Analysis of the possibilities of using ballistic systems for investigating the stratosphere

Yu. G. Tynnikov and V. A. Ivanov

''Burevestnik'' Central Research Institute, Nizhniĭ Novgorod
(Submitted December 3, 1998)
Pis'ma Zh. Tekh. Fiz. **25**, 1–6 (June 12, 1999)

An analysis is made of the possibility of conducting practical experiments in which ozone-active components of emissions (such as NO_2, Cl_2, and so on) are supplied to the stratosphere using a 203 mm self-propelled howitzer. © *1999 American Institute of Physics.* [S1063-7850(99)00106-8]

Probing of the atmosphere using active methods has been carried out since the forties, when rocket launches were first used for this purpose. In addition to launching rockets carrying measuring apparatus, some launches released dipole reflectors and various chemicals. In the sixties artillery pieces also started to be used for these purposes.[1]

In recent years, with the increasing attention being focused on ecological problems, the use of ballistic systems (artillery systems) has been preferred to launching rockets because firing a ballistic device from the ground burns up a smaller amount of fuel (solid propellant), and the combustion products are distributed in a thin layer near the earth and are not carried to the upper layers of the atmosphere. Moreover, since ballistic firing is highly accurate and the trajectories of the fired capsules have a small spread, the area required for the firing range is very much smaller than the area of a rocket launch site.

Although research into the ozone layer has been carried out for some time and the pace is intensifying, no investigations similar to the active experiments in the atmosphere have yet been undertaken for the ozone layer. The decomposition products of chlorofluorocarbons, emission of nitrous oxide, carbon monoxide, and other ozone-active gases by themselves have an anthropogenic effect on the ozone layer and the atmosphere as a whole. The ozone layer is also strongly affected by the launch of space rockets and spacecraft flights.[2]

Research has been carried out since the seventies, beginning with the work of Johnston,[3] to determine how the ozone layer is affected by subsonic and supersonic aviation and also by launches of cargo-carrying rockets. Various models have been developed to calculate the influence of emissions on the ozone layer (for example, Ref. 4) but these require data on the reaction rates under turbulent mixing conditions. For the reactions taking place when fuel combustion products are emitted in the stratosphere, it is impossible to reproduce the set of determining factors of stratospheric processes under laboratory conditions (such as gravitational acceleration, the real radiation spectrum, and so on), which makes the realistic modeling of the effects of emissions in the stratosphere a relevant issue.

Here we examine the possibility of carrying out practical experiments in which ozone-active components of emissions (such as NO_2, Cl_2, and so on) are supplied to the stratosphere using an existing ballistic device. By using this device, we can adapt the experimental setup to the capabilities of measuring systems using minimal emissions, which makes the risk of ecological consequences far lower than that involved in launching commercial rockets and aviation flights. The firing precision, characterized by a small spread ($\sim$50–100 m at 20–25 km altitude), is such that we can consider using a combination of a ballistic system to supply the active substances and a small stratosphere balloon to accommodate the measuring equipment and carry out the measurements directly in the reagent cloud.

The ballistic system being considered is a standard self-propelled 203 mm caliber ''Pion'' (Peony) howitzer. Figure 1 gives the launch altitude as a function of elevation for a standard projectile mass of 110 kg. It can be seen that this system can supply reagents at altitudes of 22–25 km which have the maximum ozone concentration (at mid latitudes).

The volume available for filling with reagents was determined taking into account the dynamic pressure in the projectile at the instant of firing. For liquid-phase reagents having densities of $(1.0–1.5)\times 10^3$ kg/m^3 and a projectile acceleration of 10 000 g, the dynamic pressure at the bottom of the projectile is $(1000–1500)\times 10^5$ Pa. Bearing in mind the strength of the casing, the permissible volume is 20–30 l with a reagent mass of $\sim$30–40 kg. The phase-transition pressure of most liquids (such as H_2O, Cl_2, N_2O_4, and so on) at ambient temperatures between -50 °C and $+50$ °C is fairly low (no higher than 15 atm), so that the capsules can be filled directly before launching and there is no need to store the filled capsules under special conditions (thermostats).

The capsules can also be filled with compressed gases, but the permissible masses of most gases compressed to several hundred atmospheres will be lower than the mass of liquid-phase substances. The most effective method is to fill the capsules with coarsely dispersed aerosols. In this case, the filling coefficient can be reduced to 0.5–0.6, so that if the standard overall mass of the capsule is 110 kg, 50–70 kg of aerosol can be supplied per shot.

These characteristics show that the experiments being discussed are technically feasible.

In order to assess the possibility of recording the emission, calculations were made of the spatial evolution of the reagent cloud and the distribution of the ozone concentration

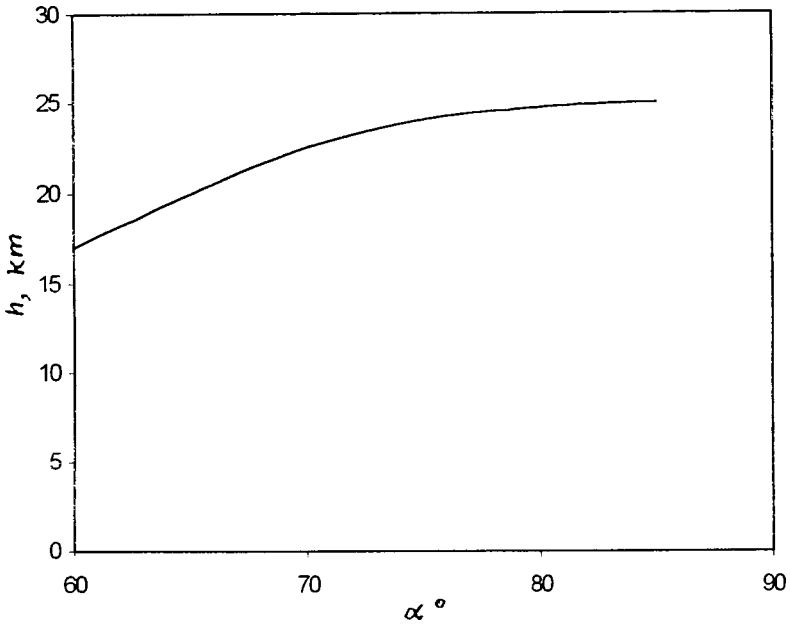

FIG. 1. Launch altitude (h) versus elevation (α) of 203 mm ballistic system.

using a model described in Ref. 5. The instantaneous emission of 30 kg NO_2 and Cl_2 into a stationary atmosphere at 25 km altitude was considered. A spherical region whose pressure is the same as that of the surrounding atmosphere is initially defined. The reagent cloud then expands anisotropically and at the same time the ozone concentration falls rapidly. As the cloud expands and the reagent concentration decreases, after more than 100 s ''slow'' reduction of the ozone begins in the interaction zone. The pattern of the process is qualitatively similar to that described by Aleksandrov and Batomonkueva.[5] In our calculations we observed a stage of ''fast'' ozone reduction in the central part of the cloud for 10–40 s when NO_2 was emitted (Fig. 2). After 40 s this stage is replaced by replenishment of the ozone concentration, which is caused by the NO_2 photodissociation reaction and does not occur when the ozone layer interacts with chlorine emissions. The maximum reduction in the total ozone content on a path running through the center of the cloud is 0.5–0.6% for both these reagents and is observed 5–7 min after emission. In this case, the horizontal diameter of the cloud increases to 400 m. Spectral devices[5] specially designed to measure short-lived ozone variations can record ~0.15% variations in the total ozone content. If necessary, repeated rounds can be fired every 5–10 min to increase the reagent mass in a particular cloud or form a chain of clouds in a particular direction. Thus, a combination of this ballistic device with terrestrial and balloon apparatus can be used to study the effect of emissions under real stratospheric conditions using minimal amounts of emissions and can also reduce the harmful effects of aircraft and rocket engines.

As well as supplying various substances into the atmosphere, ballistic systems can also be used to launch diagnostic capsules. This particularly applies to air sample collectors, but more elaborate diagnostic apparatus can also be fired from a ballistic system with a high initial acceleration.

There is no need to use large-diameter capsules to supply small devices and small quantities of materials. In this

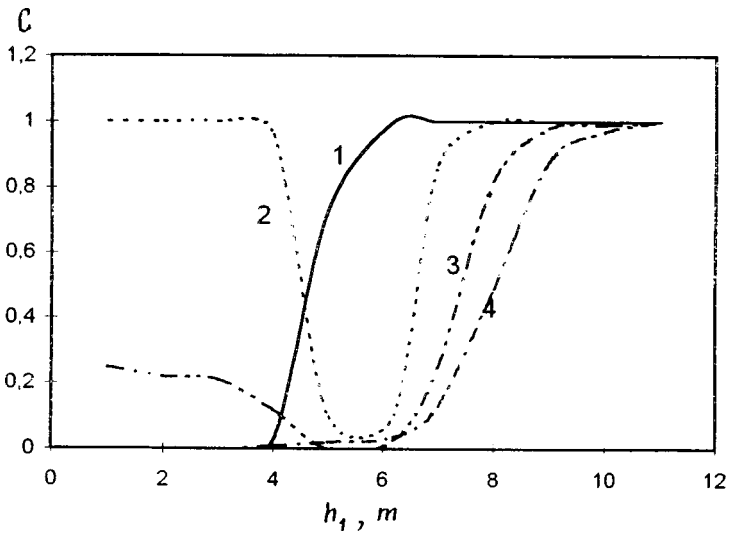

FIG. 2. Relative ozone concentration (C) versus vertical coordinate (h_1) measured from the center of emission (*1* — 5 s, *2* — 20 s, *3* — 40 s, and *4* — 60 s).

TABLE I.

Caliber, mm	Capsule weight, kg	Muzzle velocity, m/s	Launch ceiling, km
76	6.2	680	7.5
85	9.5	790	9.8
100	15.6	900	12.4
130	33	970	16.1
152	43.6	810	14.4
203	110	960	25

case, rounds of less than 203 mm caliber can be used. Table I gives data on the launch ceiling for standard-weight capsules at elevations of 80–85° for existing standard systems.

It can be seen that only a few of the standard systems can reach stratospheric altitudes. By reducing the capsule weight and also decreasing its caliber (subcaliber firing system), we can substantially raise the launch ceiling compared with the data given in the table.

[1] C. H. Murphy and G. V. Bull, J. Geophys. Res. **72**(19), 223 (1967).
[2] *Scientific Assessment of Ozone Depletion: 1991*. Report No. 25, WMO Global Ozone Research and Monitoring Project, Geneva (1992).
[3] H. S. Johnston, Science **173**, 679 (1971).
[4] R. F. Davletkin, G. M. Lokhov, and O. V. Yatsenko, Pis'ma Zh. Tekh. Fiz **19**(19), 5 (1993) [Tech. Phys. Lett. **19**, 604 (1993)].
[5] É. L. Aleksandrov and G. V. Batomonkueva, Izv. Akad. Nauk Fiz. Atmos. Okeana. **31**(1), 146 (1995).
[6] N. K. Nikiforova and N. V. Tereb, Meteor. Gidrol. No. 1, 108 (1991).

Translated by R. M. Durham

Reconstruction of dynamic systems using short signals

A. N. Pavlov, N. B. Yanson, T. Kapitaniak, and V. S. Anishchenko

Saratov State University Technical University, Łódź, Poland
(Submitted January 11, 1999)
Pis'ma Zh. Tekh. Fiz. **25**, 7–13 (June 12, 1999)

It is demonstrated that in principle, a global reconstruction technique can be used to reconstruct a dynamic description from short signals (less than ten base periods of the oscillations), which means that the reconstruction technique can be employed to estimate metric and dynamic characteristics of the operating regimes of dynamic systems using short time series.
 [S1063-7850(99)00206-2]

One method of studying various processes and phenomena in real life involves constructing and investigating mathematical models of them. Such a model is conventionally constructed by allowing for all the most important factors which influence the behavior of the system. The modeling task is complicated considerably if information on the object being studied is limited by a one-dimensional time series of one of the coordinates of state of the system. In 1987, a global reconstruction algorithm was proposed to construct a mathematical model for this case.[1,2] This algorithm can provide a dynamic description in the form of a system of first-order ordinary differential equations or discrete mappings and is implemented in two stages. The first stage involves determining the embedding space dimension and reconstructing the attractor using the scalar time series $a_i = a(i\Delta t)$, $i=1,\ldots,N$. The second stage involves defining *a priori* the general form of the equations and specifying the evolution operator by the least squares method. This method was later improved[3–5] and new approaches were developed for modeling using a one-dimensional time series.[6,7]

We assume that the system being studied can be described in the form

$$\frac{d\mathbf{x}}{dt}=\mathbf{F}(\mathbf{x}), \quad \mathbf{x}\in R^n, \tag{1}$$

where $\mathbf{F}$ is a nonlinear vector function and $\mathbf{x}$ is the state vector. Several methods are available for reconstructing the vector $\mathbf{x}$ from a time series, of which the following two are the most popular:

$$\mathbf{x}(t)=(a(t),a(t+\tau),\ldots,a(t+(n-1)\tau)), \tag{2}$$

$$\mathbf{x}(t)=(a(t),da(t)/dt,\ldots,d^{n-1}a(t)/dt^{n-1}). \tag{3}$$

The global reconstruction problem is solved by selecting *a priori* the form of the vector function $\mathbf{F}$ in Eq. (1), calculating the values of $d\mathbf{x}_i/dt$ by numerical differentiation of the scalar time series a_i, and then using the least squares method to specify the evolution operator.

One of the main problems here is selecting the right-hand sides of Eq. (1). Since it is impossible to specify *a priori* even an approximate form of the functions F_j, $j=1,\ldots n$, these are represented as an expansion in terms of a certain basis, limited to a finite number of terms. In the simplest case, F_j can be defined in terms of ν-degree polynomials:

$$F_j(\mathbf{x}_i)=\sum_{l_1,l_2,\ldots,l_n=0}^{\nu} C_{j,l_1,l_2,\ldots,l_n}\prod_{k=1}^{n} x_{k,i}^{l_k}, \quad \sum_{k=1}^{n} l_k\leqslant\nu, \tag{4}$$

where $C_{j,l_1,l_2,\ldots,l_n}$ are unknown coefficients which need to be determined. This representation will be used in the present study.

We note that the reconstructed model will be cumbersome and will contain many (usually several tens) of the coefficients $C_{j,l_1,l_2,\ldots,l_n}$. The global reconstruction procedure itself, which includes carefully selecting the parameters of the algorithm at all its stages, is very tedious and laborious. When this procedure is implemented, the question arises as to what this model actually gives the researcher in the event of a successful reconstruction. The information of practical interest in the analyses of time series is that on the operating characteristics of the dynamic system generating this time series. Given the implication that in the dynamic system under study there is an attractor, these characteristics are the spectrum of Lyapunov exponents and the dimension. These characteristics are usually calculated using standard algorithms (for instance, Refs. 8 and 9), provided that the time of the series is sufficiently long that the structure of the attractor being studied can be assessed along the phase trajectory. When fundamentally short signals are used (less than ten base periods of the oscillations) it is incorrect to use these methods, because over the observation time the phase trajectory does not have time to visit all the regions of the attractor and/or returns to these regions insufficiently frequently.[10] Here we consider the possibility of using a global reconstruction algorithm to estimate the attractor characteristics in these situations. From this point of view the influence of the signal duration (the number of points N for a fixed discretization step Δt) on the result of the modeling acquires fundamental importance.

In Ref. 11, by applying a reconstruction algorithm to one-dimensional time series obtained by integrating the equations for a Van der Pol oscillator

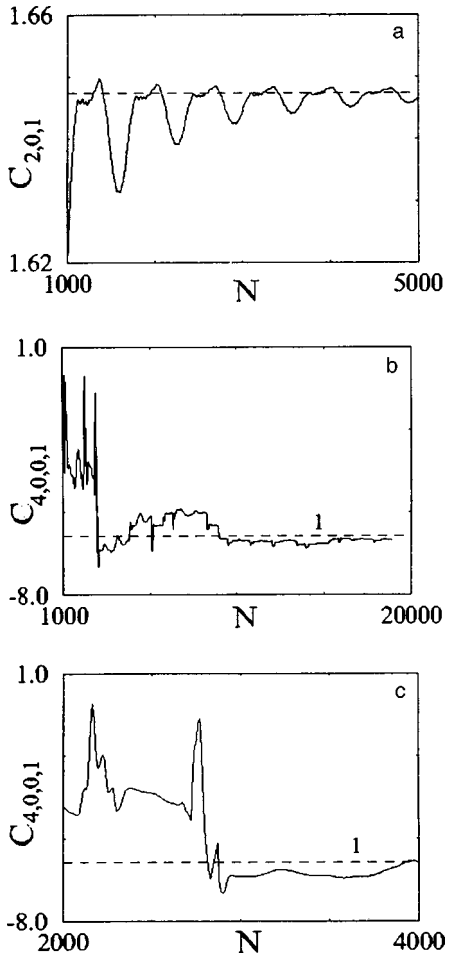

FIG. 1. Arbitrarily selected coefficients in the approximations to the nonlinearities on the right-hand sides of the equations in the reconstructed model as a function of the number of points in the times series: a — Van der Pol oscillator ($n=2$, reconstruction using first coordinate, $\Delta t=0.01$, delay method, $\nu=3$); b, c — for a Rössler system ($n=4$, reconstruction using first coordinate, $\Delta t=0.01$, two coordinates reconstructed by the delay method, one by numerical differentiation, $\nu=3$). Line *1* corresponds to $C^0_{4,0,0,0,1}\approx -5.9$.

$$\frac{dx}{dt}=y, \quad \frac{dy}{dt}=a(1-bx^2)y-x, \quad a=1.0, \quad b=0.3 \quad (5)$$

and a Rössler system

$$\frac{dx}{dt}=-(y+z), \quad \frac{dy}{dt}=x+ay, \quad \frac{dz}{dt}=b+z(x-c),$$

$$a=0.15, \quad b=0.2, \quad c=10.0, \quad (6)$$

and also to various other known model systems, we established that the N dependence of each approximation coefficient $C_{j,l_1,l_2,\ldots,l_n}$ separately exhibits convergence to some limiting value $C^0_{j,l_1,l_2,\ldots,l_n}$ as N increases. Two examples are illustrated in Figs 1a and 1b.

We introduce the relative error in the determination of the coefficient caused by the short length of the time series $\delta_N^{j,l_1,l_2,\ldots,l_n}=|C_{j,l_1,l_2,\ldots,l_n}-C^0_{j,l_1,l_2,\ldots,l_n}|/|C^0_{j,l_1,l_2,\ldots,l_n}|$. Having defined the permissible error $\delta_{\max}^{j,l_1,l_2,\ldots,l_n}$, we can determine $N_{\min}$ using the envelope $C_{j,l_1,l_2,\ldots,l_n}(N)$ such that for any $N>N_{\min}$ the value of $\delta_N^{j,l_1,l_2,\ldots,l_n}$ will be less than $\delta_{\max}^{j,l_1,l_2,\ldots,l_n}$. The estimate of $N_{\min}$ indicates the minimum length of the time series required to calculate the approximation coefficients with predefined accuracy.

Note that the behavior of the reconstructed coefficients (convergence) does not depend on how well the *a priori* selected form of the model can describe the operating regime of the initial system. In the following analysis we shall only consider those forms of the right-hand sides for which the solution of the reconstructed system can describe the initial oscillation regime fairly accurately. We also note that solving the problem of reconstructing a system with a periodic regime seems to us fairly trivial. In addition, studying a section of a time series which exhibits only a few oscillations does not allow one to say whether it corresponds to a chaotic or a complex periodic regime. Thus, we shall confine our analysis to the case when the oscillation regime under study is chaotic.

We shall consider the specific example of a Rössler system. For the given values of a, b, and c this system demonstrates chaotic behavior with an attractor characterized by the following spectrum of Lyapunov exponents: $\lambda_1\approx 0.09$, $\lambda_2=0.0$, $\lambda_3\approx -10.0$. We shall take the coordinate $x(t)$ discretized with the step $\Delta t=0.01$ as the signal being studied. We shall solve the modeling problem for this signal for various N ($N\in[2000-4000]$). The other parameters were selected as follows: $n=4$, $\nu=3$. Of the three reconstructed phase coordinates two were obtained by a delay method and one was obtained by numerical differentiation of $x(t)$. Figure 1c shows the dependence of the arbitrarily selected reconstructed coefficient $C_{j,l_1,l_2,\ldots,l_n}$ in this range of N.

In order to obtain a clear representation of the results of the modeling for each reconstructed dynamic system for a selected number of points N, we shall calculate the spectrum of the Lyapunov exponents and the Lyapunov dimension using the Kaplan–Yorke formula.[12] The corresponding dependence of λ_1 and D_L is plotted in Figs. 2a and 2b.

It can be seen from this figure that there is a set of N values for which the attractor of the reconstructed mathematical model (when the other parameters of the numerical system are fixed) has dynamic characteristics similar to those of the attractor of the initial system generating the signal being studied. However, there is also a set of N values for which periodic oscillations ($\lambda_1=0$) are reconstructed instead of dynamic chaos. In Fig. 2a the asterisks also indicate points where the phase trajectory does not belong to the basin of attraction of the attractor of the reconstructed equation (the solutions of the model system do not possess the property of Poisson stability).

In this case, the distribution of the λ_1 and D_L values obtained for various N will have two maxima (Figs. 2c and 2d), one corresponding to the known unsuccessful reconstruction, i.e., the reconstruction of the periodic oscillation regime using a chaotic signal. The second maximum corresponds to $\lambda_1\approx 0.08$, $D_L\approx 2.016$. In Fig. 2c the dashed lines

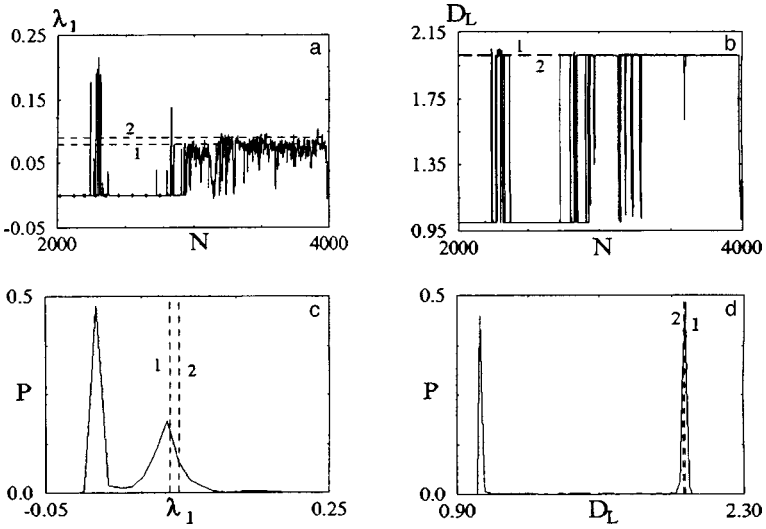

FIG. 2. a, b — Values of the leading Lyapunov exponent calculated by the method described in Ref. 13 and of the Lyapunov dimension of the attractors in the mathematical models reconstructed for each N. The lines *1* give the attractor characteristics of the model system reconstructed using a long signal, i.e., several hundred base periods ($\lambda_1=0.08$, $D_L=2.015$), the lines *2* give the attractor characteristics of the initial system (6) — $\lambda_1=0.09$, $D_L=2.01$; c, d — distribution densities of λ_1 and D_L.

show the values of the leading Lyapunov exponent calculated by a method described in Ref. 13 using the equations of a mathematical model reconstructed by a method of reconstruction using a long signal, i.e., several tens of base periods (line *1*) and using the equations of system (6) (line *2*). The results show that the positive value of the Lyapunov exponent corresponding to the distribution maximum is close to the true value.

To conclude, provided that the *a priori* selected form of the dynamic equations can qualitatively describe the initial chaotic regime, applying the reconstruction algorithm to short time series can give estimates of the characteristics of the initial attractor similar to those which can be calculated by processing long time series using standard methods.

Similar results were obtained for a modified inertial-nonlinearity generator[14] and for various other systems.

This work was partially supported by INTAS Grant No. 96-0305 and by the Royal Society, London.

[1] J. Cremers and A. Hübler, Z. Naturforsch. Teil A **42**, 797 (1987).
[2] J. P. Crutchfield and B. S. McNamara, Complex Syst. **1**, 417 (1987).
[3] G. Gouesbet and J. Maquet, Physica D **58**, 202 (1992).
[4] G. Gouesbet and C. Letellier, Phys. Rev. E **49**, 4955 (1994).
[5] J. L. Breeden and A. Hübler, Phys. Rev. A **42**, 5817 (1990).
[6] H. Voss and J. Kurths, Phys. Lett. A **234**, 336 (1997).
[7] R. Hegger, M. J. Bünner, H. Kantz, and A. Giaquinta, Phys. Rev. Lett. **81**, 558 (1998).
[8] P. Grassberger and I. Procaccia, Phys. Rev. Lett. **50**, 346 (1983).
[9] A. Wolf, J. B. Swift, H. L. Swinney, and J. A. Vastano, Physica D **16**, 285 (1985).
[10] G. G. Malinetskiĭ, A. B. Potapov, and A. I. Rakhmanov, Preprint No. 10 [in Russian], M. V. Keldysh Institute of Applied Dynamics, Russian Academy of Sciences, Moscow (1993).
[11] A. N. Pavlov, N. B. Yanson, and V. S. Anishchenko, Pis'ma Zh. Tekh. Fiz **23**(8), 7 (1997) [Tech. Phys. Lett. **23**, 297 (1997)].
[12] J. L. Kaplan and J. A. Yorke, Lect. Notes Math. **898**, 204 (1981).
[13] G. Benettin, L. Galgani, and J. M. Strelcun, Phys. Rev. A **41**, 2338 (1976).
[14] V. S. Anishchenko, *Complex Oscillations in Simple Systems* [in Russian], Nauka, Moscow (1990), 311 pp.

Translated by R. M. Durham

Investigation of the propagation of an ultrasound pulse in a dispersed fractal medium

P. A. Golovinskiĭ, D. Yu. Zolototrubov, Yu. S. Zolototrubov, and V. T. Pertsev

Voronezh State Academy of Architecture and Civil Engineering
(Submitted November 5, 1998)
Pis'ma Zh. Tekh. Fiz. **25**, 14–18 (June 12, 1999)

Results are presented of an experimental determination of the fractal parameters of crushed sand particles. Results of measurements of the propagation of an acoustic pulse through a mass of sand having various degrees of dispersion are used to determine the fractional exponent in the dependence of the propagation velocity on the ultrasound wavelength. A wave equation in fractional derivatives is proposed to describe the propagation of ultrasonic waves in a dispersed medium. © *1999 American Institute of Physics.* [S1063-7850(99)00306-7]

The structure and properties of dispersed media have recently attracted increasing attention among researchers. These media are extremely widespread, occurring both naturally, as in media of geological origin, and in various technological applications. Particular interest is being directed toward these media because of the self-organized criticality of the phenomena observed therein.[1] Phenomena of this type are characterized by self-similarity of the processes taking place on different scales. A renormalization group approximation has been developed to describe these phenomena in statistical physics and quantum field theory, and this can be applied to calculate important physical parameters.[2] From the point of view of geometric structure, self-similar structures, including statistically self-similar ones, are fractals[3] and analyses of these structures are based on fractional derivatives.[4,5] The fractal properties of various dispersed media have been established for many friable materials by measuring the adsorption of gases by their developed surfaces.[6]

In the present study a method of optical analysis was used to investigate the fractal nature of particles of crushed quartz sand having various degrees of dispersion, and then the results of ultrasound investigations were then used to determine the fractal nature of a mass of quartz sand.

Particles of quartz sand were photographed through a microscope at $280^{\times}$ magnification for sand having a specific surface area s between 3 and 35 m^2kg and at $630^{\times}$ magnification for $s > 100\ m^2$kg. The fractal dimension of the perimeter of the projection of the sand particles on a plane was determined for different scales.[7] The dependence of the number N_L of length elements covering the perimeter on the scale is a power law:

$$N_L = \delta^{-D_L}, \tag{1}$$

where D_L is the fractal dimension and δ is the scale.

Figure 1a gives N_L as a function of δ using a log–log plot. It can be seen that the experimental points are a good fit to a straight line. Moreover, the lines have the same slope for different particles having a specific surface area. For different specific surface areas D_L varies between 1.23 for $s = 200\ m^2/kg$ and 1.16 for $s = 35\ m^2/kg$.

The fractal dimension D_S of the particle projection area was calculated by counting the number of squares N_S cover-

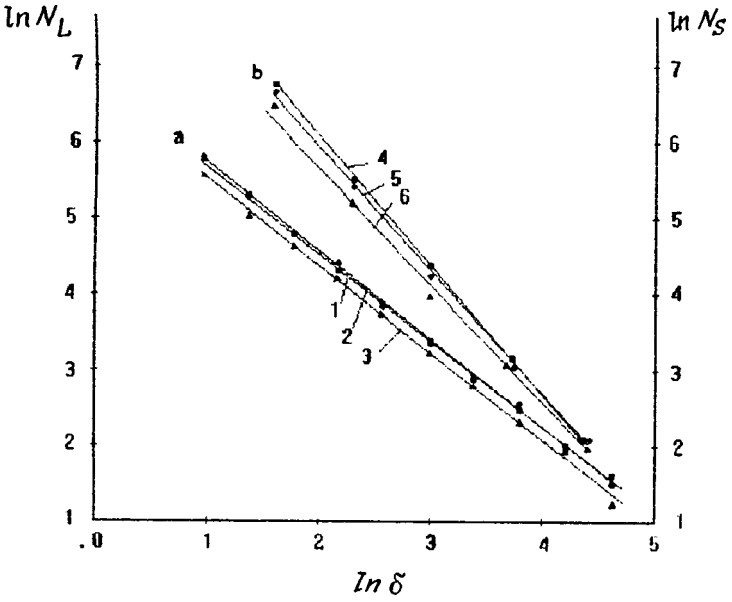

FIG. 1. Logarithm of the number of particles N_L of the perimeter length elements (a) and logarithm of the number of squares N_S covering the area of the particle projection (b) as a function of the logarithm of the scale δ for quartz sand particles having specific surface areas: *1, 4* — 35, *2, 5* — 100, and *3, 6* — 200 m^2/kg.

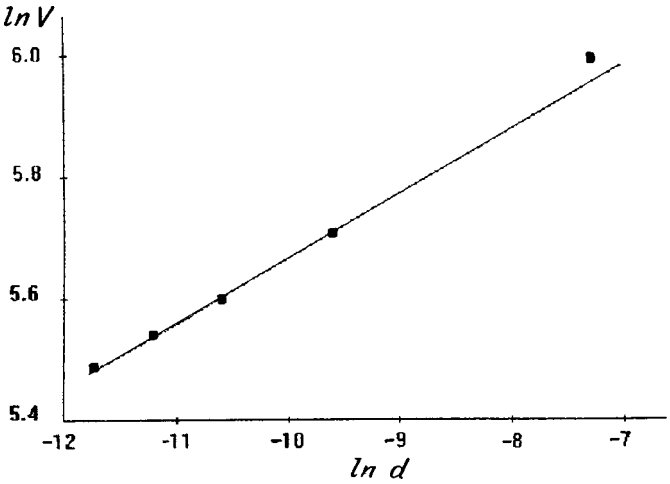

FIG. 2. Logarithm of the ultrasound propagation velocity in quartz sand as a function of the logarithm of the mean particle diameter.

ing the area of the particle projection on the plane for different scales δ of the sides of the squares. Figure 1b gives N_S as a function of δ in a log–log plot. The linear nature of the experimental dependence also shows up clearly here, and D_S varies between 1.582 for $s=200\,\mathrm{m}^2/\mathrm{kg}$ and 1.784 for $s=35\dot{\mathrm{m}}^2/\mathrm{kg}$. An important problem now is to determine the structure of the entire mass of sand. In order to identify this relationship, we measured the velocity of sound in dry quartz sand having different degrees of dispersion. The wavelength of the ultrasound propagating through the medium was at least an order of magnitude greater than the particle size, which ensured that the medium was studied in the wave propagation regime. The measurements were made at a pulse repetition rate of 67 kHz and the thickness of the samples was 25 mm. We measured the time taken for the leading edge of an ultrasound pulse to cover a known distance in the medium and we then calculated the wave propagation velocity. The pulse shape varied negligibly during propagation through the samples.

The results of the measurements are plotted in Fig. 2 in the form of a graph showing the linear dependence of the logarithm of the ultrasound propagation velocity in a mass of quartz sand on the logarithm of the mean particle diameter. As the dispersion of the sand increases, the ultrasound propagation velocity decreases, falling below the speed of sound in air. In order to explain the observed dependence of the velocity of sound in the medium on its fractal properties, we propose a model of a wave equation with fractional spatial derivatives.

In order to construct a mathematical model of the one-dimensional propagation of a longitudinal wave along the x axis in a dispersed medium, we assume that the stress at the boundary of a selected volume V is determined by the gradient of the displacement u of the solid phase. Newton's second law for the selected volume can then be written as

$$\int \rho \frac{\partial^2 u}{\partial t^2} dV = k \int \frac{\partial^{2D} u}{\partial x^{2D}} dS. \tag{2}$$

We utilized the fact that the total increment of the quantities in a self-similar discontinuous structure is expressed in terms of fractional integrodifferentiation.[5] Using a Gauss transformation for the transition from an integral over surface to an integral over volume on the right-hand side of Eq. (2) and converting to differential notation, we obtain

$$\frac{\partial^2 u}{\partial t^2} = c^2 \frac{\partial^{2D} u}{\partial x^{2D}}, \tag{3}$$

where $c^2 = k/\rho$, $1<D<2$. Note that fractional differentiation was used earlier to construct a model of filtration in porous media with a fractal structure.[8]

Mainardi and Tomirotti[9] used a Laplace transformation to obtain a fundamental solution of an equation of the type (3) in the form

$$u = M(z;\beta), \quad z = |x|/ct^{\beta}, \quad \beta = 2-D,$$

$$M(z;\beta) = \sum_{n=0}^{\infty} \frac{(-1)^n z^n}{\Gamma[-\beta n + (1-\beta)]}. \tag{4}$$

Equation (3) generates a dispersion equation $k^D = \alpha\omega$ for the propagation of sound in a fractal. The velocity of this wavefront is $v \sim k^{D-1}$. Assuming that the fractal object possesses scale self-similarity, a change in the particle scale by a factor a implies an effective change in the wavelength $\lambda \to \lambda/a$. The change in velocity is then given by $v \sim a^{D-1}$.

Using the data obtained by measuring the velocity for various degrees of dispersion of the medium plotted in Fig. 2, we obtained the exponent $D=1.103$, which confirms the fractal nature of the system. This fractional dispersion dependence is well-known for fractal meshes.[10] In our view, the reduction in the ultrasound propagation velocity with increasing dispersion of the sand can be attributed to an increase in the effective acoustic propagation path for the sound wave through the material. This result reflects the fact that the structure of a mass of quartz sand consists of alternate voids and dense particle formations with numerous contacts.

To conclude, we must stress that the assumption frequently made when modeling dispersed systems, namely, that the particles are arbitrarily spherical and closely packed, is inconsistent with the real structure of finely dispersed media.

[1] P. Bak, Tang Chao, and K. Wiensenfeld, Phys. Rev. Lett. **59**, 381 (1987).
[2] N. N. Bogoliubov and D. V. Shirkov, *Introduction to the Theory of Quantized Fields*, 3rd ed. (Wiley, New York, 1980; Russ. original, 4th ed., Nauka, Moscow, 1984, 649 pp.).
[3] B. Mandelbrot, *Les Objects Fractal* (Flammarion, 1995), 200 pp.
[4] R. R. Nigmatullin, Teor. Mat. Fiz. **90**, 354 (1992).
[5] I. P. Guk, Zh. Tekh. Fiz **68**(4), 7 (1998) [Tech. Phys. **43**, 353 (1998).
[6] J. Feder, *Fractals* (Plenum Press, New York, 1988; Mir, Moscow, 1991, 260 pp.).
[7] S. Tricot, *Courbe et Dimension Fractale* (Springer-Verlag, Paris, 1993), 349 pp.
[8] R. P. Meĭlanov, Pis'ma Zh. Tekh. Fiz **22**(23), 40 (1996) [Tech. Phys. Lett. **22**, 967 (1996)].
[9] F. Mainardi and M. Tomirotti, in *Proceedings of the International Workshop on Transforms and Special Functions*, Sofia, 1994, pp. 171–183.
[10] T. Nakayama and K. Yakubo, Rev. Mod. Phys. **66**, 381 (1994).

Translated by R. M. Durham

High-efficiency narrow-band free-electron maser using a Bragg cavity with a phase discontinuity in the ripples

N. Yu. Peskov, N. S. Ginzburg, A. A. Kaminskiĭ, A. K. Kaminskiĭ, S. N. Sedykh, A. P. Sergeev, and A. S. Sergeev

Institute of Applied Physics, Russian Academy of Sciences, Nizhniĭ Novgorod, Joint Institute for Nuclear Research, Dubna
(Submitted January 22, 1999)
Pis'ma Zh. Tekh. Fiz. **25**, 19–28 (June 12, 1999)

A new, highly selective Bragg cavity system having phase discontinuity in the ripples inside the interaction space was used to develop a free-electron maser based on the LIU-3000 accelerator (free-electron maser oscillator). This system operated at 30.7 GHz with a power of around 50 MW and an efficiency of 35%, which is the highest yet recorded for this class of system. © *1999 American Institute of Physics.* [S1063-7850(99)00406-1]

1. Bragg cavities in the form of waveguide sections with slightly rippled side walls were first proposed as electrodynamic systems for free-electron masers in Refs. 1–3 and have been successfully used to fabricate narrow-band oscillators in the millimeter wavelength range.[3–7] These experiments used a two-mirror system: the cavity was formed by two Bragg reflectors separated by a section of regular waveguide in which the interaction with the electron beam mainly took place. In particular, this type of cavity was used in a free-electron maser (FEM) oscillator developed in joint experiments at the Joint Institute of Nuclear Research (Dubna) and the Institute of Applied Physics of the Russian Academy of Sciences (Nizhniĭ Novgorod) based on the LIU-3000 linear induction accelerator. In these experiments using a reversed guide field, Bogachenkov *et al.*[8] and Ginzburg *et al.*[9] reported a 35 MW output power with 26% efficiency at 31 GHz, which exceeded the level achieved earlier in similar oscillators.[3–7] Single-mode, single-frequency oscillation was achieved in the range of optimum parameters. A numerical simulation indicates that this regime is established at the nonlinear stage as a result of competition between several longitudinal modes falling within the effective reflection band of the Bragg reflectors and initially excited by the electron beam. The results of the simulation and the experiments show that when the phase mismatch varies (i.e., when the energy or the translational velocity of the particles varies), various longitudinal cavity modes having similar frequencies and Q-factors may be excited. This circumstance may be considered to be a particular disadvantage of this type of oscillator because, as a result of the almost unavoidable instability during operation of the accelerator and the power sources of the FEM electron-optical system, jumps in the radiation frequency may occur during a single pulse and from one pulse to another. However, for many applications of high-power millimeter oscillators, stringent constraints must be imposed on the frequency stability of the radiation. For instance, high stability combined with high powers are required to power the high-gradient structures in the new generation of accelerators.[10]

This problem may be resolved by using an alternative Bragg cavity system, also considered by Kovalev *et al.*[1], which consists of a cavity formed by two rippled waveguides, where the ripple has a phase discontinuity of π where the two meet (Fig. 1). This cavity has a natural mode at the exact Bragg resonance frequency whose Q-factor considerably exceeds that of the other modes. This circumstance significantly enhances the selective properties of this cavity compared with a conventional two-mirror system. The high Q-factor of the dominant cavity mode means that the length of the interaction space can be reduced, which is attractive for improving the efficiency and lowering the sensitivity to the initial spread of beam parameters. Here we report theoretical and experimental studies of an FEM oscillator based on this new type of Bragg cavity.

2. The conditions for the establishment of single-mode, single-frequency oscillation were first investigated by means of a numerical simulation of the process of establishment of self-oscillation. A method of coupled (concurrent and counterpropagating) waves was used to describe the interaction of intra-Bragg structures via a space–time approach.[11] Figure 2a gives the time dependence of the electron efficiency for a moderate excess of the cavity Q-factor above the threshold. An analysis of the frequency spectrum shows that the dominant cavity mode is excited at the exact Bragg resonance frequency with almost no ''parasitic'' modes even under transient conditions.

Note that, along with the highest-Q mode, the spectrum of cavity modes generally also contains additional modes (''lateral'' relative to the Bragg frequency) whose frequencies lie outside the opacity band of the Bragg structures. These modes are essentially the modes of the various segments making up the phase-shift cavity. As the coefficient of wave coupling at the Bragg structures increases (i.e., the depth of the ripple increases), the Q-factors of these modes increase and ultimately the starting conditions for the excitation of these modes are also satisfied. Several cavity modes can be excited under transient conditions in this cavity. However, in the nonlinear regime, when the Q-factor of the modes moderately exceeds the lasing threshold, the highest-Q mode then inhibits the others as a result of nonlin-

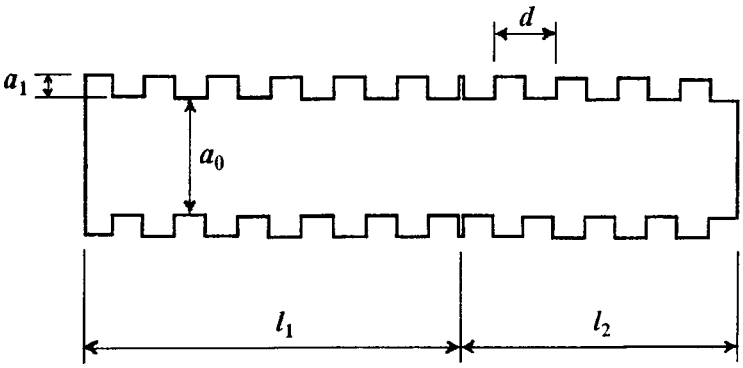

FIG. 1. Schematic of Bragg cavity with a ripple phase discontinuity.

ear competition, and steady-state oscillation is established in this mode (Fig. 2b). It is important to note that for optimized parameters steady-state oscillation in the dominant mode is established for any phase mismatches in the self-excitation band. Moreover, the longitudinal field structure in the cavity is more favorable for removing energy from the electron beam (Fig. 2b) compared with a two-mirror cavity, which enhances the efficiency by a factor of approximately 1.5.

An increase in the length of the segments making up the cavity causes a further increase in the Q-factors of the lateral modes. By systematically varying the phase mismatch in this cavity, it is possible to establish steady-state oscillation in the dominant highest-Q mode and in lateral modes (Fig. 2c). Nevertheless, the frequencies of the lateral and dominant modes are fairly well separated, their frequency difference being half the width of the opacity band of the Bragg structures. This is slightly greater than that for a two-mirror cavity where several longitudinal cavity modes lie within the opacity band. Thus, in a phase-shift cavity an appreciable change in the phase mismatch is required to tune the oscillation from the dominant to a lateral mode. The constraints on the operating stability of the FEM power supply system can be reduced considerably and are easily attainable in existing experimental facilities.

3. The FEM electrodynamic system used for the experiment comprised a cavity formed by two sections of circular waveguide 22 mm in diameter, with rippled side walls in the form of a meander of period $d=5.4$ mm and depth a_1 between 0.3 and 0.6 mm. At the point where these structures were joined, the ripple has a phase discontinuity of π. The length of the cavity input segment l_1 (on the cathode side) was varied between 20 and 40 cm and the length of the output segment l_2 was varied between 10 and 20 cm. The lowest $TE_{1,1}$ mode of the circular waveguide was selected as the working mode. The optimum cavity parameters were calculated for the conversion of this working mode of the intra-Bragg structure into a feedback mode $TM_{1,1}$, which was observed near 31GHz. Figure 3a and 3b give the calculated dependence for cavities of different length and also the results of cold electrodynamic measurements of the reflection coefficient as a function of frequency for a Bragg cavity with a ripple phase discontinuity. In this method of measurement,

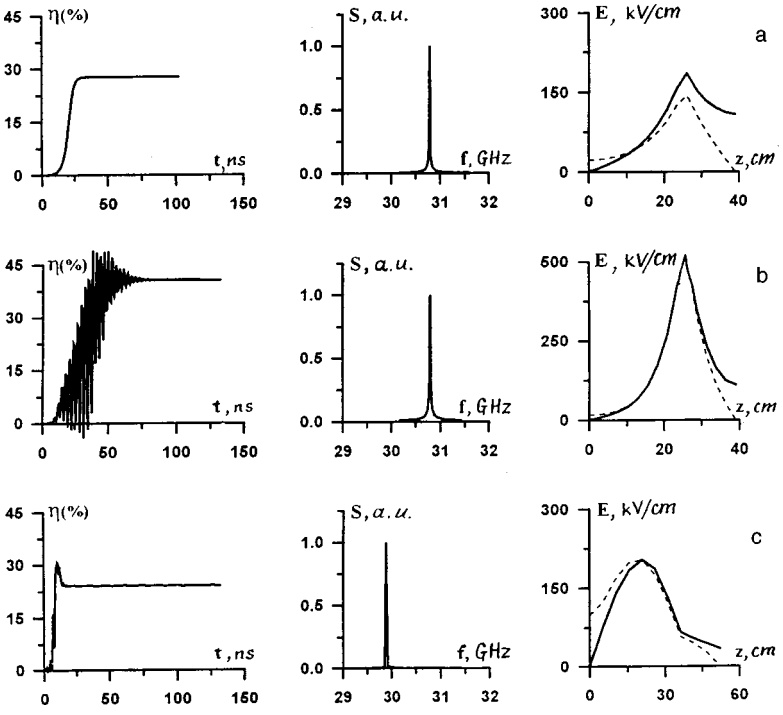

FIG. 2. Simulation of the process of establishment of self-oscillation in cavities with a ripple phase discontinuity of different geometry. Time dependence of the efficiency (η) and also radiation spectrum (S) and longitudinal field structure (E) of the partial waves (solid curve — concurrent wave, dashed curve — counterpropagating wave) under steady-state oscillation: a — $l_1=26$ cm, $l_2=13$ cm, $a_1=0.4$ mm, $B_w=0.1$ T; b — $l_1=26$ cm, $l_2=13$ cm, $a_1=0.6$ mm, $B_w=0.09$ T; c — $l_1=39$ cm, $l_2=13$ cm, $a_1=0.6$ mm, $B_w=0.12$ T ($E_{\text{beam}}=0.8$ MeV, $I_{\text{beam}}=170$ A, $B_0=-0.2$ T).

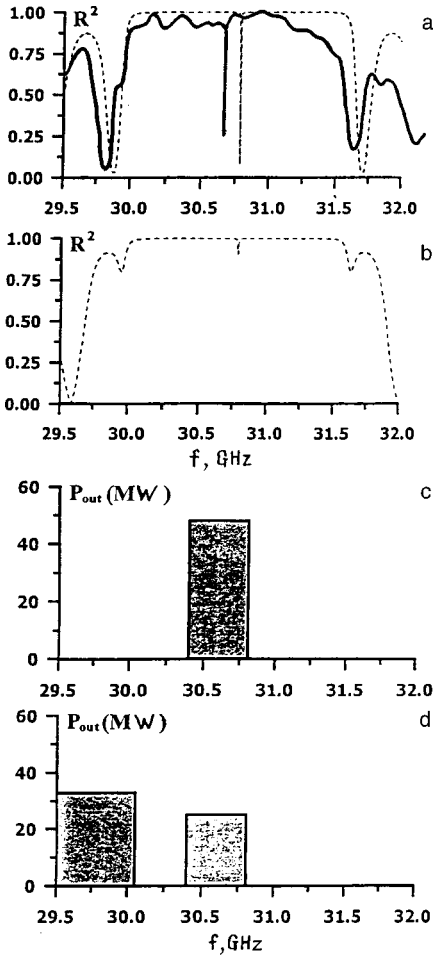

FIG. 3. Reflection coefficient R as a function of frequency for cavities of different geometry (solid curve — result of cold electrodynamic measurements, dashed curve — calculated values: a — $l_1=l_2=21.6$ cm and b — $l_1=26$ cm, $l_2=13$ cm ($a_1=0.6$ mm). The hatched areas in Figs. 1c and 1d indicate the frequency intervals in which the recorded radiation frequency fell for free-electron masers with different cavity geometries, and the height of the hatched region corresponds to the maximum radiation power: c — $l_1=26$ cm, $l_2=13$ cm; d — $l_1=39$ cm, $l_2=13$ cm ($a_1=0.6$ mm).

the natural modes correspond to the minima of the reflection coefficients. Note that when the lengths of the segments are equal, the incident wave is reflected from them in antiphase, so that in this case the reflection coefficient at the frequencies of the natural modes tends to zero (Fig. 3a). When the lengths of the segments differ substantially, the coefficients of reflection from each segment differ significantly and the total reflection coefficient from this cavity will be fairly close to unity, even at the frequencies of the natural modes (Fig. 3b). This explains the difficulty of making cold measurements in cavities having this geometry.

It can be seen from Fig 3a that for a symmetric cavity the width of the opacity band and consequently the coefficient of wave coupling at the Bragg structure $\sim 0.16\,\mathrm{cm}^{-1}$ show good agreement with the calculated results. The measured frequency of the highest-Q mode was 30.7 GHz, and the small shift from the calculated value may be attributed to the difference between the period of the fabricated structure and the calculated value. For the asymmetric cavity whose parameters are given in Fig. 3b (in which the maximum output power was obtained in a hot experiment), the calculated Q-factor of the dominant mode at the exact Bragg resonance frequency for a known wave coupling coefficient was 1300.

4. Experimental investigations of the free-electron maser were carried out using the LIU-3000 linear induction accelerator (Joint Institute for Nuclear Research, Dubna), which delivered an electron beam having a particle energy of 0.8 MeV, a current of up to 200 A, and a pulse duration of 200 ns at a pulse repetition rate up to 1 Hz. A working transverse velocity $\beta_\perp \approx 0.2$ was imparted to the particles in a spiral wiggler with a period of 6 cm, having adiabatically smooth switching for the first six periods. The wiggler was positioned inside a solenoid. The amplitude of the transverse field B_w on the axis was varied between 0 and 0.3 T and the guiding magnetic field B_0 was regulated up to 0.7 T. The output current from the accelerator and the oscillator was recorded using induction and resistive detectors and was 150–200 A under various operating conditions. The radiation power was measured using calibrated crystal detectors for which the accuracy, including the calibration accuracy, was $\sim 20\%$. The radiation spectrum was measured using a set of cutoff waveguide filters with a diameter step of 0.1 mm, which can determine the frequency in the range 26–40 GHz to within 1.5–2%.

The selected operating regime of the free-electron maser used a reversed magnetic guide field (subsequently denoted as negative),[12,13] oriented so that the direction of the cyclotron rotation of the electrons was the opposite of their direction of rotation in the field of the spiral wiggler. Advantages of this FEM operating regime are that a high-quality helical electron beam is formed, the sensitivity to the initial spread of the beam parameters is low, and consequently a high efficiency can be achieved.[9,14] This is confirmed by the results of previous experimental investigations of amplifier[12,13] and oscillator[8,9] FEM systems where the maximum efficiency was obtained in this regime.

In the present experiment, circularly polarized radiation was observed on entry to the free-electron maser, whose structure corresponded to the excitation of the $TE_{1,1}$ lasing mode. The microwave pulse lasted 100–150 ns. In agreement with the calculations, the maximum radiation power was obtained near 31 GHz. The system was tuned to the optimum oscillation regime by varying the wiggler and solenoid fields, which altered the particle translational velocity. The cavity parameters were varied by selecting the ripple depth, the lengths of the Bragg structures (segments), and also the length ratio of these segments.

The maximum radiation power of 48 ± 5 MW was obtained at 30.7 GHz using a cavity formed by segments 26 and 13 cm long. The working current was 170 A, which corresponded to a lasing efficiency of around 35%. The wiggler and solenoid fields were $B_0 = -0.21$ T and $B_w = 0.12$ T. The results of measurements of the radiation spectrum for these cavity parameters are plotted in Fig. 3c. The hatched region corresponds to the frequency range between two neighboring filters (in terms of cutoff frequencies) in which the radiation frequency fell. A comparison with the results of the cold measurements of the mode spectrum (Figs. 3a and 3b) suggests that the measured spectrum can be interpreted as

single-mode single-frequency oscillation. Further confirmation that the oscillation is single-mode is provided by the absence of any low-frequency modulation of the output signal corresponding to the mode beats, which was observed earlier in multifrequency oscillation regimes in free-electron masers with two-mirror Bragg cavities.[9] However, the fairly large difference between the frequencies of the dominant and lateral cavity modes (around 2%) allowed the oscillation at these frequencies to be distinguished experimentally using the existing set of waveguide filters. In previous experiments using two-mirror Bragg cavities, it was difficult to measure the radiation spectrum by a similar method.[8] It should be noted that in accordance with the results of the simulation (Figs. 2a and 2b) for optimum cavity parameters over the entire range of variation of the fields B_0 and B_w (i.e., over the entire range of phase mismatch) oscillation was observed in the dominant mode in the cavity self-excitation band.

When the position of the phase discontinuity was shifted toward the center of the cavity (i.e., using segments of equal length), the output power decreased. This is because when the Bragg structures are positioned symmetrically, the microwave energy fluxes in both directions of the cavity are the same.[1] Degrading the symmetry of the cavity by shifting the phase discontinuity toward the collector can provide almost unidirectional coupling out of the radiation (compare Figs. 2a and 2b).

It should be noted that when the length of the input segment of the cavity was increased to 39 cm, the results of the simulation indicated that lateral modes were excited separately. Results of measurements of the power and frequency of the output radiation in the range 29–32 GHz are plotted in Fig. 3d. The oscillation frequency was tuned by varying the fields B_0 and B_w, i.e., by selecting the optimum mismatch for the excitation of each mode (compare with Fig. 2c). The fields for which radiation was observed in the lateral mode at frequency 29.9 GHz were $B_0 = -0.18$ T and $B_w = 0.11$ T.

5. To sum up, in these experiments we have demonstrated for the first time the efficiency of a Bragg cavity with a phase discontinuity and have shown that these cavities are potentially useful for FEM oscillators. Various cavity configurations have been studied. The FEM parameters for which oscillation was observed and the measured efficiencies show good agreement with the values obtained from a numerical simulation of the excitation process. For optimum cavity parameters an output power of around 50 MW was obtained at 30.7 GHz with a 35% efficiency, which is the highest yet recorded for this type of device. The radiation spectrum corresponded to the excitation of the highest-Q mode.

The authors are grateful to N. F. Kovalev, M. I. Petelin, and G. G. Denisov for useful discussions.

This work was supported by the Russian Fund for Fundamental Research (Grant Nos. 97-02-16643 and 97-02-17379).

[1] N. F. Kovalev, M. I. Petelin, and M. G. Reznikov, Author's Certificate No. 720592, Byul. Izobret. No. 9 (1980).
[2] V. L. Bratman, N. S. Ginzburg, and G. G. Denisov, Pis'ma Zh. Tekh. Fiz **7**, 1320 (1981) [Sov. Tech. Phys. Lett. **7**, 565 (1981)].
[3] V. L. Bratman, G. G. Denisov, N. S. Ginzburg, and M. I. Petelin, IEEE J. Quantum Electron. **QE-19**, 282 (1983).
[4] M. Wang, Z. Wang, J. Chen, Z. Lu, and L. Zhang, Nucl. Instrum. Methods Phys. Res. A **304**, 116 (1991).
[5] K. Mima, T. Akiba, K. Imasaki, N. Ohigashi, Y. Tsunawaki, T. Taguchi, S. Kuruma, S. Nakai, and C. Yamanaka, Nucl. Instrum. Methods Phys. Res. A **304**, 93 (1991).
[6] T. S. Chu, F. Hartemann, B. G. Danly, and R. J. Temkin, Phys. Rev. Lett. **72**, 2391 (1994).
[7] P. Zambon, W. J. Witteman, and P. J. M. van der Slot, Nucl. Instrum. Methods Phys. Res. A **341**, 88 (1994).
[8] V. A. Bogachenkov, N. S. Ginsburg, A. A. Kaminskiĭ, A. K. Kaminskiĭ, N. Yu. Peskov, V. P. Sarantsev, S. N. Sedykh, A. P. Sergeev, and A. S. Sergeev, Pis'ma Zh. Tekh. Fiz **21**(22), 45 (1995) [Tech. Phys. Lett. **21**, 925 (1995)].
[9] N. S. Ginzburg, A. A. Kaminsky, A. K. Kaminsky, N. Yu. Peskov, S. N. Sedykh, A. P. Sergeev, and A. S. Sergeev, IEEE Trans. Plasma Sci. **26**, 536 (1998).
[10] A. M. Sessler, *Laser Acceleration of Particles* AIP Conf. Proc. p. 154 (1982).
[11] N. S. Ginzburg, N. Yu. Peskov, A. S. Sergeev, G. R. M. Robb, and A. D. R. Phelps, IEEE Trans. Plasma Sci. **24**, 770 (1996).
[12] A. A. Kaminsky, A. K. Kaminsky, and S. B. Rubin, Part. Accel. **33**, 189 (1990).
[13] M. E. Conde and G. Bekefi, Phys. Rev. Lett. **67**, 3082 (1991).
[14] N. Yu. Peskov, S. V. Samsonov, N. S. Ginzburg, and V. L. Bratman, Nucl. Instrum. Methods Phys. Res. A **407**, 107 (1998).

Translated by R. M. Durham

Formation of ArCl(B) molecules in a transverse volume discharge

A. K. Shuaibov, L. L. Shimon, A. I. Dashchenko, Yu. Yu. Neĭmet, and I. V. Shevera

Uzhgorod State University
(Submitted November 6, 1998)
Pis'ma Zh. Tekh. Fiz. **25**, 29–33 (June 12, 1999)

Results of optimizing a $\lambda = 175$ nm ArCl(B–X) emitter pumped by a transverse volume discharge are presented. The formation of ArCl(B) molecules was investigated in a plasma formed by mixtures of rare gases with HCl and Cl_2 molecules. It is shown that the Cl_2 molecule is the most efficient chlorine carrier and that neon at pressures $\geqslant 50$ kPa is the most efficient buffer gas. © *1999 American Institute of Physics.* [S1063-7850(99)00506-6]

Electric-discharge lasers and lamps using rare-gas halides are widely used in microelectronics, photochemistry, medicine, and other fields of science and technology.[1,2] Emitters using the B–X ArCl transition, which have one of the shortest wavelengths, 175 nm, have currently been little studied. Lasing in ArCl(B–X) was reported in Ref. 3, but its output characteristics were appreciably inferior to those of ArF emitters having a similar lasing wavelength $\lambda = 193$ nm (Ref. 4). This is mainly because of the small cross section for stimulated emission at $\lambda = 175$ nm in ArCl. It is therefore preferable to use ArCl(B–X) in sources of spontaneous vacuum ultraviolet radiation with pulse lengths $\leqslant 100-200$ ns. Various pulsed sources of vacuum ultraviolet radiation pumped by a transverse discharge[5–7] have been developed in the vacuum ultraviolet (within the transmission range of $\lambda\lambda = 110-190$ nm windows): 126 nm Ar_2^*, 146 nm Kr_2^*, and 172 nm Xe_2^*. These sources require expensive, heavy rare gases. The possibilities of developing simple, moderate-pressure, vacuum ultraviolet emitters at $\lambda = 175$ nm in ArCl have not been studied.

Here we report results of optimizing the active medium of an electric-discharge vacuum ultraviolet emitter using He(Ne)/Ar/Cl_2(HCl) mixtures.

A transverse volume discharge was ignited in a system of electrodes 18 cm long. The interelectrode gap was 2.2 cm and the width of the discharge region was between 0.5 and 0.7 cm. We used automatic spark preionization similar to that used in Ref. 8. The discharge was ignited using an LC circuit with a 30 nF capacitance and 9.4 nF peaking capacitance. A TGI1 1000/25 thyratron was used as the switch in the pulsed supply system. The radiation was recorded using a half-meter vacuum monochromator fabricated using a Seya–Namioka system. A 1200 lines/mm diffraction grating was used and the emitter was connected to the monochromator via a CaF_2 window. The radiation detector was an FÉU-142 photomultiplier with an LiF window. The monochromator and the section for the photomultiplier were evacuated to high vacuum. A side window having an aperture of 18×1.8 cm was provided in the emitter to pump extended media with vacuum ultraviolet radiation. A spectroscopic study of the plasma was made in the range 130–300 nm.

The radiation spectra of a transverse volume discharge in mixtures of rare gases with HCl and Cl_2 molecules revealed the highest-intensity radiation for 175 nm ArCl (B–X) and 258 nm Cl_2^*. The spectra also showed a broad weak band with a maximum at 199 nm, which we ascribed to the C–A ArCl transition.[9] For the discharges using mixtures of rare gases with Cl_2 molecules the 258 nm band was between two and three times brighter than that for HCl mixtures.

Figure 1 gives the brightness of ArCl (B–X) radiation as a function of the content of HCl molecules in a transverse volume discharge using an He/Ar/HCl mixture. The optimum HCl content, 80 Pa, is considerably lower than that for 308 nm XeCl and 222 nm KrCl emitters ($P_{opt} = 300-400$ Pa). Replacing HCl with Cl_2 molecules increases the brightness of the ArCl (B–X) radiation, and the optimum Cl_2 content is in the range 300–400 Pa. This difference in the efficiency of formation of ArCl(B) can be attributed to the absorption of vacuum ultraviolet radiation by HCl molecules. The experiments were carried out using charging voltages of $\leqslant 15$ kV.

Figure 2 gives the brightness of the ArCl (B–X) radiation as a function of the buffer gas pressure and also shows

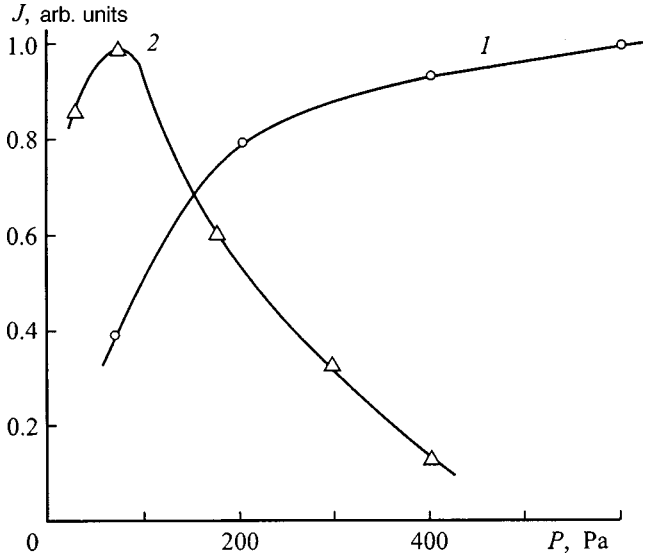

FIG. 1. Brightness of the $\lambda = 175$ nm ArCl (B–X) radiation band as a function of the content of HCl molecules in a He/Ar/HCl=48/8/[HCl] transverse discharge (*1*) and as a function of the Cl_2 content in an Ar/Cl_2 mixture (*2*) for [Ar]=5.3 kPa. Curves *1* and *2* are each normalized to their maxima.

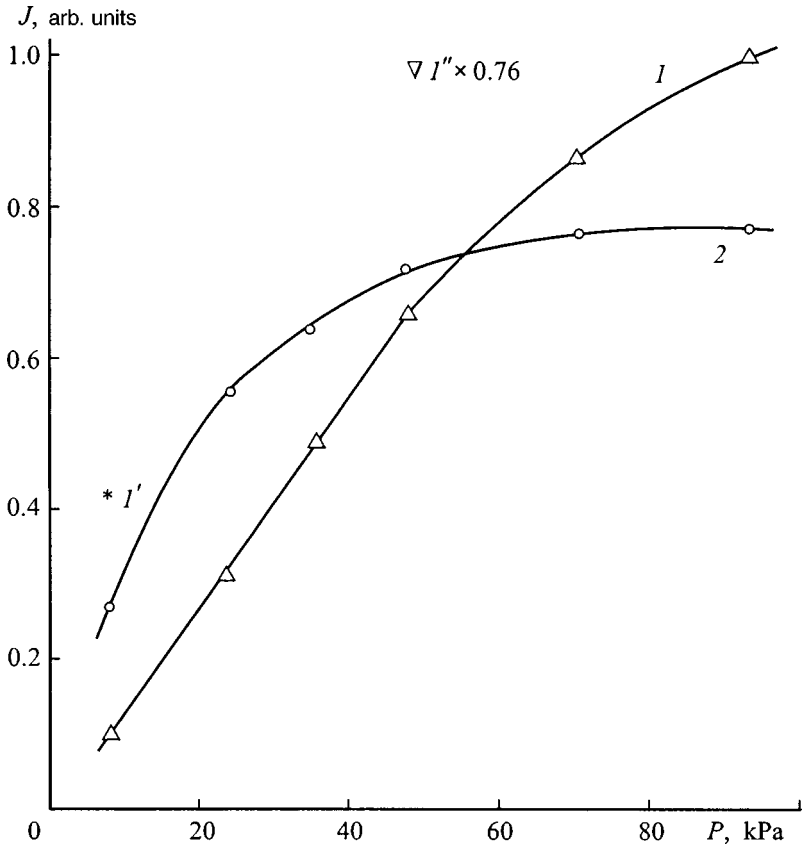

FIG. 2. Brightness of $\lambda = 175$ nm ArCl (B–X) radiation as a function of the Ne (*1*) and He content (*2*) in Ne(He)/Ar/HCl=[Ne(He)]/8/0.8 kPa discharges and brightness of ArCl (B–X) radiation in the following mixtures: *1′*—Ne/Ar/Cl_2=8/8/0.226 and *1″*—Ne/Ar/HCl=48/16/0.08 kPa.

comparative data on the ArCl brightness for a Cl_2 mixture and for an increased content of Ar atoms in the gas mixture. At mixture pressures $\leqslant 50$ kPa, He is the most efficient buffer gas, whereas at higher pressures Ne is best. The optimum argon content in the active mixtures is $\geqslant 16$ kPa. Using Cl_2 molecules in a transverse volume discharge in a reduced-pressure Ne/$ArCl_2$ mixture can enhance the brightness of the ArCl(B–X) radiation more than fourfold compared with a similar HCl mixture. The brightness of the $\lambda = 258$ nm Cl_2^* radiation band for discharges in He(Ne)/Ar/HCl mixtures also exhibits the same dependence on the buffer gas content as for the ArCl(B–X) band. The brightness of the $\lambda = 258$ nm Cl_2^* radiation is an order of magnitude higher for discharges in an Ne/Ar/Cl_2 mixture compared with a similar HCl mixture. Investigations of the service life of the ArCl(B–X) radiation showed that the brightness of the 175 nm ArCl band for a discharge in a Ne/Ar/HCl=48/16/0.08 kPa mixture was reduced by a factor of four after 10^4 discharge pulses.

Thus, optimizing the composition of a 175 nm ArCl (B–X) electric-discharge emitter showed that Cl_2 molecules are the best chlorine carriers at pressures of 300–400 Pa. At active mixture pressures $\leqslant 50$ kPa He is the most efficient buffer gas, whereas at higher pressures Ne is the most efficient. This discharge is also a source of $\lambda = 258$ nm Cl_2^* radiation, for which the optimal media are similar to those for ArCl emitters.

[1] J. Bendig, J. Inf. Rec. Mater. **15**, 385 (1987).
[2] V. Yu. Baranov, V. M. Borisov, and Yu. Yu. Stepanov, *Rare-Gas Halide Electric-Discharge Excimer Lasers* [in Russian], Énergoatomizdat, Moscow (1988), 216 pp.
[3] R. W. Waynant, Kvantovaya Élektron. (Moscow) **5**, 1767 (1978) [Sov. J. Quantum Electron. **8**, 1002 (1978)].
[4] C. P. Wang, Kvantovaya Élektron. (Moscow) **5**, 1771 (1978) [Sov. J. Quantum Electron. **8**, 1004 (1978)].
[5] T. Sakurai, N. Goto, and C. E. Webb, J. Phys. D: Appl. Phys. **20**, 709 (1987).
[6] A. A. Kuznetsov, V. S. Skakun, V. F. Tarasenko, and E. A. Fomin, Pis'ma Zh. Tekh. Fiz **19**(5), 1 (1993) [Tech. Phys. Lett. **19**, 133 (1993)].
[7] V. S. Skakun, V. F. Tarasenko, E. A. Fomin, and A. A. Kuznetsov, Zh. Tekh. Fiz. **64**(10), 146 (1994) [Tech. Phys. **39**, 1054 (1994)].
[8] A. K. Shuaibov, Pis'ma Zh. Tekh. Fiz **24**(1), 85 (1998) [Tech. Phys. Lett. **24**, 38 (1998)].
[9] M. H. R. Hutchinson, Appl. Phys. **21**, 95 (1980).

Translated by R. M. Durham

Theory of multiple scattering in a fractal medium

V. V. Uchaĭkin and D. A. Korobko

Ulyanovsk State University
(Submitted November 17, 1998)
Pis'ma Zh. Tekh. Fiz. **25**, 34–40 (June 12, 1999)

An analysis is made of multiple scattering of particles whose ranges have a power-law distribution corresponding to a fractal medium. The small-angle approximation is used to derive an expression for the angular distribution of particles which have traversed a specific path. The results of numerical calculations are presented. © *1999 American Institute of Physics.* [S1063-7850(99)00606-0]

West[1] and Zosimov and Lyamshev[2] have reported theoretical analyses of the scattering of waves by inhomogeneous self-similar structures (fractals). The need for such calculations has been stimulated by studies of structures such as amorphous polymers, colloidal aggregates and aggregates formed in air from microscopic solid-phase particles, porous materials such as porous aerogels, and so on.[3] In the present paper we consider the multiple scattering of particles in a fractal medium made up of a random distribution of scattering centers with power-law long-range correlations.[4]

In the small-angle approximation the deflection of a particle from its initial direction is described by the two-dimensional vector θ (see, for example, Ref. 5). Let us assume that $\sigma(\theta)$ is the angular distribution of a particle being scattered once by an isolated atom, $\int \sigma(\theta)d\theta=1$, and then the distribution of a particle having undergone n scattering events is given by the multiple convolution of these distributions:

$$\sigma^{(n+1)}(\theta)=\int \sigma(\theta')\sigma^{(n)}(\theta-\theta')d\theta', \tag{1}$$

where $\sigma^{(0)}(\theta)\equiv\delta(\theta)$. The angular distribution of particles which have traversed the path x is given by

$$\Psi(\theta,x)=\sum_{n=0}^{\infty} p_n(x)\sigma^{(n)}(\theta), \tag{2}$$

where $p_n(x)$ is the probability that over the path x the particle will undergo exactly n scattering events. This probability characterizes the medium and is related to the distribution density of the mean free path $q(x)$ by

$$p_n(x)=\int_0^x Q(x-x')q^{(n)}(x')dx', \tag{3}$$

where

$$Q(x)=\int_x^{\infty} q(x')dx'$$

is the probability that a random range exceeds x and $q^{(n)}(x)$ is a multiple convolution of the distributions $q(x)$ describing the distribution of the coordinate of the nth collision point. In this notation, the distribution is given by

$$\Psi(\theta,x)=\sum_{n=0}^{\infty} \sigma^{(n)}(\theta)\int_0^x Q(x-x')q^{(n)}(x')dx'. \tag{4}$$

In the classical theory of multiple scattering, the scattering centers are assumed to be distributed independently with a constant (for a homogeneous medium) average density. In this case, the mean free path distribution has the form

$$q_0(x)=\mu\exp(-\mu x), \tag{5}$$

where μ is the linear scattering coefficient, which is the reciprocal of the mean free path. Since $q_0^{(n)}(x)=\mu(\mu x)^{n-1}\exp(-\mu x)/(n-1)!$ and $Q_0(x)=\exp(-\mu x)$, the angular distribution (2) is described by the generalized Poisson distribution[6]

$$\Psi_0(\theta,x)=\exp(-\mu x)\sum_{n=0}^{\infty}\frac{(\mu x)^n}{n!}\sigma^{(n)}(\theta). \tag{6}$$

For $x\to\infty$ the average random number of terms increases as μx, and its relative fluctuations decrease as $\sim(\mu x)^{-1/2}$. Since for large n we have

$$\sigma^{(n)}(\theta)\sim\frac{1}{2\pi n\langle\Theta^2\rangle}\exp\{-\theta^2/[2n\langle\Theta^2\rangle]\}, \tag{7}$$

where

$$\langle\Theta^2\rangle=\int \theta^2\sigma(\theta)d\theta$$

is the mean square of the single scattering angle, the angular distribution for large depths has the form

$$\Psi_0(\theta,x)\sim\frac{1}{2\pi\mu x\langle\Theta^2\rangle}\exp\{-\theta^2/[2\mu x\langle\Theta^2\rangle]\},\quad x\to\infty, \tag{8}$$

obtained by Fermi[7] for multiple Coulomb scattering of charged particles.

The fractal distribution of the random points $\{x_i\}$ on a straight line is described by a power dependence of the average number $\overline{N}(x)$ of points on the section $[x_i,x_i+x]$, one end of which coincides with one of the fractal points:

$$\overline{N}(x)\sim Ax^{\alpha},\quad x\to\infty, \tag{9}$$

where $\alpha<1$ is the fractal dimension (for $\alpha=1$ we have the homogeneous Poisson ensemble considered above). In this case, we have

$$q(x)\sim\alpha Bx^{-\alpha-1},\quad x\to\infty, \tag{10}$$

and from the theory of stable distributions[8]

$$q_0^{(n)}(x)\sim[nB\Gamma(1-\alpha)]^{-1/\alpha}g^{(\alpha)}((nB\Gamma(1-\alpha))^{-1/\alpha}x),$$
$$n\to\infty, \tag{11}$$

where $g^{(\alpha)}(x)$ is the one-sided density of the stable law whose Laplace transform (in the form B) can be written

$$\tilde{g}^{(\alpha)}(\lambda)\equiv\int_0^\infty g^{(\alpha)}(x)e^{-\lambda x}dx=\exp(-\lambda^\alpha). \tag{12}$$

The densities $g^{(\alpha)}(x)$, like the normal density, describe the limiting distribution of a sum of independent random quantities but unlike the normal density, they belong to distributions of the type (10) whose mathematical expectation is infinite.

Introducing the notation

$$Q^{(n)}(x)=\int_x^\infty q^{(n)}(x')dx',\quad G^{(\alpha)}(x)=\int_0^x g^{(\alpha)}(x')dx',$$

we write the probability that over the path x a particle will undergo n collisions:

$$p_n(x)=Q^{(n+1)}(x)-Q^{(n)}(x)$$
$$=G^{(\alpha)}((nB\Gamma(1-\alpha))^{-1/\alpha}x)-G^{(\alpha)}([(n+1)$$
$$\times B\Gamma(1-\alpha)]^{-1/\alpha}x). \tag{13}$$

Expressing the argument of the subtrahend function in the form

$$[(n+1)B\Gamma(1-\alpha)]^{-1/\alpha}x=[nB\Gamma(1-\alpha)]^{-1/\alpha}x$$
$$-[nB\Gamma(1-\alpha)]^{-1/\alpha}x(n\alpha)^{-1} \tag{14}$$

and expanding this as a series, we obtain the asymptotic expression

$$p_n(x)\sim[nB\Gamma(1-\alpha)]^{-1/\alpha}x(n\alpha)^{-1}g^{(\alpha)}$$
$$\times([nB\Gamma(1-\alpha)]^{-1/\alpha}x),\quad x\to\infty. \tag{15}$$

Then, using expression (7) again and converting in expression (2) from summation over n to integration with respect to the variable

$$\tau=[nB\Gamma(1-\alpha)]^{-1/\alpha}x,$$

we arrive at the distribution

$$\Psi(\theta,x)\sim(4Dx^\alpha)^{-1}f^{(\alpha)}(|\theta|/\sqrt{4Dx^\alpha}),\quad x\to\infty, \tag{16}$$

where

$$D=\frac{\langle\Theta^2\rangle\Gamma(1+\alpha)}{2B(\Gamma(1-\alpha))^2},$$

and

$$f^{(\alpha)}(u)=\pi^{-1}\int_0^\infty d\tau e^{-u^2\tau^\alpha}\tau^\alpha g^{(\alpha)}(\tau),\quad \alpha<1. \tag{17}$$

For $\alpha\to1$ we obtain $g^{(\alpha)}(\tau)\to\delta(\tau-1)$ and $f^\alpha(u)$ becomes a Gaussian distribution, but for $\alpha<1$ we obtain a different distribution, which has a logarithmic singularity at zero

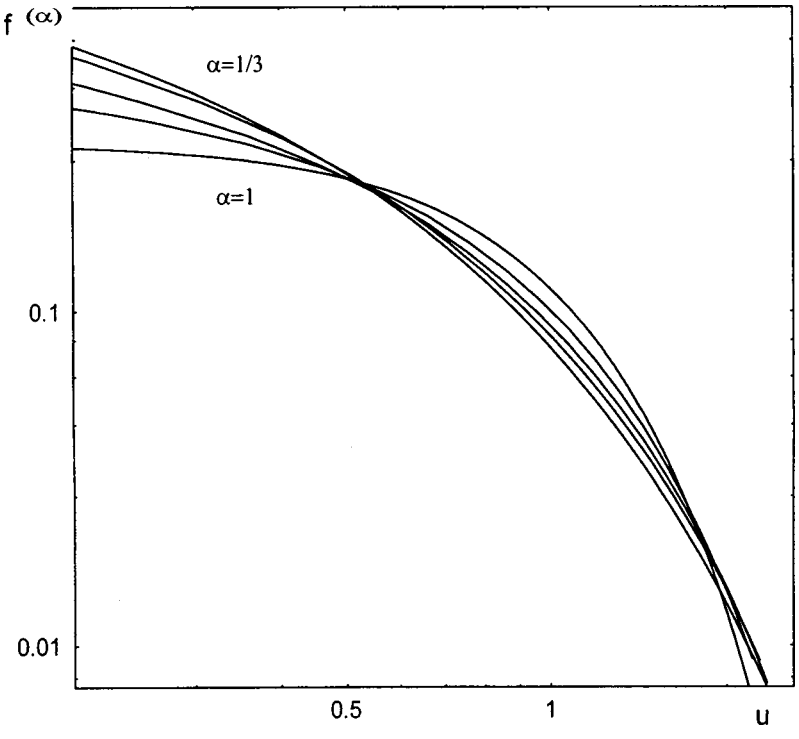

FIG. 1. Distributions of $f^\alpha(u)$ for the exponents α = 1/3, 1/2, 2/3, 5/6, and 1.

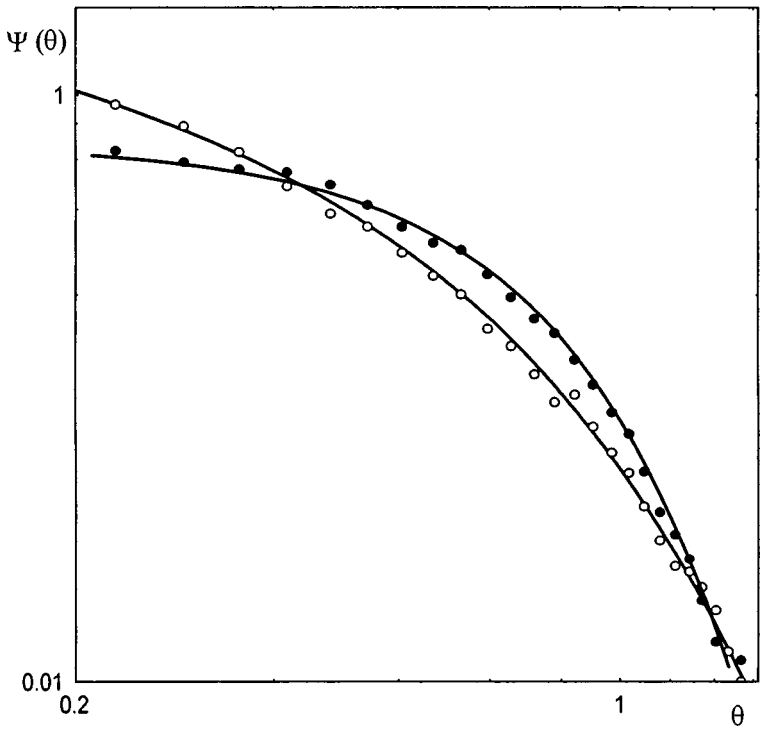

FIG. 2. Angular distributions of multiply scattered particles $\Psi_0(\theta)$ (8) and $\Psi(\theta)$ (16) for $\alpha=1/2$ for a thickness corresponding to an average of 500 collisions. The mean-square angles of single scattering $\langle\Theta^2\rangle$ are the same. The circles give the results of a Monte Carlo simulation (10 000 histories). The filled circles correspond to a homogeneous medium having the exponential range distribution (5) and the open circles corresponds to a fractal medium having the power-law distribution of ranges (10).

$$f^{\alpha}(u)\sim[2\pi\Gamma(1-\alpha)]^{-1}|\ln u|, \quad u\to 0; \tag{18}$$

outside this region, however, it is described by the asymptotic expression

$$f^{\alpha}(u)\sim \frac{\alpha^{(3\alpha-2)/2(2-\alpha)}}{\pi\sqrt{2-\alpha}}u^{-2(1-\alpha)/(2-\alpha)} \times\exp\{-(2-\alpha)\alpha^{\alpha/(2-\alpha)}u^{2/(2-\alpha)}\}. \tag{19}$$

The results of numerical calculations using Eq. (17) for several exponents α, including the limiting case $\alpha=1$, are plotted in Fig. 1. The mean-square angle of multiple scattering is calculated analytically:

$$\overline{\theta^2}(x)=\frac{4}{\Gamma(\alpha+1)}Dx^{\alpha}. \tag{20}$$

The angular distribution of multiply scattered particles in a fractal medium exhibits a slower increase in width $\propto x^{\alpha/2}$ as compared with $\propto x^{1/2}$ for a homogeneous medium. The form of the distribution (16) differs from the normal distribution in having a higher probability concentration at small and large angles (Fig. 2).

Both the width and the form of the angular distribution of particles undergoing multiple scattering in a fractal medium can be used to determine experimentally the fractal dimension α of an inhomogeneous structure.

This work was supported by the Russian Fund for Fundamental Research (Grant No. 98-01-03307).

[1] B. J. West, J. Opt. Soc. Am. A **6**, 1074 (1990).
[2] V. V. Zosimov and L. M. Lyamshev, Usp. Fiz. Nauk **165**, 361 (1995).
[3] *Fractals in Physics: Proceedings of the Sixth International Symposium on Fractals in Physics*, edited by L. Pietronero and E. Tosatti (North Holland, Amsterdam, 1986; Mir, Moscow, 1988, 672 pp.)
[4] V. V. Uchaikin and G. G. Gusarov, J. Math. Phys. **38**(5), 5 (1997).
[5] A. I. Kol'chuzhkin and V. V. Uchaĭkin, *Introduction to the Theory of Particle Propagation Through Matter* [in Russian], Atomizdat, Moscow (1978), 256 pp.
[6] W. Feller, *An Introduction to Probability Theory and its Applications*, 3rd ed. (Wiley, New York, 1967) [Russ. transl., later ed, Vol. 2, Mir, Moscow 1984, 752 pp.]
[7] E. Fermi, Phys. Rev. **63**, 485 (1940).
[8] V. M. Zolotarev, *One-Dimensional Stable Distributions*, Amer. Math. Soc, Providence, RI (1986) [Russian original, Nauka, Moscow (1983), 304 pp].

Translated by R. M. Durham

Quantum-dot injection heterolaser with 3.3 W output power

A. R. Kovsh, D. A. Livshits, A. E. Zhukov, A. Yu. Egorov, M. V. Maksimov, V. M. Ustinov, I. S. Tarasov, N. N. Ledentsov, P. S. Kop'ev, Zh. I. Alferov, and D. Bimberg

A. F. Ioffe Physicotechnical Institute, Russian Academy of Sciences, St. Petersburg Institut für Festkörperphysik, Technische Universität Berlin, Hardenbergstr. 36, D-10623 Berlin, Germany
(Submitted March 1, 1999)
Pis'ma Zh. Tekh. Fiz. **25**, 41–46 (June 12, 1999)

Continuous-wave lasing has been achieved via the ground state of composite vertically coupled InAlAs/InGaAs quantum dots in an AlGaAs matrix with a room temperature output power of 3.3 W at both mirrors. © *1999 American Institute of Physics.* [S1063-7850(99)00706-5]

Over the last few years structures with self-organized quantum dots have been attracting increasing interest in semiconductor physics.[1] The main difference between these and quantum-well structures is their delta-function density of states, which suggests that the characteristics of semiconductor lasers may be drastically improved.[2,3] To date considerable progress has been achieved in this direction. In various systems of materials, lasing has been achieved via the quantum-dot ground state with threshold current densities of 63 A/cm^2 (Ref. 4) and 11 A/cm^2 (Ref. 5) at room temperature and at liquid nitrogen temperature, respectively.

The possibility of achieving high output powers in quantum-dot laser diodes has not yet been adequately studied. In Ref. 6 we reported cw lasing in a structure with an InGaAs/AlGaAs quantum-dot active region with an output power of 1 W at room temperature. By improving the quantum dot formation process,[7] we succeeded in increasing this value to 1.5 W (Ref. 8). Here we report a self-organized quantum-dot laser with a maximum output power of 3.3 W.

One of the main mechanisms limiting the power of semiconductor lasers is spectral hole burning (see Ref. 9 and the literature cited therein) caused by the finite rate of carrier trapping at states involved in the lasing. Since the trapping times in InGaAs/AlGaAs quantum-dot structures are fairly long (tens of picoseconds[10]) and an array of quantum dots has a finite number of states determined by its surface concentration, there has long been some skepticism regarding the use of quantum dots for laser applications requiring high radiation powers. The quantum-dot concentration can be increased by using several layers of quantum dots[11] and also by forming these on vicinal surfaces.[12] In Ref. 7 we proposed an alternative approach which can enhance the surface concentration of quantum dots in each layer. The basic idea of this approach involves using denser arrays of InAlAs quantum dots as centers for the stimulated formation of InGaAs quantum dots directly involved in the lasing. Ultimately an array of composite, vertically-coupled quantum dots is formed whose surface concentration is defined by the InAlAs quantum dots, whereas the optical transition energy is determined by the InGaAs quantum dots. This method was used to form the active region in the laser studied here.

The structure was grown by molecular beam epitaxy on an n^+-GaAs(100) substrate using a solid As_4 source in a Riber 32P system. We selected a standard double-hetero-

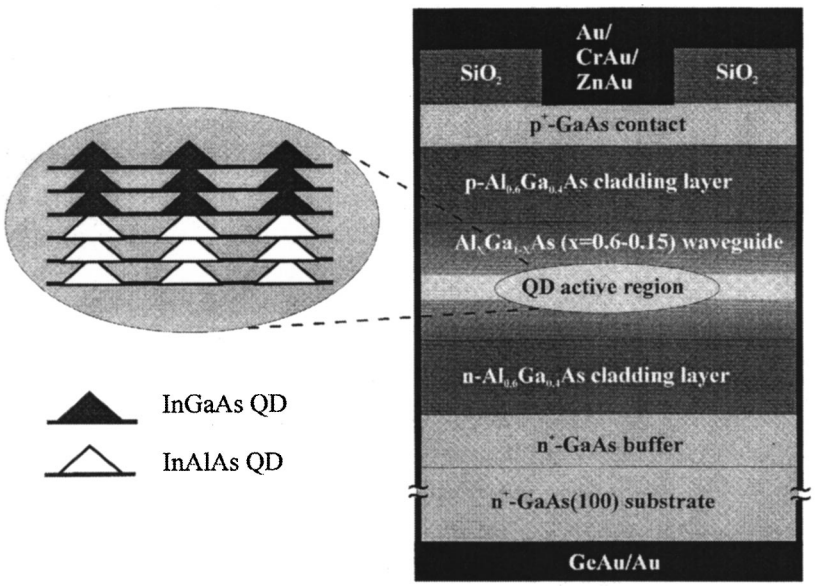

FIG. 1. Schematic of laser diodes with active region formed by composite vertically-coupled InAlAs/InGaAs quantum dots in an AlGaAs matrix.

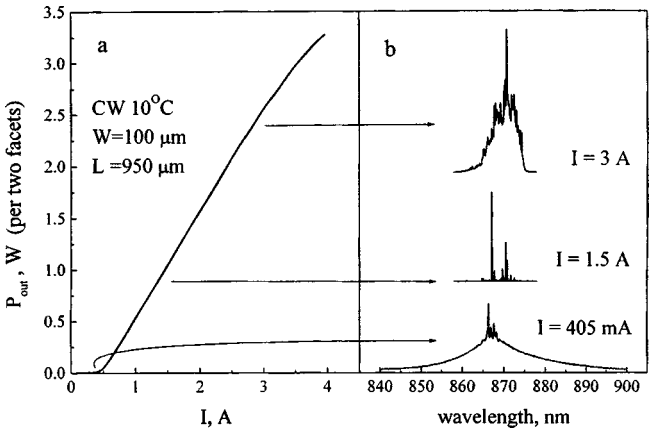

FIG. 2. Watt–ampere characteristics of cw laser at 10 °C (a); lasing spectra at various pump currents (b).

structure geometry with separate carrier and lightwave confinement, and a graded-index waveguide. The structure is shown schematically in Fig. 1 and the inset shows an image of a cross section through the active region, which was positioned at the center of the 0.5 μm thick waveguide layer and consisted of an array of composite vertically-coupled quantum dots. The first three layers of quantum dots were formed by depositing 5.3 ML thick InAlAs layers separated by 5 nm thick $Al_{0.15}GaAs$ spacers and then depositing three layers of InGaAs quantum dots, separated by the same spacers. The transition from two-dimensional to three-dimensional growth of the In-containing layers was observed directly during the growth process from the appearance of a shaded reflection high-energy electron diffraction (RHEED) pattern. The growth temperature during deposition of the active region was 485 °C, whereas the substrate temperature during growth of the waveguide and the emitters was 600 °C and 700 °C, respectively. The entire structure was grown in an arsenic-enriched environment, standard for molecular beam epitaxy.

This structure was used to fabricate stripe lasers of width $W=100\,\mu$m using ''wide contact'' technology. The insulator forming the stripe contact was a 0.2 μm thick layer of SiO_2 deposited by magnetron sputtering of silicon in an oxygen atmosphere. A contact with the p^+-GaAs layer was made by depositing and brazing ZnAu and CrAu alloys and also strengthening with gold to achieve better indium wetting during the subsequent soldering onto the heat sink. A contact with the n^+-substrate was made by depositing GeAu and strengthening with gold. No dielectric coatings were deposited on the mirrors.

The *p*-sides of the lasers were indium-soldered to a copper heat sink and measurements were made under cw conditions at a heat sink temperature of 10 °C. Figure 2a shows the power–current characteristic of a laser diode with a cavity of length $L=950\,\mu$m. Figure 2b shows the electroluminescence spectra of this laser at various pump currents. The threshold current was $I_{th}=402$ mA, which corresponds to a current density of 423 A/cm^2. The maximum radiation power (P_{out}) and the differential quantum efficiency (η_d) on the linear section of the characteristic for both mirrors were 3.28 W and 73%, respectively. Above 2.7 A, the power–current characteristic begins to curve as a result of heating of the laser active region, which leads to a regular long-wavelength shift of the lasing maximum.

The method of increasing the surface concentration of quantum dots used in the present study can increase the maximum current flowing through the structure in the lasing regime, which is limited by the finite number of quantum dots and the carrier trapping time in these dots. It can also reduce the population of matrix states for the same level of pumping, which can then reduce the parasitic currents and overheating of the structure caused by recombination via higher states. Both these factors are extremely important for achieving a high output power.

To sum up, we have achieved an output power of 3.3 W from a quantum-dot laser, which is the highest power recorded for quantum-dot lasers, and we have thereby demonstrated that these lasers can be used for applications requiring a high output power.

This work was supported by INTAS Program No. 96-0467 and by the program BMBF 13 No. 7231.

[1] L. Goldstein, F. Glas, J. Y. Marzin, M. N. Charasse, and G. Le Roux, Appl. Phys. Lett. **47**, 1099 (1985).
[2] Y. Arakawa and H. Sakaki, Appl. Phys. Lett. **40**, 939 (1982).
[3] M. Asada, Y. Miyamoto, and Y. Suematsu, IEEE J. Quantum Electron. **QE-22**, 1915 (1986).
[4] V. M. Ustinov, A. Yu. Egorov, A. R. Kovsh, A. E. Zhukov, M. V. Maksimov, A. F. Tsatsul'nikov, N. Yu. Gordeev, S. V. Zaitsev, Yu. M. Shernyakov, N. A. Bert, P. S. Kop'ev, Zh. I. Alferov, N. N. Ledentsov, J. Bohrer, D. Bimberg, A. O. Kosogov, P. Werner, and U. Gosele, J. Cryst. Growth **175**, 689 (1997).
[5] V. M. Ustinov, A. E. Zhukov, A. Yu. Egorov, A. R. Kovsh, S. V. Zaitsev, N. Yu. Gordeev, V. I. Kopchatov, N. N. Ledentsov, A. F. Tsatsul'nikov, B. V. Volovik, P. S. Kop'ev, Zh. I. Alferov, S. S. Ruvimov, Z. Liliental-Weber, and D. Bimberg, Electron. Lett. **34**, 670 (1998).
[6] Yu. M. Shernyakov, A. Yu. Egorov, A. E. Zhukov, S. V. Zaĭtsev, A. R. Kovsh, I. L. Krestnikov, A. V. Lunev, N. N. Ledentsov, M. V. Maksimov, A. V. Sakharov, V. M. Ustinov, Chao Chen, P. S. Kop'ev, Zh. I. Alferov, and D. Bimberg, Pis'ma Zh. Tekh. Fiz **23**(4), 51 (1997) [Tech. Phys. Lett. **23**, 149 (1997)].
[7] A. R. Kovsh, A. E. Zhukov, A. Yu. Egorov, V. M. Ustinov, Yu. M. Shernyakov, M. V. Maksimov, A. F. Tsatsul'nikov, B. V. Volovik, A. V. Lunev, N. N. Ledentsov, P. S. Kop'ev, Zh. I. Alferov, and D. Bimberg, Fiz. Tekh. Poluprovodn **32**, 1114 (1998) [Semiconductors **32**, 997 (1998)].
[8] Yu. M. Shernyakov, A. Yu. Egorov, B. V. Volovik, A. E. Zhukov, A. R. Kovsh, A. V. Lunev, N. N. Ledentsov, M. V. Maksimov, A. V. Sakharov, V. M. Ustinov, Zhen Zhao, P. S. Kop'ev, Zh. I. Alferov, and D. Bimberg, Pis'ma Zh. Tekh. Fiz **24**(9), 50 (1998) [Tech. Phys. Lett. **24**, 351 (1998)].
[9] N. Kirstaedter, O. Schmidt, N. N. Ledentsov, M. Grundmann, D. Bimberg, V. M. Ustinov, A. Yu. Egorov, A. E. Zhukov, M. V. Maximov, P. S. Kop'ev, Zh. I. Alferov, A. O. Kosogov, U. Gosele, and J. Heydenreich, IEEE **1**, 290 (1995).
[10] T. Makino, J. D. Evans, and G. Mak, Appl. Phys. Lett. **71**, 2871 (1997).
[11] Q. Xie, A. Madhukar, P. Chen, and N. Kobayashi, Phys. Rev. Lett. **75**, 2542 (1995).
[12] V. P. Evtikhiev, I. V. Kudryashov, E. Yu. Kotel'nikov, V. E. Tokranov, A. N. Titkov, I. S. Tarasov, and Zh. I. Alferov, Fiz. Tekh. Poluprovodn **32**, 1482 (1998) [Semiconductors **32**, 1323 (1998)].

Translated by R. M. Durham

Fabrication of cerium oxide films on sapphire by rf magnetron sputtering

E. K. Hollmann, S. V. Razumov, and A. V. Tumarkin

State Electrotechnical University (LETI), St. Petersburg
(Submitted February 2, 1999)
Pis'ma Zh. Tekh. Fiz. **25**, 47–51 (June 12, 1999)

Results are presented of experiments to fabricate preferentially (200) oriented CeO_2 films without mechanical stresses on Al_2O_3 substrates. © *1999 American Institute of Physics.* [S1063-7850(99)00806-X]

The use of high-temperature superconducting and ferroelectric films in microwave instruments and devices imposes various constraints on the films themselves and on the substrate materials. First, the substrate material should be suitable for growing epitaxial films and second, the dielectric properties of the substrate should satisfy the constraints imposed by the microwave applications.

A promising substrate material for depositing high-temperature superconducting and ferroelectric films (especially STO) for microwave applications is sapphire (Al_2O_3) (Ref. 1). However, at the high deposition temperatures required for epitaxial growth, chemical interaction may take place between the growing film and the sapphire. The difficulties involved in fabricating films such as YBCO and strontium titanate on sapphire are compensated by their good dielectric properties and high mechanical strength.

The problem of matching the substrate and growing film materials from the point of view of crystalline compatibility and interdiffusion between the substrate elements and the film may be solved by using buffer layers. Materials chemically and structurally matched with YBCO and STO are used as a buffer layer for sapphire. Commonly used compounds include $PrBa_2Cu_3O_7$, zirconium oxide stabilized with yttrium, cerium dioxide, and others.[1]

Cerium dioxide is currently one of the most promising buffer layers for fabricating YBCO and STO films on sapphire.[2] The crystal lattice of cerium dioxide, which exhibits cubic symmetry with $a=5.420$ Å, is matched with the oriented (r-cut) lattice of Al_2O_3 and with the lattices of strontium titanate and YBCO. In addition, the linear coefficient of thermal expansion of cerium dioxide is similar to the thermal coefficients of STO and YBCO.

The quality of the CeO_2 buffer layer, and specifically the existence of blocks having only one orientation or blocks having different orientations to the substrate surface as well as the tensile or compressive strain of the lattice in many respects determine the subsequent growth of structurally perfect YBCO and STO films.

In the present study we investigated the growth of cerium oxide films on r-oriented sapphire substrates in order to obtain coatings of this buffer layer preferentially oriented in the (200) direction to the substrate surface with minimum lattice strains.

The cerium oxide films were prepared by rf magnetron sputtering of a ceramic CeO_2 target. The films were deposited in a pure oxygen atmosphere. The preliminary sputtering time with the baffle closed was 15–20 min. The working pressure decreased from 60 Pa at the beginning of the deposition process to 8 Pa after 30 min and then remained constant during growth of the film. The total time taken to de-

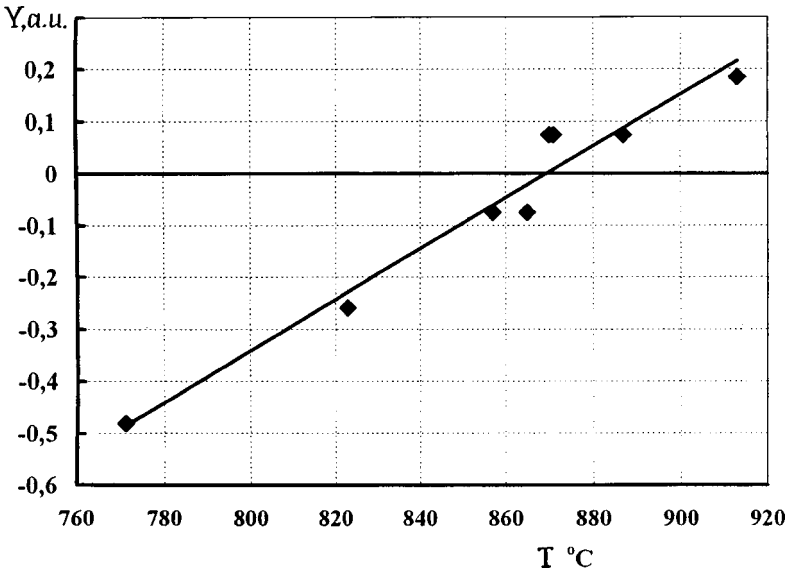

FIG. 1. Stress of CeO_2 films versus temprature of substrate holder.

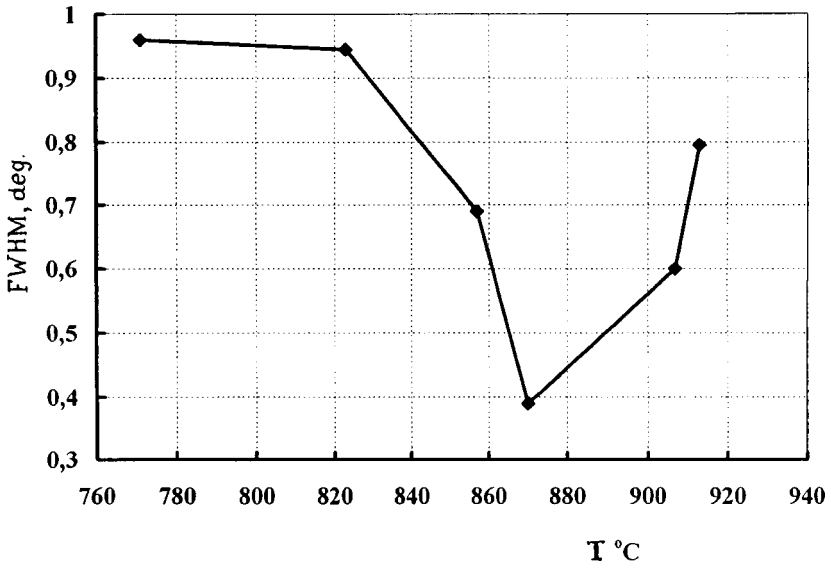

FIG. 2. Overall width of (200) peak versus temperature of substrate holder.

posit the film was 120 min. The temperature of the substrate heater was varied between 770 and 910 °C during the deposition process. After the growth had ended, the films were cooled in pure oxygen at atmospheric pressure.

The phase composition and structural quality of the CeO_2 films were investigated by x-ray diffractometry.

An analysis of the phase composition of the CeO_2 films showed that depending on the synthesis temperature, the film is either preferentially oriented, with the (200) orientation relative to the substrate surface, or it contains two phases oriented in the (200) and (111) directions. The films of mixed orientation, containing both the (200) and (111) phases, form at lower synthesis temperatures than the films having preferentially (200)-oriented blocks. The analysis was made by comparing the integrated intensities of the (200) and (111) peaks normalized to the corresponding intensities measured for powder samples.[3]

In order to obtain a more accurate estimate of the temperature range for synthesis to produce cerium oxide films preferentially oriented in the (200) direction and having lattice parameters corresponding to those of the single-crystal samples, we made a detailed analysis of the x-ray diffraction patterns of these samples, which can be used to determine the tensile or compressive strain of the lattice. The analysis was made by comparing the interplanar spacings measured for the (200) phase of the films with the interplanar spacing for the same phase of a powder sample

$$Y = \frac{d - d_p}{d_p} \times 100,$$

where Y is the relative stress of the film, d is the interplanar spacing for the samples, and d_p is the interplanar spacing for the powder sample.

Figure 1 gives the lattice strain which determines the total stress of the film, plotted as a function of the synthesis temperature. The results suggest that in our case, the optimum temperature of the substrate holder is ~870 °C. The films obtained at this temperature exhibit the lowest lattice stress in the absence of any (111)-oriented phase inclusions.

Figure 2 gives the overall width of the (200) peak as a function of the temperature of the substrate holder, which indicates the structural quality of the (200) phase. It should be noted that the synthesis temperature which yields CeO_2 films preferentially oriented in the (200) direction to the substrate surface with the minimum lattice stresses (Fig. 1) is also optimum from the point of view of crystallite sizes. The absence of any stresses in the films obtained at substrate holder temperatures of ~870° C suggests that at the optimum synthesis temperature the absolute value of the (200) peak width is clearly only determined by the region of coherent scattering of the x-rays in the film.

To conclude, these investigations suggest that the temperature of the substrate holder during the film growth process is one of the determining factors for the formation of high-quality cerium oxide films. The presence of a minimum in the temperature dependence of the x-ray peak indicates that there is an optimum temperature for the synthesis of CeO_2 films. In our case, the optimum heater temperature is ~870° C. Thus, this growth regime can produce structurally perfect CeO_2 buffer layer films, which opens up extensive possibilities for the subsequent fabrication of high-quality YBCO and STO films on sapphire.

[1] E. K. Hollmann, O. G. Vendik, and A. G. Zaitsev, Supercond. Sci. Technol. **7**, 609 (1994).
[2] A. G. Zaitsev and G. Ockenfuss, J. Appl. Phys. **81**, 3069 (1997).
[3] F. Vassenden, G. Linker, and J. Geerk, Physica C **175**, 566 (1991).

Translated by R. M. Durham

Possibility of nondestructive layer-by-layer analysis of multilayer structures of ultrathin films using low-energy hydrogen ions

V. A. Kurnaev, N. N. Trifonov, M. N. Drozdov, and N. N. Salashchenko

Moscow Engineering Physics Institute
(Submitted January 14, 1999)
Pis'ma Zh. Tekh. Fiz. **25**, 52–56 (June 12, 1999)

The possibility of nondestructive monitoring of the distribution of the composition in multilayer structures was investigated experimentally by analyzing the energy spectra of scattered hydrogen ions. © *1999 American Institute of Physics.* [S1063-7850(99)00906-4]

Progress in the field of micro- and nanotechnology has attached increasing importance to monitoring the parameters of thin and ultrathin layers of different composition. The most widely used method of studying their composition and depth profile is layer-by-layer analysis by various methods of ion beam sputtering[1] (such as Auger spectroscopy, secondary ion mass spectroscopy, scattering spectroscopy, recoil atoms, and others). However, in these methods of analysis the depth resolution is at most 3 nm and the region being analyzed is effectively destroyed. Rutherford backscattering can be used for nondestructive layer-by-layer analysis, although this requires expensive equipment and the depth resolution is poor. Using light ions with energies of hundreds of kiloelectronvolts can improve the resolution to 1 nm (Ref. 2). Here we present results of an investigation into the possibility of using hydrogen ions having energies of a few kiloelectronvolts.

The experimental geometry is shown in Fig. 1. We used a molecular deuterium ion beam having energies in the range 9–15 keV and a current of 50–150 nA, for which the degree of energy homogeneity was 0.03 and the angular divergence 0.01 rad. The energy spectra of the scattered ions were recorded using an automatic electrostatic sector analyzer with an energy resolution of 0.004 and an aperture ratio of 7.4×10^{-4} sr. The analyzer could be turned through the angle ψ relative to the direction of the primary beam and the other experimental conditions were as Ref. 3. The target consisted of ten alternate layers of B_4C and Mo, 4.3 nm and 0.6 nm thick, respectively,[4] for which the results of a layer-by-layer Auger analysis were reported in Ref. 5.

Figure 2 shows the high-energy part of the deuteron spectrum scattered at an angle of 60° when the target was bombarded by a 12 keV ion beam. It is natural to assume that the 3.3 keV peak corresponds to particles reflected from the first Mo layer beneath the surface of the target. We used the SCATTER computer code,[3] which is qualitatively similar to the well-known TRIM pair collision code,[6] to make a comparison with the experimental results and to optimize possible values of the characteristic angles and parameters of the probe particle beam. The KrC potential was taken as the interaction potential and the inelastic energy losses were calculated from the Owen–Robinson formula using the Bragg rule for multicomponent targets.[6] We calculated 10^7 trajectories to simulate each spectrum. The results of the calculations plotted in Fig. 2 show that the computer code accurately predicts the position of the peak on the energy scale but not its shape. (Note that if the energy dependence of the probability of positive ion formation is assumed to have some influence, this gives a difference in the peak energy of less than 1%).

The position of the peak determined by the most probable energy loss ΔE can also be estimated from the simple single-deflection model usually used to analyze the scattering of high-energy ions:[6]

$$\Delta E \approx kL\{1/\sin\alpha + 1/\sin(\psi-\alpha)\}E^{1/2} + \Delta E_{\mathrm{el}}, \qquad (1)$$

where k is the proportionality factor in the dependence of the inelastic energy losses on the root of the energy, L is the thickness of the B_4C layer, and ΔE_{el} is the energy lost in an elastic collision between a particle and an Mo atom. The calculations using this simple formula describe the measured dependence of ΔE on the scattering angle with a relative accuracy of at least 0.15.

The error in determining the position of the peak from the experimental spectrum can be estimated as ± 40 keV. The energy losses are determined with a relative accuracy of 0.07, which corresponds to determining the thickness of the B_4C layer to within ~ 0.3 nm.

The position of the peak on the energy scale, like its relative amplitude, depends on the angles α and ψ but the scattering angle ψ, has a greater influence: as ψ increases, the relative peak height above the minimum in the spectrum increases, whereas the most probable energy loss decreases, saturating at $\psi > 90°$. Any variation of the initial energy within the range specified above has no significant influence on the accuracy of determining the peak parameters. By measuring the position of the peak for scattering angles $\psi < 50°$ we can determine the value of kL with a high degree of accuracy and thereby determine the layer thickness or, by measuring this independently, we can find the stopping power of the material. The fact that the width of the measured peak exceeds the calculated value can be attributed to various factors which were neglected in the computer simulation, i.e., the fluctuations of the B_4C layer thickness and also the possible influence of the dissociation of primary molecular ions on the particle energy distribution. Since the energy losses of particles reflected by the molybdenum layer

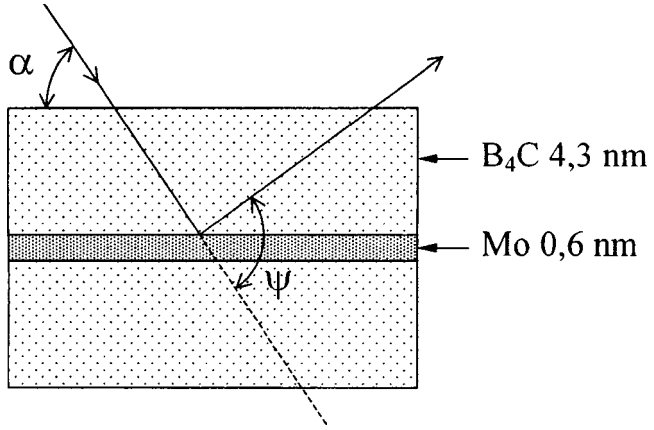

FIG. 1. Schematic of experiment.

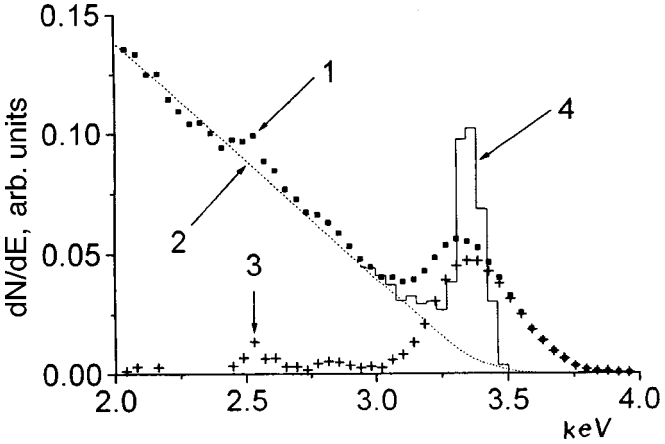

FIG. 2. High-energy part of the deuteron spectrum reflected by a multilayer B_4C/Mo target bombarded by 12 keV D_3^+ ions (60° glancing angle, 60° scattering angle): *1* — experiment, *2* — computer simulation for a B_4C target, *3* — difference between spectra *1* and *2*, and *4* — computer simulation of a B_4C target with a single 0.6 nm thick Mo layer at a depth of 4.3 nm.

and also the width of the peak formed by these particles are small compared with the initial beam energy, in principle the inhomogeneity over the thickness of the first B_4C layer can be analyzed using the results of Ref. 3, in which Koborov *et al*. determined the width of the particle energy distribution during propagation through a thin free foil as a function of various factors, including fluctuations in its thickness.

To conclude, we have shown that low-energy hydrogen ions can be successfully used for a layer-by-layer analysis of multilayer structures of ultrathin films. Estimates of the broadening of the Mo layer by ion mixing under ion bombardment, made using the same SCATTER program and also confirmed experimentally using high radiation doses, show that the $10^{14}\,cm^{-2}$ dose needed for the measurements barely influences the parameters of the Mo layer. The simplicity of the method together with the inexpensive equipment used suggest that this method may be successfully used directly in production systems for *in situ* monitoring of processes.

This work was partially supported by the Russian Fund for Fundamental Research (Project No. 96-02-19283).

[1] C. P. Woodruffe and T. A. Delchar, *Modern Techniques of Surface Science* (Cambridge University Press, Cambridge, 1986; Mir, Moscow, 1989, 564 pp.).
[2] A. Feurstein, H. Grahmann, S. Kabitzer, and H. Oestzman, *Ion Beam Surface Layer Analysis*, edited by O. Meyer, G. Linker, and F. Kappeler (Plenum Press, New York, 1975), p. 471.
[3] N. N. Koborov, A. I. Kuzovlev, V. A. Kurnaev, V. S. Remizovich, and N. N. Trifonov, Nucl. Instrum. Methods Phys. Res. B **129**, 5 (1977).
[4] S. S. Andreev, A. D. Akhsakhalyan, M. N. Drozdov, N. I. Polushkin, and N. N. Salashenko, Thin Solid Films **263**, 169 (1995).
[5] M. N. Drozdov, S. S. Andreev, D. V. Masterov, N. N. Salashchenko, and E. A. Shamov, Poverkhnost' **11**, 57 (1997).
[6] W. Eckstein, *Computer Simulation of Ion-Solid Interactions* (Springer-Verlag, New York, 1991; Mir, Moscow, 1995, 321 pp.).
[7] V. A. Kurnaev, E. S. Mashkova, and V. A. Molchanov, *Scattering of Light Ions by the Surface of Solids* [in Russian], Énergoatomizdat, Moscow (1985), 192 pp.

Translated by R. M. Durham

Nature of the ''ring effect'' in intense field emission

A. V. Batrakov and D. I. Proskurovskiĭ

Institute of High-Current Electronics, Siberian Branch of the Russian Academy of Sciences, Tomsk
(Submitted December 14, 1998)
Pis'ma Zh. Tekh. Fiz. **25**, 57–63 (June 12, 1999)

The electron trajectories corresponding to the angular distribution of the emission current are simulated, allowing for self-heating of the cathode and the influence of space charge on the emission. It is shown that the nature of the rings is related to the emission from peripheral regions of the tip (conical section) and to compression of the current from these regions.
 [S1063-7850(99)01006-X]

Studies of pulsed field emission in a field-emission microscope[1–5] have conclusively established that as the current densities approach critical levels, the emission pattern undergoes a characteristic change, with the appearance of a bright ring surrounding the normal emission image. The authors of Refs. 1–5 showed that this bright ring may be caused by thermionic emission from the peripheral region of the cathode tip when it is heated by its own emission current. The delay before the current appears in the ring relative to the field emission current from the tip apex was ascribed by these authors[2–5] to the inertia in the heating of the conical part of the tip. However, these authors[2–5] cast some doubt on the accuracy of this explanation of the ring effect because the current in the ring increases by two or three orders of magnitude during the pulse, whereas the temperature correction to the field emission current within the range of validity of

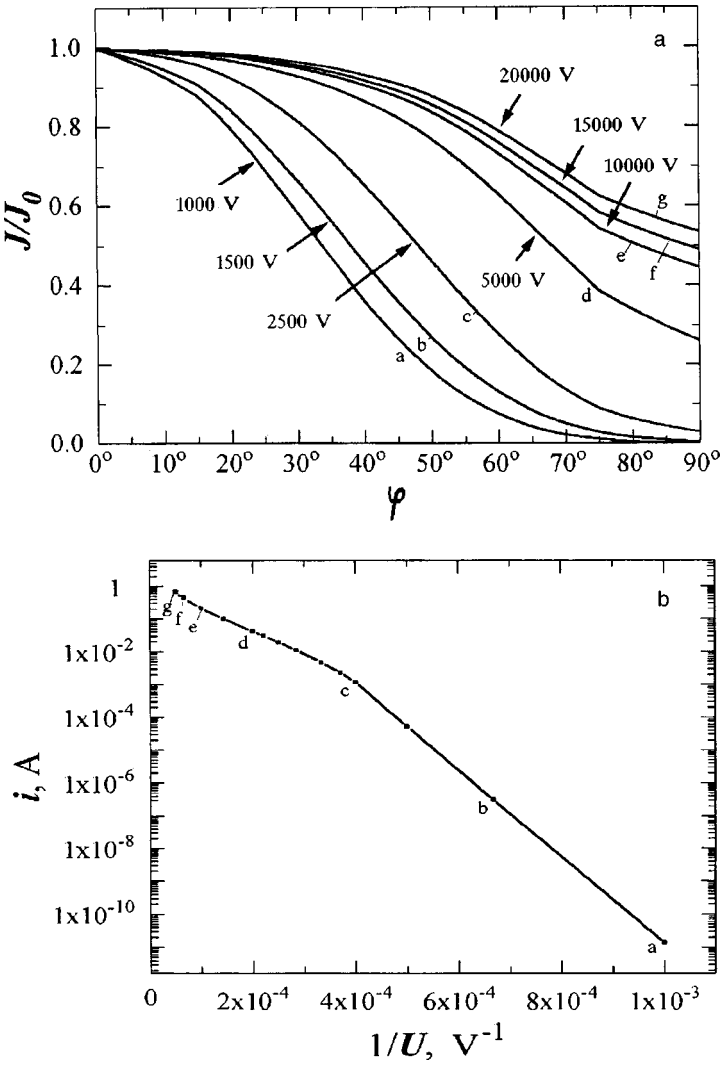

FIG. 1. Angular distributions of the current density at the cathode (a) and calculated current–voltage characteristic. The letters on the current–voltage characteristic (b) correspond to the current density distributions (a).

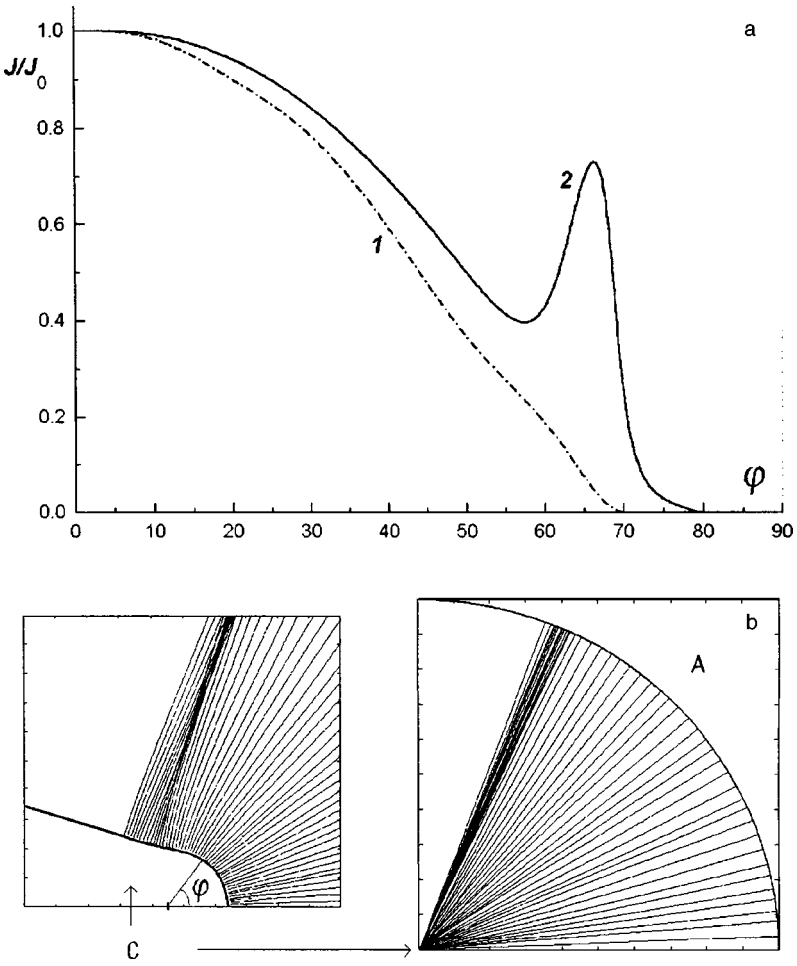

FIG. 2. Current density distribution at the surface of the anode (a) for distributions of the emission current density given by curve *c* (*1*) and curve *d* (*2*) in Fig. 1 and electron trajectories calculated for the second case (b). A — anode and C — cathode.

the Fowler–Nordheim equation[6] is only a few tens of percent. Another problem, in the view of these authors,[2–5] is that careful scrutiny of the emission images can reveal several (two or three or more) rings, which may indicate that they are of diffraction origin.

The observation of the ring effect for voltages pulses of tens of nanoseconds[7] resulted in a different explanation for these rings.[8,9] Zhukov and Egorov[8] and Zhukov *et al.*[9] postulate that as the apex of the tip is heated rapidly by the field emission current, a very thin layer of ''quasiliquid'' metal forms on its surface. Vertically polarized waves propagate along the interface between this layer and the underlying material. At the periphery of the tip apex, where the liquid layer becomes thinner, the amplitude of the waves increases, causing rings to appear on the emission image. This model seems rather unconvincing because the presence of liquid metal in a strong electric field ($\sim 10^8$ V/cm) would inevitably cause a conical protrusion to develop and subsequently explode[10] over times $< 10^{-9}$ s.

In order to understand the nature of the ring effect, we made a numerical simulation of the behavior of the electron beam in a field-emission microscope using the SuperSAM program.[11] We first need to know the exact angular distribution of the field emission current density over the cathode surface. We note that the ring effect begins to appear when the field emission current density is limited by the space charge of the emitted electrons.[1–5] Under these conditions, the tip region of the cathode involved in the field emission becomes substantially broader.[1] In addition, the electric field at the surface of the field emitter is considerably weaker than the field calculated by solving the electrostatic problem because of the screening influence of the space charge,[12] which must also be taken into account in the simulation.

The model of the field-emission microscope included a pointed cathode having a tip radius $r_c = 0.2\,\mu$m, a conical section with half-angle $\Theta = 12°$, and a hemispherical anode of radius 2 cm. For each angular segment of the cathode we calculated the geometric field E_g, and then using expression (3) from Ref. 12, we calculated the real field E_c for this section of the cathode. These values of E_c were used to calculate the emissivity of the cathode segments using the Fowler–Nordheim equation. Figure 1a shows the angular distributions of the current density for $\phi = 4.5$ eV. The current–voltage characteristic of the field-emission microscope was also calculated by integrating the distributed current density over the emitter surface (Fig.1b). Curve *c* in Fig. 1a corresponds to the time when the space charge begins to influence the current–voltage profile (point *c* in Fig. 1b). As the accelerating voltage increases, the fraction of the current extracted from the periphery of the field emitter tip increases substantially. The current–voltage characteristic deviates increasingly from the Fowler–Nordheim characteristic toward lower currents. The increase in current with increasing voltage is caused by an increase in the current density and by the

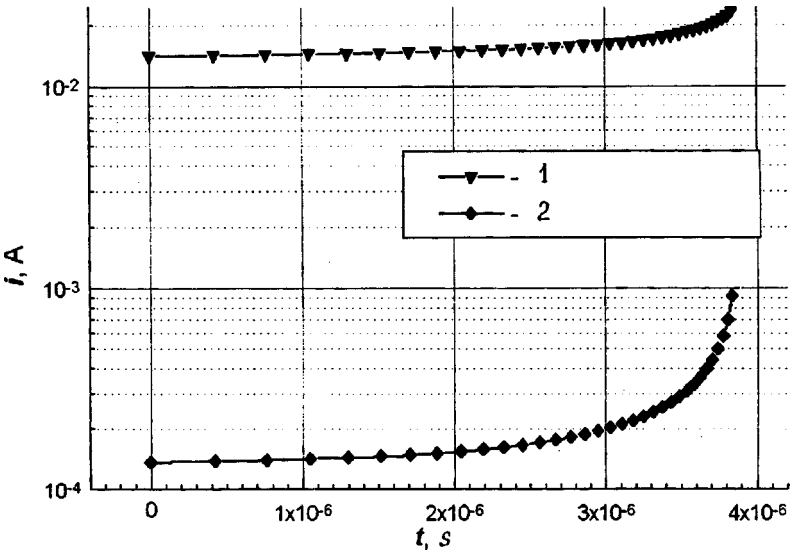

FIG. 3. Time dependence of the total current (*1*) and the current from the periphery (*2*).

involvement of the periphery in the emission process.

Hence, two key factors emerge: the field emission current is only limited by the hemispherical part of the tip (curves *a–c* in Fig. 1a) and an appreciable fraction of the emission takes place at the periphery of the tip apex (curves *d–g*). Examples of the results of simulating the electron beam in a field-emission microscope for these scenarios are given in Fig. 2.

After analyzing these results, we can make the following observations. In the absence of any appreciable emission from the conical part of the tip, we observe no bunching of the electron trajectories at the periphery of the electron image on the anode (Fig. 2a, curve *1*). In cases where the current density is limited by the electron space charge when appreciable emission is observed from the side surface of the tip, the trajectories of electrons emitted by the conical part of the tip become bunched at the periphery of the emission image (Fig. 2b). This is manifested as a high peak on the angular distribution of the current density at the anode of the field-emission microscope (Fig. 2a, curve *2*). Thus, the emission from the periphery can in fact explain the existence of a ring on the emission image.

It is also important to specify the role of the thermal correction to the field emission current in the appearance of the ring effect. For this purpose we made a numerical simulation of the heating of the tip by the field emission current for the cathode geometry described above in order to determine the influence of the heating on the angular distribution of the current density at the cathode and the anode under conditions close to the experiments.[1–4] The value of E_g at the tip apex was taken to be 7×10^7 V/cm. The real values of the electric field strength and the emission current density were calculated allowing for the space charge of the emitted electrons. The heat source in the heat conduction equation was assumed to be merely Joule heating. The current density in the emitter body was calculated by integrating the emission current density over the emitter surface. The Fowler–Nordheim equation for the extended thermionic field emission range[6] was used to calculate the field emission current density. Since this equation can be applied at relatively low temperatures, the condition for the end of the voltage pulse was taken as the time when the emitter tip reaches 2000 K. As a result of this simulation, we established that the transition from field emission to thermionic field emission leads to a sharp rise in the fraction of the current from the periphery in the total current (Fig. 3). Since almost the entire current from the conical part of the tip is compressed into a ring, the current density in the ring at the anode also increases considerably faster than the emission current density from the tip and the entire current from the tip. The current in the ring increases as a result of an increase in the emission current density and as a result of an increase in the emission area. The saturation of the current in the ring observed in Refs. 3–5 can reasonably be attributed to the emitter going over to a quasisteady-state thermal regime. However, the upper temperature constraint on using the Fowler–Nordheim equation prevented us from simulating the heating of the tip for higher temperatures.

To sum up, this analysis has clearly indicated that the appearance of a ring on the field emission image is caused by the peripheral part of the tip apex taking part in the emission process. More accurate modeling may well be required to explain the appearance of several rings.

The authors would like to than I. V. Pegel' for assistance with the numerical simulation.

This work was partially supported by the Russian Fund for Fundamental Research (Project No. 97-02-17208) and by the Siberian Branch of the Russian Academy of Sciences (Grant from Youth Projects Competitive Examination, 1997).

[1] W. P. Dyke, J. K. Trolan, E. E. Martin, and J. P. Barbour, Phys. Rev. **91**, 1043 (1953).
[2] I. L. Sokol'skaya and G. N. Furseĭ, Radiotekh. Elektron. **7**, 1474 (1962).
[3] I. L. Sokol'skaya and G. N. Furseĭ, Radiotekh. Elektron. **7**, 1484 (1962).
[4] G. N. Furseĭ and I. D. Tolkacheva, Radiotekh. Elektron. **8**, 1210 (1963).
[5] G. N. Furseĭ, Zh. Tekh. Fiz **34**, 1312 (1964) [Sov. Phys. Tech. Phys. **9**, 1013 (1965)].
[6] H. Craig Miller, J. Vac. Sci. Technol. **17**, 691 (1980).

[7] V. M. Zhukov and S. A. Polezhaev, Radiotekh. Elektron. **33**, 2360 (1988).
[8] V. M. Zhukov and N. V. Egorov, Zh. Tekh. Fiz **61**(3), 170 (1991) [Sov. Phys. Tech. Phys. **36**, 353 (1991)].
[9] V. M. Zhukov, N. V. Egorov, and A. P. Prudnikov, Poverkhnost'. No. 6, 33 (1993).
[10] A. V. Batrakov, S. A. Popov, and D. I. Proskurovskiĭ, JETP Lett. **67**, 299 (1998)].
[11] D. G. Myakishev, M. A. Tiunov, and V. P. Yakovlev, Int. J. Mod. Phys. A (Proc. Suppl.) 2B **2**, 915 (1993).
[12] A. V. Batrakov, I. V. Pegel, and D. I. Proskurovsky, in *Proceedings of the of 18th International Symposium on Discharges and Electrical Insulation in Vacuum*, Eindhoven, The Netherlands, 1988, pp. 44–47.

Translated by R. M. Durham

Membrane oscillations in the channel of a steady-state plasma thruster

A. I. Bugrova, A. S. Lipatov, A. I. Morozov, and V. K. Kharchevnikov

Moscow State Institute of Radio Engineering, Electronics, and Automation
(Submitted February 11, 1999)
Pis'ma Zh. Tekh. Fiz. **25**, 64–68 (June 12, 1999)

Extremely strong low-frequency oscillations (~ 35 kHz) predicted earlier were observed experimentally in the channel of a steady-state plasma thruster. These oscillations are mainly caused by fluctuations of the electron temperature and affect the ion beam divergence.
 [S1063-7850(99)01106-4]

Low-frequency ($f \leqslant 1$ MHz) oscillations in the channel of a steady-state plasma thruster possess axial symmetry.[1,2] Thus, in the presence of oscillations the equipotentials (but not the magnetic drift surfaces) can either move along the channel (parallel to the z axis) or can change their curvature along the radius r. Oscillations of the first type, i.e., longitudinal oscillations, are usually considered. In 1995 Morozov drew attention to the strong influence of the second type of oscillations and called these ''membrane'' oscillations. These membrane oscillations strongly influence the divergence of the outgoing plasma jet and the erosion of the output section of the channel insulators.[3] They are fundamentally attributable to fluctuations of the electron temperature and the presence of a transverse flux density gradient. This statement follows from the formula for the electric potential[1]

$$\Phi(\bar{x},t)=\Phi^*(\psi)-\frac{1}{e}\int\frac{dP_e}{n}. \tag{1}$$

Here $\psi(r,z)$ is the magnetic flux function, $P_e = P_e(n,\psi)$, and the remaining notation is conventional. For clarity we write Eq. (1) for a Maxwellian electron distribution:

$$\Phi(\bar{x},t)=\Phi^*(\psi)-\frac{kT_e(t,\psi)}{e}\ln\frac{n(\bar{x},t)}{n_0}. \tag{2}$$

Although the change in the curvature of the equipotentials can be attributed to a density perturbation, experiments carried out to measure the ion current and electron temperature fluctuations[4] show that the T_e fluctuations play a decisive role.

Figure 1 shows equipotentials for three values of T_e: optimum T_{e0} (Fig. 1a), maximum $T_{e\max}$ (Fig. 1b), and minimum $T_{e\min}$ (Fig. 1c). For a diverging flux (Fig. 1b) a crossover zone forms on the axis of the system, characterized by a complex superposition of fluxes which depend strongly on the individual characteristics of the plasma thruster and its operating regime.

Figure 2 shows distributions of the flux density leaving the plasma thruster for $r \geqslant r_1$, where r_1 is the radius of the internal insulator, corresponding to Figs. 1a and 1b.

If membrane oscillations appear in the system, the distribution of the flux density will vary with time as shown in Fig. 2. Then, if we take two pairs of probes p_1, p_2 and p_3, p_4 whose positions are indicated in Fig. 2, it is predicted that in the presence of membrane oscillations the ion signals at probes p_1 and p_2 will be in phase and those at probes p_3 and p_4 will be in antiphase. The signals should also be accompanied by fluctuations of the electron temperature in the channel of the plasma thruster.

Experiments carried out using the ATON plasma thruster[5] with $\dot{m}=2$ mg/s and $U_p=250$ V using probes completely confirmed these predictions. The experiment was carried out using two planar probes with a collecting surface area $S=60\ \text{mm}^2$ separated by a fixed distance $d=4$ cm. The probes were moved parallel (along the z axis) and at right angles (along the r axis) to the plasma flux by means of a coordinate device. A negative potential relative to ground $\varphi=-21$ V was applied to the probes so that the ion component of the probe current could be isolated and we obtained an oscilloscope trace of the J_1 oscillations on the screen of a storage oscilloscope. The frequency of the low-frequency oscillations was ~ 35 kHz. The experiment showed that as the probes move along r, the signals from the probes are either in phase or in antiphase (Fig. 3a). For larger z, i.e., the fur-

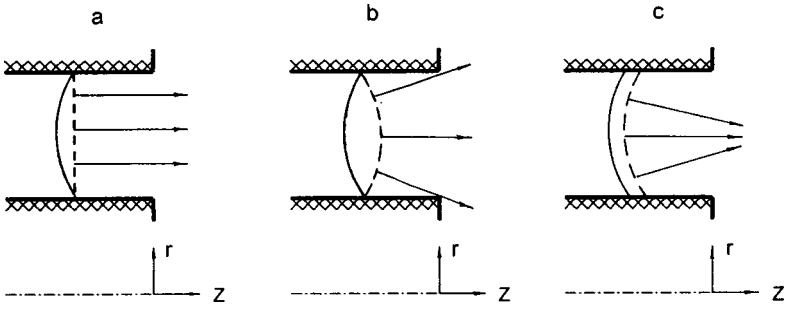

FIG. 1. Difference between the equipotentials and magnetic field lines in the channel of a steady-state plasma thruster at various electron temperatures: a — $T_e \sim T_{e0} \sim \varepsilon^*/e$ ($\sigma=1$), where ε^* is the electron energy for which the coefficient of secondary emission of the insulator is 1; b — $T_e \sim T_{e\max} > \varepsilon^*/e$ ($\sigma=1$), and c — $T_e \sim T_{e\min} < \varepsilon^*/e$ ($\sigma=1$). The solid curve gives the magnetic field lines and the dashed curves give the equipotentials.

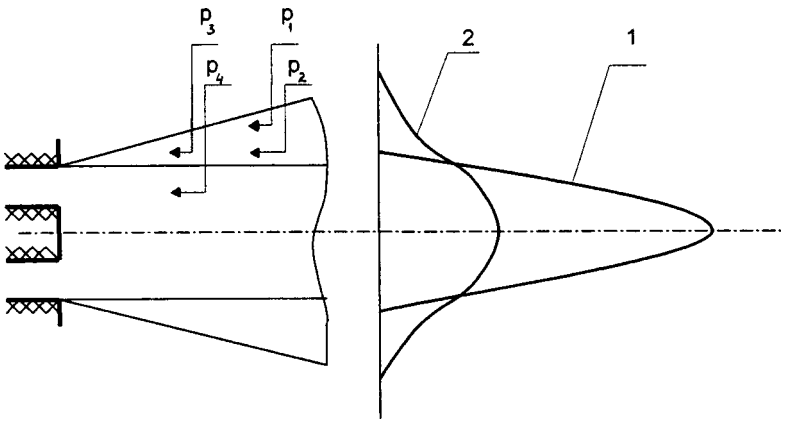

FIG. 2. Distribution of the ion flux density and position of the probes relative to the edge of the thruster: p_1, p_2 — first pair of probes, p_3, p_4 — second pair of probes. *1* — distribution of ion flux density for time t_1, *2* — distribution of ion flux density for time t_2.

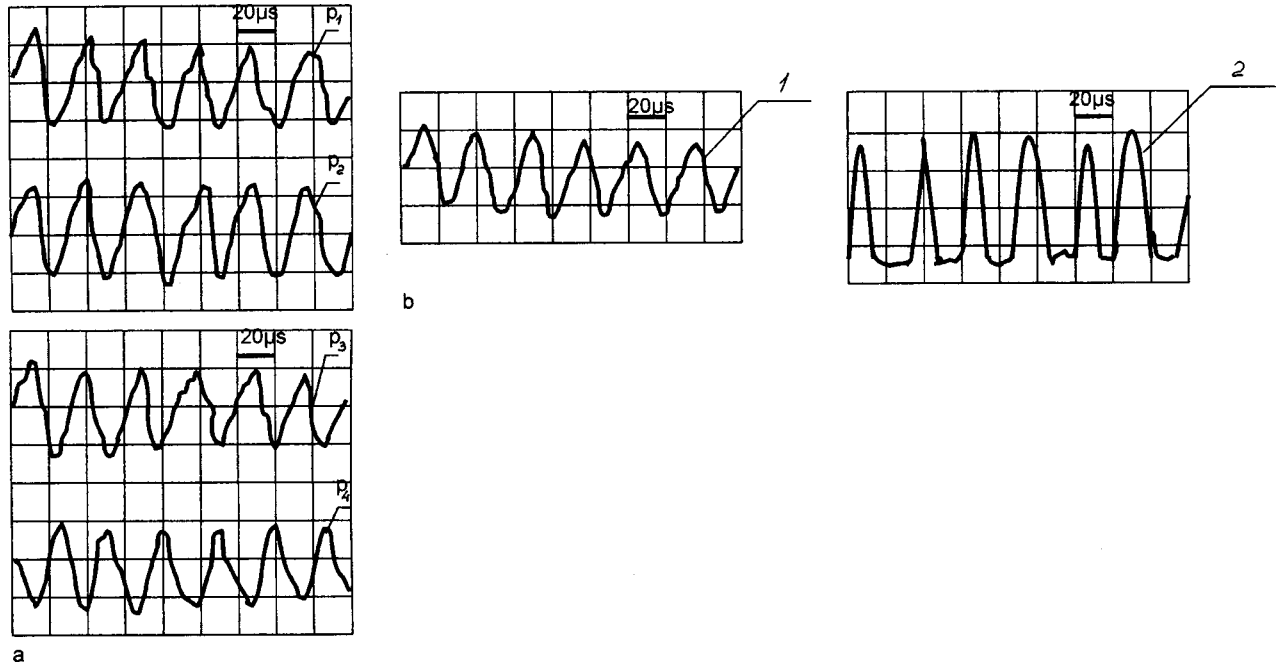

FIG. 3. a — Fluctuations of the ion current at two pairs of probes p_1, p_2 and p_3, p_4; b — fluctuations of the ion current (*1*) and electron temperature (*2*).

ther we move from the edge of the thruster, the further are these positions from the symmetry axis of the plasma jet. Thus, we confirmed that beyond the edge of the thruster there are regions in each of which the oscillations are phase-matched, and these are separated by a zone where the oscillations are in antiphase.

Figure 3b shows oscilloscope traces of the ion current fluctuations at a wall probe mounted in the thruster channel and fluctuations of the electron temperature obtained by analyzing the probe current–voltage characteristics. It can be seen from these traces that the fluctuations of the ion current at the wall probes are accompanied by fluctuations of the electron temperature.

Thus, we have confirmed experimentally that membrane oscillations exist in a steady-state plasma thruster.

This work was supported by INTAS Grant No. 96 2276.

[1] A. I. Morozov, *Physical Principles of Ion-Plasma Jet Space Engines* [in Russian], Atomizdat, Moscow (1978).
[2] A. I. Morozov, in *Proceedings of the 24th International Electric Propulsion Conference*, Moscow, 1995.
[3] B. A. Arkhipov, R. Yu. Gnizdor, N. A. Maslennikov, and A. I. Morozov, Fiz. Plazmy **18**, 1241 (1992) [Sov. J. Plasma Phys. **18**, 641 (1992)].
[4] A. I. Bugrova and A. I. Morozov, in *Proceedings of the 23rd International Conference on Phenomena in Ionized Gases*, Toulouse, France, 1997.
[5] A. I. Morozov, Fiz. Plazmy **23**, 635 (1997) [Plasma Phys. Rep. **23**, 587 (1997)].

Translated by R. M. Durham

Micromechanism for anomalous creep of $MoSi_2$ polycrystals

I. A. Ovid'ko

Institute of Problems of Mechanical Engineering, Russian Academy of Sciences, St. Petersburg
(Submitted January 27, 1999)
Pis'ma Zh. Tekh. Fiz. **25**, 69–73 (June 12, 1999)

A theoretical model is proposed for an anomalous creep effect in $MoSi_2$ polycrystals (characterized by an anomalous dependence of the plastic strain rate on the grain size). In this model the micromechanism for anomalous creep is represented as the diffusion-controlled climb of grain-boundary dislocations in grain-boundary planes. © *1999 American Institute of Physics.* [S1063-7850(99)01206-9]

Plastic deformation in crystals occurs through the movement of defects whose aggregate characteristics are responsible for the dependence of the strain macrocharacteristics on the structural parameters of the crystal (Refs. 1 and 2). For instance, the dependence $\dot{\varepsilon} \propto d^{-p}$ of the plastic strain rate on the grain size d in polycrystals undergoing high-temperature creep is determined by the behavior characteristics of ensembles of defects (strain carriers). The power is usually found to be $p=2$ (for Nabarro–Herring creep resulting from the intragranular migration of point defects) or $p=3$ (for Coble–Lifshitz creep resulting from the migration of point defects along grain boundaries).[2] An anomalous dependence $\dot{\varepsilon} \propto d^{-p}$, $p \geqslant 5$ was recently identified experimentally for $MoSi_2$ polycrystals[3–5] which cannot be explained in terms of existing physical models of creep. Here we propose a model which attributes the anomalous dependence $\dot{\varepsilon} \propto d^{-5}$ to a particular creep micromechanism, that is, dislocation climbing in grain boundaries.

In the proposed model, plastic deformation in an $MoSi_2$ polycrystal undergoing creep is resulting from the climbing of dislocations at grain boundaries, which is controlled by the diffusion of point defects (vacancies, interstitial atoms) in the grain boundaries (see Fig. 1). The fluxes of point defects formed under mechanical loading, which are intense at grain boundaries and especially at grain-boundary triple-junctions, play a particular role here.[1)] In fact, each dislocation, or strain carrier, migrates (climbs) in the grain-boundary plane as a result of fluxes of point defects moving inside the dislocation core from its edges (joined to triple junctions) toward the center and/or in the opposite direction (see Fig. 1).

In this situation the plastic strain rate is given by

$$\dot{\varepsilon} - = \rho b v, \tag{1}$$

where ρ is the density of ''active'' dislocations, b is the Burgers dislocation vector, and v is the dislocation climb rate. In this case, b does not depend on d but the density of active dislocations is

$$\rho \propto d^{-2}, \tag{2}$$

since these dislocations are localized in grain boundaries.

We shall now analyze the dependence of v on d. Since the dislocation climb is controlled by fluxes of point defects through the dislocation cores (see Fig. 1), a dislocation of length d migrates (climbs) over a distance equal to the crystal lattice parameter a when d/a point defects pass through its core. In this situation the dislocation climb rate is given by

$$v = \varphi a (a/d), \tag{3}$$

where φ is the number of point defects which have passed through the dislocation core per unit time. The value of φ is defined in terms of the flux J of point defects through the dislocation core (which has the cross section a^2) as follows:

$$\varphi = J a^2. \tag{4}$$

In turn the flux J depends on the spatial distribution of the point defect densities $C_i(x)$, where i is the type of point defect and x is the coordinate along the dislocation line. For simplicity we shall confine our analysis to the case where the main contribution to the dislocation climb is made by a flux of point defects of the same type (for instance, interstitial atoms), moving from the edges of the dislocation (having the coordinates $x=0$ and $x=d$) toward its center ($x=d/2$), where the spatial distribution $C(x)$ of the point defects is symmetric relative to the center point of the dislocation $x=d/2$. In this case, to a first approximation, the flux J depends on $C(x)$ as follows:

$$J = -D \operatorname{grad} C(x) \approx \alpha D \frac{C(d/2) - C(0)}{d/2}, \tag{5}$$

where D is the diffusion coefficient in the core of a dislocation situated in the grain boundary and $\alpha = \text{const}$.

The spatial distribution $C(x)$ is determined by elastic interaction between point defects and triple junctions as sources of internal stresses. More accurately (in the sense of the theory of interaction between point defects and sources of internal stresses),[7] in equilibrium $C(x)$ is given by

$$C(x) = C_0 \exp\{U(x)/kT\}, \tag{6}$$

where $C_0 = \text{const}$, k is the Boltzmann constant, T is the temperature, and $U(x)$ is the potential of elastic interaction between point defects and a triple junction. Disclinations which act as sources of long-range stresses[8] frequently form at grain-boundary triple junctions in polycrystals synthesized

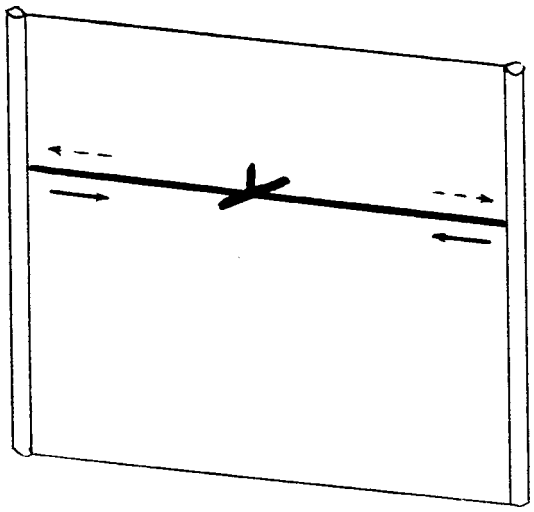

FIG. 1. Dislocation climb controlled by diffusion fluxes (solid and dashed arrows) in the plane of a grain boundary bounded by triple junctions (cylindrical regions).

from powders at high pressures such as $MoSi_2$ (Refs. 3–5). The interaction potential between wedge dislocations and dilatational point defects takes the form[9]

$$U(x) = -\beta \ln (x/a) \tag{7}$$

(β=const), which taking account of Eqs. (5) and (6) determines the following dependence of J on d:

$$J \propto d^{-2} \tag{8}$$

for polycrystals having disclinations at grain-boundary triple junctions. Equations (1)–(4) and (8) yield the following dependence

$$\dot{\varepsilon} \propto d^{-5}. \tag{9}$$

This dependence was observed in experiments to study creep in $MoSi_2$ polycrystals in a specific range of structural parameters and mechanical loading characteristics.

To sum up, a model of plastic deformation resulting from dislocation climb in grain boundaries of polycrystals with connecting disclinations efficiently describes the anomalous dependence ($\dot{\varepsilon} \propto d^{-5}$) of the plastic strain rate on the grain size in $MoSi_2$ crystals undergoing creep. However, in order to identify the micromechanism for creep in $MoSi_2$ polycrystals (and therefore check the proposed model), it is important to carry out new experiments to observe the evolution of the microstructure in deformable $MoSi_2$ polycrystals.

The author would like to than Dr. K. Sadananda for useful discussions which stimulated this work.

This work was supported by the Russian Fund for Fundamental Research (Grant No. 98-02-16075), the US Office of Naval Research, and the Volkswagen Foundation.

[1)] According to Rabukhin[6] the diffusion coefficients at grain-boundary triple junctions are substantially higher (frequently several orders of magnitude higher) than those in the grain boundaries themselves.

[1] B. I. Smirnov, *Dislocation Structure and Strengthening of Crystals*. L.: Nauka, 1981. 235 s.
[2] J.-P. Poirier, *Creep of Crystals* (Cambridge University Press, Cambridge, 1985; Mir, Moscow, 1988, 288 pp.)
[3] K. Sadananda, C. R. Feng, H. Jones, and J. Petrovic, Mater. Sci. Eng., A **227**, 155 (1992).
[4] K. Sadananda and C. R. Feng, Mater. Sci. Eng., A **170**, 199 (1993).
[5] K. Sadananda and C. R. Feng, Mater. Res. Soc. Symp. Proc. **322**, 157 (1994).
[6] V. B. Rabukhin, Poverkhnost' No. **6**, 143 (1986); No 7, 126 (1986).
[7] B. Ya. Lyubov, *Diffusion Processes in Inhomogeneous Solids* [in Russian], Nauka, Moscow (1981), 296 pp.
[8] V. G. Gryaznov and L. I. Trusov, Prog. Mater. Sci. **37**, 289 (1993).
[9] A. E. Romanov and G. G. Samsonidze, Pis'ma Zh. Tekh. Fiz **14**, 1339 (1988) [Sov. Tech. Phys. Lett. **14**, 585 (1988)].

Translated by R. M. Durham

Nutational nuclear quadrupole resonance in metal oxide compounds of copper

A. S. Azheganov, I. V. Zolotarev, and A. S. Kim

Perm State University
(Submitted May 28, 1998; resubmitted February 22, 1999)
Pis'ma Zh. Tekh. Fiz. **25**, 74–77 (June 12, 1999)

A pulsed nuclear quadrupole resonance method that can be used to study compounds with broad lines, especially metal oxide compounds of copper, is considered for the first time. © *1999 American Institute of Physics.* [S1063-7850(99)01306-3]

For spin 3/2 nuclei the nuclear quadrupole resonance (NQR) spectrum contains only one line, so that measurements of its resonant frequency cannot be used to determine the two quadrupole interaction parameters separately, i.e., the quadrupole interaction constant eQq_{zz} and the asymmetry parameter η of the electric field gradient. The parameter η is usually measured by applying an external magnetic field, i.e., the Zeeman effect in nuclear quadrupole resonance.[1,2] The external field splits the doubly degenerate quadrupole energy levels, giving a complex NQR spectrum from which the required parameters can be determined. However, the various Zeeman-effect techniques can only be applied for fairly narrow NQR lines. For metal oxide compounds, especially high-temperature superconductors, the lines of the NQR spectrum are fairly broad ($\sim 10^2$ – 10^3) kHz, which means that the Zeeman effect cannot be used.

The aim of the present study is to develop an optimum NQR method which can be applied to investigate compounds with broad lines, especially metal oxide compounds of copper.

Nuclear quadrupole resonance is usually recorded at the resonant frequency ω_Q of the excited transition. However, NQR can also be recorded at the nutation frequency of the nuclei, which for NQR is equal to the NQR frequency in a rotating coordinate system.[3] Measuring the nutation frequency ω_n can provide information on the parameter η of the electric field gradient. For nuclear spins $J=3/2$ the frequency ω_n is given by[4]

$$\omega_n = 2\pi\nu_n = \frac{\omega_1}{\rho}\left[(\rho^2-1)\cos^2\theta + \frac{1}{4}(2+\rho^2 + 2\eta\cos 2\varphi)\sin^2\theta\right]^{1/2}, \quad \rho = \sqrt{1+\frac{\eta^2}{3}}, \tag{1}$$

where η is the asymmetry parameter of the electric field gradient, $\omega_1=\gamma H_1$ (H_1 is the amplitude of the rf field), and θ and φ are the polar and azimuthal angles of the vector $\mathbf{H}_1$ in the system of principal axes X, Y, Z of the electric field gradient.

It can be seen from expression (1) that the frequency ω_n in a single crystal depends on η and also on the orientation of the axes of the electric field gradient relative to the direction of the rf field. In cases where quadrupole nuclei occupy several sites in the lattice, their nutational NQR frequencies can be distinguished even if the quadrupole parameters eQq_{zz} and η nuclei are the same, provided that the orientations of the electric-field-gradient axes at their sites are different.

When echo signals are excited by a two-pulse method, the echo amplitude depends on three independent time parameters (the duration of the first pulse t_1, the duration of the second pulse t_2, and the time interval between them τ), so that three methods of observing the modulation effect of the spin echo envelope can be used.

We shall examine one of these methods, where the durations of the first and second pulses are varied (where $t_2=2t_1$) for a selected interval τ. In this variant, the echo amplitude for a polycrystal is given by

$$E(t_1,\omega_1,\eta) = \int_0^{2\pi}\int_0^{\pi} \sin\theta(\omega_n \sin^3(\omega_n t_1))\,d\theta\,d\varphi. \tag{2}$$

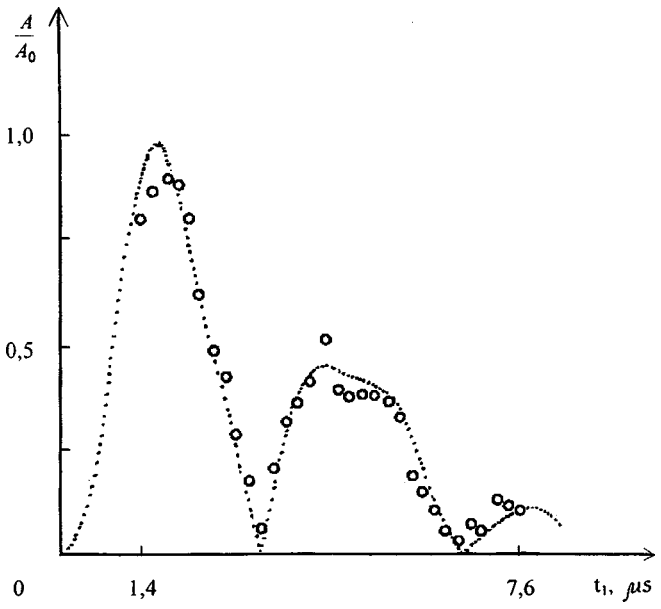

FIG. 1. Amplitude of the spin echo of ^{63}Cu nuclei in $Y_1Ba_2Cu_3O_{7-\delta}$ (Cu1 position) as a function of the pulse duration for an interpulse interval $\tau=22\ \mu$s.

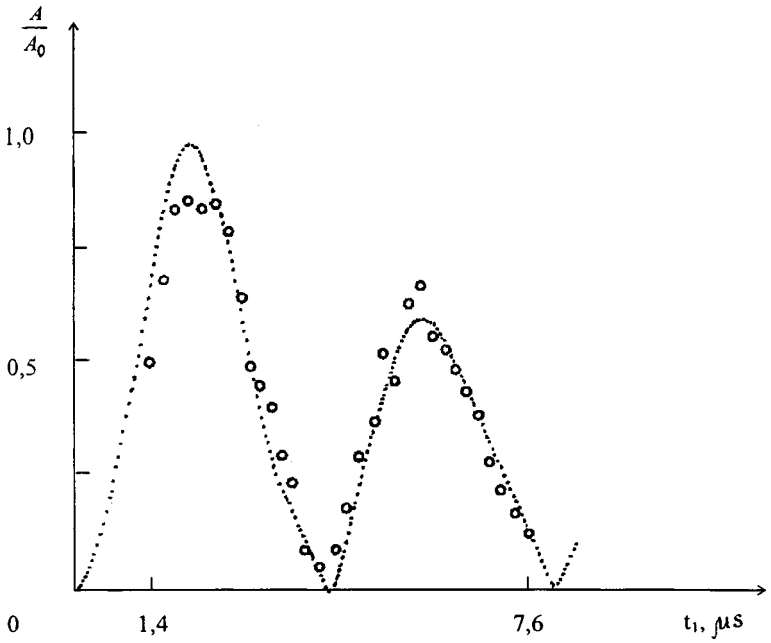

FIG. 2. Amplitude of the spin echo of ^{63}Cu nuclei in $Y_1Ba_2Cu_3O_{7-\delta}$ (Cu2 position) as a function of the pulse duration for an interpulse interval $\tau = 22\ \mu$s.

It can be seen from expression (2) that the amplitude of the spin echo is modulated at the frequency ω_n.

We used the high-temperature superconductor $Y_1Ba_2Cu_3O_{7-d}$ to carry out experiments with ^{63}Cu nuclei at frequencies of 31.13 MHz (Cu2) and 22.24 MHz (Cu1). The duration of the first pulse t_1 was varied between 1.4 and 7.6 μs in 0.2 μs steps (the duration of the second pulse was $t_2 = 2t_1$) and the interpulse interval was $\tau = 22\ \mu$s.

Figures 1 and 2 show the observed modulation of the ^{63}Cu echo amplitude in this yttrium ceramic. The NQR line of ^{63}Cu at 31.13 MHz has an appreciable width of $\sim$0.2 MHz, which becomes comparable with the width of the radio pulse spectrum and then exceeds it as the pulse duration increases (in the experiment we introduced a correction to allow for the narrowing of the radio pulse spectrum). These figures also show the calculated dependence of the echo amplitude on the radio pulse duration for $\eta = 0.3$ (Cu2) and $\eta = 0.8$ (Cu1). A comparison of the patterns of the modulation effect reveals that in position Cu1 (Fig. 1) the asymmetry parameter of the electric field gradient is close to 1, whereas in position Cu2 (Fig. 2) the asymmetry parameter is considerably smaller, $\eta = 0.3$.

To conclude, good qualitative agreement is obtained between the theory and the experiment for nutational NQR, which can be used to estimate the asymmetry of the electric field gradient for NQR spectra with broad lines.

[1] C. Dean, Phys. Rev. **96**, 1053 (1954).
[2] M. H. Cohen, Phys. Rev. **96**, 1278 (1954).
[3] N. E. Aĭnbinder and G. B. Furman, Zh. Éksp. Teor. Fiz. **85**, 988 (1983) [Sov. Phys. JETP **58**, 575 (1983)].
[4] N. E. Aĭnbinder and A. N. Osipenko, Izv. Vyssh. Uchebn. Zaved. Radiofiz. **26**, 1617 (1983).

Translated by R. M. Durham

Limitation of the field emission current density by the space charge of the emitted electrons

A. V. Batrakov, I. V. Pegel', and D. I. Proskurovskiĭ

Institute of High-Current Electronics, Siberian Branch of the Russian Academy of Sciences, Tomsk
(Submitted December 14, 1998)
Pis'ma Zh. Tekh. Fiz. **25**, 78–82 (June 12, 1999)

Rigorous and exact calculations are used to show that in earlier analytic studies of this problem by Barbour *et al.* [Phys. Rev. **92**, 45 (1953)] and Aĭzenberg [Zh. Tekh. Fiz **11**, 2079 (1954)], the influence of the electron space charge was not taken into account very accurately. It is shown that the real field of action is much weaker than that calculated geometrically.
 [S1063-7850(99)01406-8]

It has now been established experimentally beyond any doubt[1–3] that at field emission current densities $j \gtrsim 5\times10^6$ A/cm^2 the current is limited by the space charge of the emitted electrons. One manifestation of this effect is that the current–voltage characteristics calculated using the coordinates of the Fowler–Nordheim equation depart from a straight line toward lower currents. Quite clearly, the space charge primarily influences the electric field intensity at the cathode, reducing it. The greater the geometric electric field E_g (the field determined by solving the electrostatic problem for $j=0$), the higher the density of the field emission current, the stronger the influence of the space charge, and consequently, the greater the screening of the emitting surface, and the larger the difference between the real electric field at the cathode E_c and the geometric field E_g.

The first attempt to analyze this problem analytically was made by Stern *et al.*[4] for a planar vacuum diode with infinitely extended electrodes. This problem was then analyzed in greater detail by Dyke's group.[5] The field emission diode was replaced by an equivalent planar diode having an effective gap $d \simeq r_c$, where r_c is the radius of the field emitter tip. Solving, as in Ref. 4, the Poisson equation for this planar diode and using the Fowler–Nordheim equation for the current density [$j = AE_c^2 \exp(-B/E_c)$], these authors[5] derived an expression for the real electric field at the cathode:

$$E_c = \frac{U_a}{d} - \frac{4}{3\varepsilon_0}\sqrt{\frac{m}{2e}}\,\frac{U_a^{3/2}}{d}A\exp\left(\frac{-B}{E_c}\right) + 3\frac{m}{2\varepsilon_0^2 e}A^2E_c^2 d\exp\left(\frac{-2B}{E_c}\right), \quad (1)$$

where U_a is the anode potential, e and m are the electron charge and mass, respectively, and ε_0 is the dielectric constant. Since for this diode geometry we have $E_g = U_a/d$, expression (1) relates the real field at the cathode E_c to the geometric field E_g.

Quite clearly, a more accurate approach to analyzing the role of space charge in a field emission diode should involve determining the dependence of E_c on E_g by solving the Poisson equation for a spherical vacuum diode. This problem was first analyzed analytically by Aĭzenberg[6] who obtained the following approximate expression:

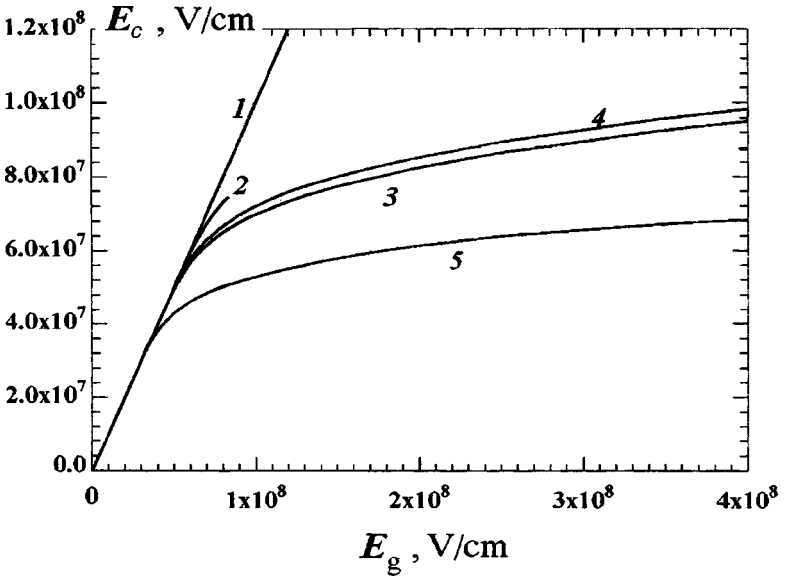

FIG. 1. Real field at the cathode versus geometric field: *1* — geometric field, *2* — from expression (1) for $\phi = 4.5$ eV, *3* — from expression (3) for $\phi = 4.5$ eV, *4* and *5* — numerical solutions of the Poisson equation for $\phi = 4.5$ eV and $\phi = 3.5$ eV, respectively.

TABLE I.

r_c, μm	E_g, V/cm	E_c, V/cm	$j(E_c)$, A/cm^2	j (Ref. 8), A/cm^2	j (Ref. 9), A/cm^2
0.2	5.5×10^8	1.03×10^8	8.7×10^8	between 6×10^8	between 4.5×10^8
0.15	7.3×10^8	1.11×10^8	1.5×10^9	and	and
0.1	1.1×10^9	1.25×10^8	3.6×10^9	2×10^9	6×10^8

$$E_c=\frac{U_a}{r_c}-\frac{i}{4\pi\varepsilon_0 r_c}\sqrt{\frac{m}{2eU_a}}\ln\frac{4r_a}{r_c}, \tag{2}$$

where i is the cathode current and r_a is the anode radius. If the current i is given by the Fowler–Nordheim equation, expression (2) has the form

$$E_c=\frac{U_a}{r_c}-\frac{r_c}{\varepsilon_0}\sqrt{\frac{m}{2eU_a}}\ln\frac{4r_a}{r_c}AE_c^2\exp\left(\frac{-B}{E_c}\right). \tag{3}$$

This expression also relates the real field at the cathode E_c to the geometric field E_g since for a spherical diode we have $E_g=U_a/r_c$.

Equations (1) and (3) were solved by an iterative method (see Fig. 1, curves *2* and *3*).

In order to obtain an accurate determination of the electric field E_c at the cathode under conditions where the field emission current is limited by space charge, we obtained a numerical solution of a self-consistent, nonsteady-state problem for an electron beam in a spherical diode using a macroparticle method.[7] In the model used, the emission current from the cathode was defined by the Fowler–Nordheim equation and the electric field at the cathode E_c was determined with allowance for the space charge of the emitted electrons by solving the Poisson equation

$$\frac{d^2U}{dr^2}+\frac{2}{r}\frac{dU}{dr}=-4\pi\rho(r) \tag{4}$$

with the boundary conditions for the potential

$$U(r_c)=0, \quad U(r_a)=U_a. \tag{5}$$

In order to compare these results with the results of the calculations using Eqs. (1) and (3), we used steady-state values of the current and the electric field in the diode. Our exact results $E_c(E_g)$ for two values of the work function ϕ are given by curves *4* and *5* in Fig. 1.

From an analysis of these curves we note that the behavior of $E_c(E_g)$ indicates that the cathode is strongly screened by the space charge of the emitted electrons for $E_g>5\times10^7$ V/cm. As the field E_g increases, the degree of screening increases as a result of the nonlinear dependence of the field emission current density on the field at the cathode. It can also be seen from Fig. 1 that expression (3) describes the behavior of the real field at the cathode of a spherical diode under intensive field emission more accurately than expression (1) and may be used to analyze the processes accompanying intensive field emission. Comparing curves *4* and *5*, we note that for a lower work function the screening of the electric field at the cathode is stronger because of the higher current density. Nevertheless, for the same geometric field E_g a lower work function ϕ corresponds to a higher field emission current density.

It is interesting to compare our calculated field emission current densities with the limiting current densities determined experimentally using short pulses. A comparison was made with data from Refs. 8 and 9 (tungsten cathodes, $r_c=0.1$–$0.2\,\mu$m, $r_a\simeq0.5$ cm, $U_a=15$ kV, and pulse duration 5 ns). The values of E_g were calculated numerically for a real vacuum-diode geometry using the SuperSAM program.[10] The results are summarized in Table I. It is easy to see that the calculated and experimental current densities are in good agreement. However, attention should be directed once again to the appreciable difference (a factor between 5 and 10) between the real field at the cathode and the geometric one.

This work was supported by the Russian Fund for Fundamental Research (Project No. 97-02-17208) and by the Siberian Branch of the Russian Academy of Sciences (Grant from Youth Projects Competitive Examination, 1997).

[1] W. P. Dyke and W. W. Dolan, Phys. Rev. **89**, 799 (1953).
[2] M. I. Elinson, V. A. Gor'kov, A. A. Yasnopol'skaya, and G. A. Kudintseva, Radiotekh. Elektron. No. 8, 1318 (1960).
[3] G. N. Furseĭ and I. D. Tolkacheva, Radiotekh. Elektron. No. 7, 1210 (1963).
[4] T. E. Stern, B. S. Gosling, and R. H. Fowler, Proc. R. Soc. London, Ser. A **124**, 699 (1929).
[5] J. P. Barbour, W. W. Dolan, J. K. Trolan, E. E. Martin, and W. P. Dyke, Phys. Rev. **92**(1), 45 (1953).
[6] N. B. Aĭzenberg, Zh. Tekh. Fiz. **11**, 2079 (1954).
[7] C. K. Birdsall and A. B. Langdon, *Plasma Physics via Computer Simulation* (McGraw-Hill, New York, 1985; Énergoatomizdat, Moscow, 1989, 455 pp.)
[8] G. K. Kartsev, G. A. Mesyats, D. I. Proskurovskiĭ, V. P. Rotshteĭn, and G. N. Furseĭ, Dokl. Akad. Nauk SSSR **192**, 309 (1970) [Sov. Phys. Dokl. **15**, 475 (1970)].
[9] V. M. Zhukov, M. S. Aksenov, and G. N. Furseĭ, Zh. Tekh. Fiz. **53**, 1588 (1983) [Sov. Phys. Tech. Phys. **28**, 976 (1983)].
[10] D. G. Myakishev, M. A. Tiunov, and V. P. Yakovlev, Int. J. Mod. Phys. A (Proc. Suppl.) **2**, 915 (1993).

Translated by R. M. Durham

Temperature dependence of transport losses in multicored high-temperature superconducting composites

I. A. Rudnev, A. E. Khodot, A. V. Eremin, and I. I. Akimov

Moscow State Engineering Physics Institute (Technical University), Moscow
(Submitted February 2, 1999)
Pis'ma Zh. Tekh. Fiz. **25**, 83–87 (June 12, 1999)

Measurements were made of the ac transport losses at temperatures $T \geqslant 77$ K in silver-sheathed $(Bi,Pb)_2Sr_2Ca_2Cu_3O_x$ composites with $N=19$, 61, and 127 filaments. It was observed that an increase in temperature causes an increase in the transport losses which depend on the amplitude of the working transport current. It is shown that the increase in the transport losses results from a reduction in the critical current of the composites. © *1999 American Institute of Physics.* [S1063-7850(99)01506-2]

At present, multicored high-temperature superconducting composites can be regarded as likely current-carrying elements for transformers and electric transmission lines with liquid nitrogen suggested as the working coolant. In consequence, almost all investigations of the electrical energy losses in the field of an alternating transport current (transport losses) have been carried out at $T=77$ K (Refs. 1–6). However, under the real operating conditions of electrotechnical systems using high-temperature superconducting elements, changes in the operating temperature may occur either for design reasons or because of emergency situations. It is therefore important to know how the transport losses change as the temperature increases and the reasons for the observed effects.

Here we report results of measurements of the transport losses in silver-sheathed multicored $(Bi,Pb)_2Sr_2Ca_2Cu_3O_x$ composite tapes at various temperatures. The investigations indicate that an increase in temperature causes an increase in the transport losses by lowering the critical current I_c of the composites.

Tapes of $(Bi,Pb)_2Sr_2Ca_2Cu_3O_x$/Ag composite containing $N=19$, 61, and 127 filaments were prepared by the ''powder in tube'' method described at length in the literature.[7] The typical dimensions of the measured tapes were $(0.1–0.2)\times(3–4)\times 30$ mm and the ratio of high-temperature superconductor to silver was $\sim 20:80$. In the experiments we measured the cophasal component of the first harmonic of the voltage at the sample as a function of the amplitude of the alternating transport current at different frequencies. The voltage at each frequency was determined using a selective amplifier. The inductive component of the voltage was compensated by using a transformer loop in the current circuit. The power of the total transport losses was determined as the product of the cophasal current and the voltage. The frequency of the alternating current was set by a sinusoidal signal generator and the current was then amplified using a low-frequency amplifier and a transformer. The potential outputs were loops between 1.5 times and twice the width of the tape, positioned in the plane of the tape.[5,8] The critical current was measured by the standard four-contact method using the 1 μV/cm criterion. For $B=0$ and $T=77$ K the value of I_c for different samples was between 12 and 19 A. The critical temperature was $T_c=110.5$ K. The experimental apparatus could vary the composite temperature between 77 and 95 K in 1.5 K steps and could sustain this temperature for the required time to within 0.5 K. At each temperature we measured the dc and ac current–voltage characteristics.

All the samples exhibited qualitatively the same results, and so for the sake of brevity we shall only give typical curves obtained for an $N=61$ composite for a transport current frequency $f=330$ Hz.

Figure 1 gives the specific power loss (normalized to the sample length) per cycle plotted as a function of the amplitude of the transport current $Q(I)$ at various temperatures T. It can be seen that if the current amplitude is fixed, a rise in the temperature is associated with an increase in losses. Moreover, the higher the working amplitude of the current, the greater is the relative increase in the losses.

What causes this increase in the transport losses? Calculations of the transport losses made for differently oriented composites show that the dependence of the losses on the normalized amplitude of the transport current $\beta=I/I_c$ is accurately described by the Norris equations (1) and (2) obtained for elliptic and rectangular cross sections, respectively:[9]

$$Q=\frac{\mu_0 I_c^2}{\pi}\left[(2-\beta)\frac{\beta}{2}+(1-\beta)\ln(1-\beta)\right], \tag{1}$$

$$Q=\frac{\mu_0 I_c^2}{\pi}[(1+\beta)\ln(1+\beta)+(1-\beta)\ln(1-\beta)-\beta^2)]. \tag{2}$$

In particular, it follows from expressions (1) and (2) that for fixed β the losses are determined only by the critical current and Q/I_c^2, i.e., the loss normalized to the square of the critical current is a general function of β for a given geometry. Figure 2 gives the dependence $Q/I_c^2(\beta)$ plotted using the measured values of Q and I_c for different temperatures. It

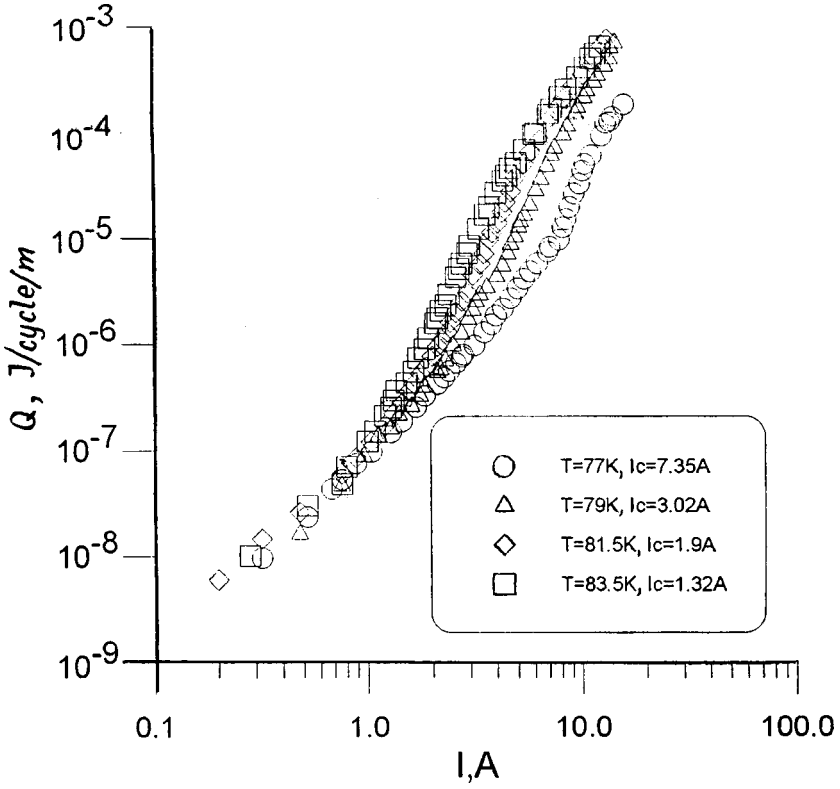

FIG. 1. Specific transport losses per cycle as a function of β.

can be seen that the curve $Q/I_c^2(\beta)$ is universal, which indicates that the changes in the losses with increasing temperature are caused by a drop in the critical current I_c of the composites.

To sum up, we have demonstrated experimentally that the influence of temperature on the transport losses amounts to a reduction in the critical current of the composites, similar to the influence of an external static magnetic field.[6] Note that by their nature, these losses are so-called ''losses in the saturated zone,'' which increase with decreasing I_c, unlike hysteresis losses.

This work was supported by the ANFKS Scientific Council, ''Superconductivity'' subprogram, Project No. 99011.

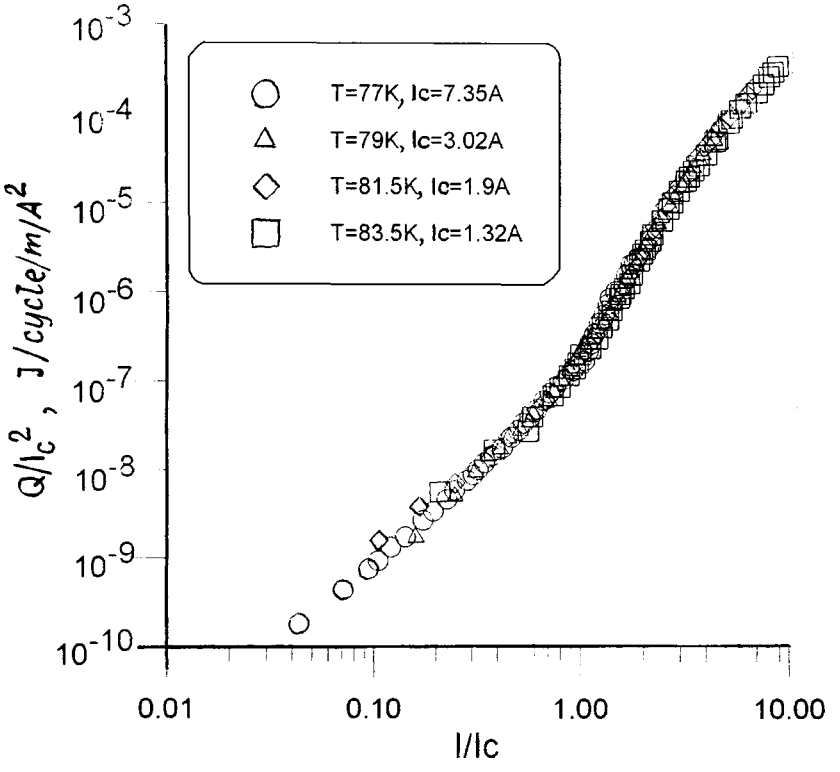

FIG. 2. Behavior of $Q/I_c^2(\beta)$ for an $N=61$ composite.

[1] S. A. Awan, S. Sali, C. M. Friend *et al.*, IEEE Trans. Appl. Supercond. **7**, 335 (1997).
[2] Y. Fukumoto, H. J. Wiesmann, M. Garber *et al.*, J. Appl. Phys. **78**, 4584 (1995).
[3] K. Kwasnitza and St. Clerc, Physica C **233**, 423 (1994).
[4] A. Oota, T. Fukunaga, M. Matsui *et al.*, Physica C **249**, 157 (1995).
[5] T. Fukunaga, T. Itou, A. Oota *et al.*, IEEE Trans. Appl. Supercond. **7**, 1666 (1997).
[6] I. A. Rudnev, A. E. Khodot, A. V. Eremin, and I. I. Akimov, Fiz. Nizk. Temp. **25**, 141 (1999) [Low Temp. Phys. **25**, 100 (1999)].
[7] A. D. Niculin, A. K. Shikov, I. I. Akimov *et al.*, IEEE Trans. Appl. Supercond. **7**, 2094 (1997).
[8] A. M. Campbell, IEEE Trans. Appl. Supercond. **5**, 682 (1995).
[9] W. T. Norris, J. Phys. D **3**, 489 (1970).

Translated by R. M. Durham

Mössbauer spectroscopy of interlayer boundaries in magneto-noncollinear $[^{57}Fe/Cr]_{12}/MgO\,(100)$ superlattices

V. V. Ustinov, V. A. Tsurin, L. N. Romashev, and V. V. Ovchinnikov

Institute of Metal Physics, Urals Branch of the Russian Academy of Sciences, Ekaterinburg
(Submitted February 10, 1999)
Pis'ma Zh. Tekh. Fiz. **25**, 88–94 (June 12, 1999)

Results are presented of Mössbauer analyses of $[^{57}Fe/Cr]_{12}/MgO\,(100)$ superlattices. A combined approach was used, based on model calculations and a method of reconstructing the density distribution function $P(H_{hf})$ of the hyperfine fields. This procedure allowed us to systematically subtract the subspectra from the different neighborhood configurations of the resonant ^{57}Fe atom. A detailed structural model was obtained for the Fe–Cr transition region from a ''pure'' Fe layer to a ''pure'' Cr layer. A deflection of the magnetic moment of the Fe atoms from the plane of the superlattice layers was identified in the interface of the Fe and Cr layers. The specific magnetic structure of the interface regions with different angular orientations of the magnetic moments of the Fe atoms relative to the plane of the layers (between 0 and 90°) is attributed to the coexistence of strong antiferromagnetic interaction between Fe and Cr atoms and an incommensurate spin density wave in the Cr layers. [S1063-7850(99)01606-7]

It has been demonstrated theoretically and experimentally[1–5] that the conditions for the existence of noncollinear ordering in magnetic superlattices are in many respects determined by the structure of the interlayer boundaries (interfaces). Of particular interest is the magnetic structure of the interface regions. In particular, in Fe/Cr superlattices this structure may be not only an important factor in the mechanism for noncollinear ordering of neighboring Fe ferromagnetic layers but may also have a determining influence on the formation of a particular magnetic order in the Cr layers, induced by the neighboring iron layers. Here we present results of an experimental investigation of the atomic and magnetic structure of the interfaces in Fe/Cr noncollinear magnetic superlattices using the nuclear gamma resonance method.

Superlattices of $[^{57}Fe/Cr]_{12}$ having iron layers of different thickness t_{Fe}, up to 95% enriched in ^{57}Fe, were grown on single-crystal MgO substrates by molecular beam epitaxy. The superlattice growth conditions and their characteristics were given by Ustinov *et al.*[6] and the results of studying their magnetic and magnetotransport properties were described by Ustinov *et al.*[6–8]

The Mössbauer measurements were made in a transmission geometry using a ^{57}Co source in a Cr matrix. The γ-radiation beam was directed along the normal to the surface of the film. The experimental spectra were analyzed mathematically using a program whose algorithm was described by Nikolaev and Rusakov.[9] We used a combined approach which included model calculations and a method of reconstructing the distribution function $P(H_{hf})$ of the hyperfine fields. The parameters obtained from the Mössbauer spectrum S_b of a film containing one comparatively thick layer of iron, Cr (40 Å)/Fe (180 Å)/Cr (40 Å)/MgO, for which the Fe–Cr interlayer boundaries make a negligible contribution to the spectrum, were used as the initial approximation for the model calculations.

The results of calculating the distribution function $P(H_{hf})$ (number of sextets, magnitude of the hyperfine field, and the intensity ratio of the various sextets) were used as the basis for a model to unravel the subspectra for the interlayer boundary. By calculating the Mössbauer spectra of superlattices having Fe layers of different thickness we determined the total intensities I_b and I_i of the spectra S_b and S_i for atoms of the bulk iron (bulk Fe) and the set of Fe atoms in the interlayer boundary (interface Fe). Figure 1 give the relative intensity of the spectrum for bulk (''pure'') α-Fe in samples of these superlattices plotted as a function of the thickness of the Fe layers determined by small-angle x-ray diffraction. It can be seen that when the thickness of the Fe layers is less than 8 Å, no fraction of bulk (pure) Fe occurs in these layers.

Assuming that the values of I_i and I_b are respectively proportional to the average thickness of the interface layers t_i and the thickness t_b of the layers of pure α-Fe, which is equal to $t_{Fe}-t_i$, we can write

$$I_i = kt_i; \quad I_b = k(t_{Fe}-t_i). \tag{1}$$

Having determined the nominal thickness of the iron layers t_{Fe} in these superlattices from the x-ray measurements, we can use the formulas (1) to calculate the average thickness of the interface layers (having in mind the average for both sides of the Fe layer):

$$t_i = \frac{t_{Fe}}{1+\dfrac{I_b}{I_i}}. \tag{2}$$

The average thickness of the interface layer thus calculated for these samples was between two and three lattice

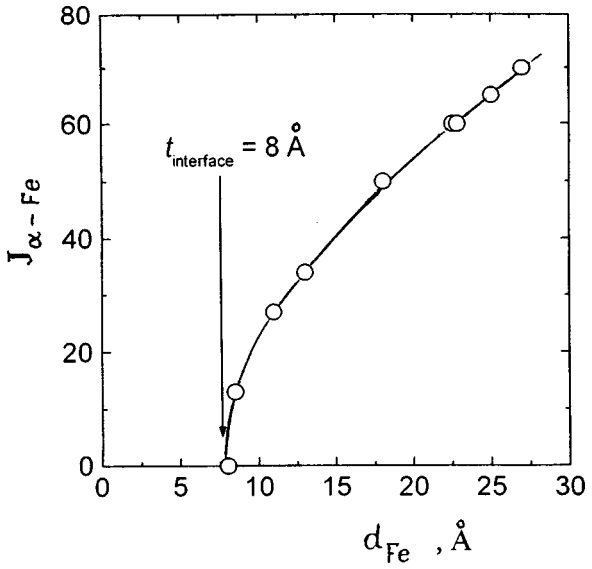

FIG. 1. Bulk fraction of pure α-Fe in layers of Fe/Cr superlattices determined from calculations of nuclear gamma resonance spectra as a function of the thickness of the Fe layers obtained from results of an x-ray analysis.

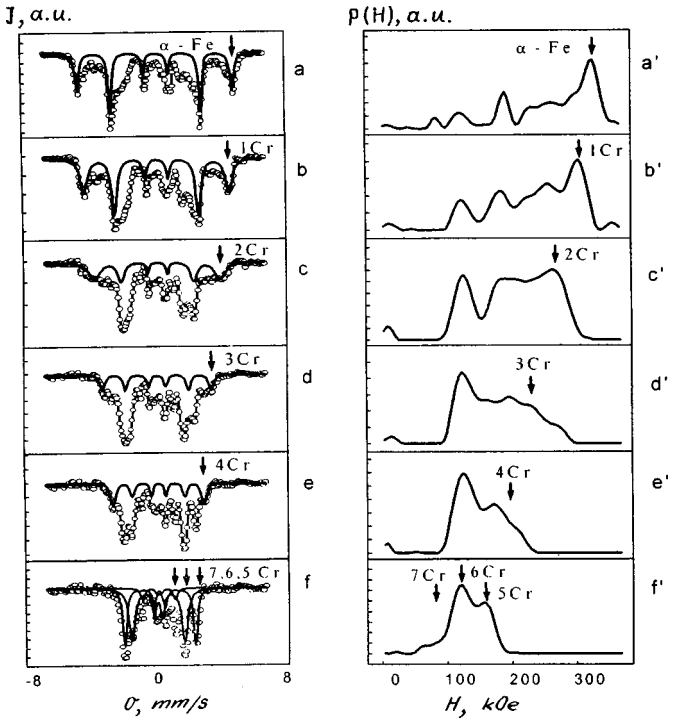

FIG. 2. Procedure for mathematical treatment of the Mössbauer spectrum of ^{57}Fe in superlattices by systematic subtraction of the subspectra $S_{n\mathrm{Cr}}$ for different configurations n_{Cr} (see text) and corresponding distribution functions of the hyperfine magnetic field $P(H_{\mathrm{hf}})$ for a [Cr (13 Å)/ ^{57}Fe (14 Å)]$_{12}$/Cr (90 Å)/MgO (100) superlattice.

constants. This estimate of the interface layer thickness obtained using the assumption made above is confirmed by the data plotted in Fig. 1.

In order to obtain more detailed information on the atomic and magnetic structure of the interlayer boundary in the superlattices, we carried out a procedure which involved subtracting the contribution of the bulk α-Fe from the experimental spectrum. We analyzed the functions $P(H_{\mathrm{hf}})$ for the difference spectra of these superlattices. This analysis showed that the nature of the distribution $P(H_{\mathrm{hf}})$ and specifically the number of maxima and the corresponding values of the hyperfine fields are almost the same for all the samples. We also found that the structure of the functions $P(H_{\mathrm{hf}})$ in terms of the parameters is similar to that determined earlier[10–12] from calculations of the Mössbauer spectra of solid samples of Fe_xCr_{1-x} alloys. The various $P(H_{\mathrm{hf}})$ peaks correspond to different nearest neighborhood configurations of the ^{57}Fe atom with Cr atoms whose number in the first coordination sphere is $n_{\mathrm{Cr}}=0,1,2,3,4\ldots$. The second coordination sphere influences the width of the peaks. In order to make a more accurate determination of the initial parameters of the subspectra describing the interlayer boundary (the ratios of the lines in each subspectrum, especially for spectra with small hyperfine fields corresponding to configurations with $n_{\mathrm{Cr}}\geqslant 4$), we carried out a procedure which involved systematically subtracting the model spectra $S_{n\mathrm{Cr}}$ for the various configurations, as illustrated in Fig. 2. Figure 2a shows the initial superlattice spectrum S (circles) and the spectrum S_b subtracted from it (solid curve). Figure 2c shows the result of the subtraction (the spectrum S_i) and the spectrum subtracted from it S_1 (solid curve). The procedure is then repeated for $n_{\mathrm{Cr}}=2,3\ldots 7$. At each stage the result of subtracting the sextet with the required ''weight'' was monitored from the disappearance of the corresponding peak on the distribution function $P(H_{\mathrm{hf}})$ (see Figs. 2a′–2f′).

The parameters of the sextet components $S_{n\mathrm{Cr}}$ thus obtained were then used for a model unraveling of the spectra with ''rigid'' and ''nonrigid'' coupling imposed on the variable parameters. In this case, we assumed that the line intensities in each subspectrum could vary. The results of the calculations for an analysis of the spectrum shown in Fig. 2 are presented in Table I.

Hence, this investigation has enabled us to obtain direct information on the transition region between the pure Fe and Cr layers. An important characteristic which should be noted here is the departure of the magnetic moments of the Fe atoms from the plane of the superlattice. Consequently, we are dealing with local effects on the Fe atoms in the interface. These can be attributed to magnetic interactions of Fe atoms with Cr atoms which also possess a magnetic moment and may be ordered either in a normal antiferromagnetic lattice or in an incommensurate spin density wave structure.[13] Recent neutron and synchrotron scattering studies of the spin structure of thick (greater than 1000 Å) epitaxial Cr layers coated with a 20 Å thick Fe layer have unambiguously shown[14,15] that strong antiferromagnetic coupling exists between the Fe and Cr atoms at the Fe–Cr interface, and incommensurate spin density waves are also present with the Cr magnetic moments perpendicular to the plane of the superlattice. It is natural to assume that for these samples the presence of Fe atoms in the interface region with the magnetic moment oriented normal to the plane of the superlattice may be attributed to the existence of incommensurate spin density waves in the chromium layers, where the magnetic moments of the Cr atoms are perpendicular to the plane of the layers. However, the possibility of such waves existing in

TABLE I. Results of calculating the parameters of Mössbauer spectra using the procedure described in the text for mathematical treatment of the gamma resonance spectrum of the magneto-noncollinear superlattice [Cr (13 Å)/^{57}Fe (14 Å)]$_{12}$/Cr (90 Å)/MgO.

	Spectrum							
	S_b	S_i						
Parameter		S_{1Cr}	S_{2Cr}	S_{3Cr}	S_{4Cr}	S_{5Cr}	S_{6Cr}	S_{7Cr}
Relative intensity of subspectra I, %	37±3	22±3	10±3	8±3	5±3	7±3	10±3	~1
Hyperfine field H_{hf}, kOe	330±3	299±3	258±3	228±3	191±3	154±3	117±3	58±3
Angle of deviation of magnetic moment from plane of film $\Delta\theta$°	0	11±10	24±10	23±5	35±5	57±10	90±5	90±10

superlattices with thin Cr layers remains open to doubt.

This work was supported by the Russian Foundation for Basic Research (Grant No. 98-02-17517) and under Project No. 97-1080 of the Program ''Physics of Solid-State Nanostructures.''

[1] A. Schreyer, J. F. Ankner, Th. Zeidler *et al.*, Phys. Rev. B **52**, 16 066 (1995).
[2] J. C. Slonczewski, J. Magn. Magn. Mater. **150**, 13 (1995).
[3] S. Demokritov, E. Tsymbal, P. Grünberg, and W. Zinn, Phys. Rev. B **49**, 720 (1994).
[4] A. Schreyer, Physica B **221**, 366 (1996).
[5] V. M. Uzdin and N. S. Yartreva, Comput. Mater. Sci. **10**, 211 (1998).
[6] V. V. Ustinov, M. M. Kirilllova, I. D. Lobov *et al.*, Zh. Eksp. Teor. Fiz. **109**, 477 (1996) [JETP **82**, 253 (1996)].
[7] V. V. Ustinov, N. G. Bebenin, L. N. Romashev *et al.*, Phys. Rev. B **54**, 15 958 (1996).
[8] V. V. Ustinov, L. N. Romashev, V. I. Minin *et al.*, Fiz. Met. Metalloved. **80**(2), 71 (1995).
[9] V. I. Nikolaev and V. S. Rusakov, *Mössbauer Studies of Ferrites* [in Russian], Moscow State University Press, Moscow (1985), p. 224 .
[10] D. Chandra and L. H. Schwartz, Metall. Trans. **2**, 511 (1971).
[11] V. L. Arbuzov, A. L. Nikolaev, V. A. Tsurin *et al.*, in *Strongly Excited States in Crystals* (Collected Works) [in Russian], Tomsk (1991), pp. 40–46.
[12] G. K. Wertheim, V. Jaccarino, J. H. Wernick, and D. N. E. Buchanan, Phys. Rev. Lett. **12**, 24 (1964).
[13] H. Zabel, P. Bodeker, and A. Schreyer, J. Phys. D: Appl. Phys. **31**, 656 (1998).
[14] P. Sonntag, P. Bodeker, A. Schreyer *et al.*, J. Magn. Magn. Mater. **183**, 5 (1998).
[15] E. Fawcett, Rev. Mod. Phys. **60**, 209 (1988).

Translated by R. M. Durham

Lasing in the vertical direction in quantum-size InGaN/GaN multilayer heterostructures

A. V. Sakharov, V. V. Lundin, V. A. Semenov, A. S. Usikov, N. N. Ledentsov, A. F. Tsatsul'nikov, and M. V. Baĭdakova

A. F. Ioffe Physicotechnical Institute, Russian Academy of Sciences, St. Petersburg
(Submitted March 3, 1999)
Pis'ma Zh. Tekh. Fiz. **25**, 1–9 (June 26, 1999)

Lasing is discovered in the direction perpendicular to the surface in quantum-size InGaN/GaN multilayer heterostructures grown by vapor-phase epitaxy. At high excitation densities one of the modes in the luminescence spectrum, which is modulated by modes of the Fabry–Pérot cavity formed by the GaN/air and GaN/sapphire-substrate interfaces, is sharply amplified and begins to dominate the spectrum. The dependence of the luminescence intensity on pump density has a clearly expressed threshold character. The threshold excitation density in the vertical direction is 5–6 times greater than the stimulated-emission threshold for observation from an end surface of the structure. The gain coefficient in the active region at the threshold for surface-emitting lasing is estimated as 2×10^5 cm^{-1}. The interaction between the cavity modes and the gain spectrum is detected in the form of displacement (by up to 2.6 nm) of modes on the short-wavelength edge of the luminescence spectrum toward higher photon energies. The characteristic temperature (T_0) measured in the range from 16 to 120 K is 480 K. At higher temperatures $T_0=70$ K. © *1999 American Institute of Physics.*
[S1063-7850(99)01706-1]

There has recently been intensive research into structures based on group-III nitrides in connection with the creation of light-emitting diodes and lasers which operate in the near-ultraviolet, blue, and green regions of the spectrum. Injection lasers with a long service life have already been obtained on the basis of InGaN/GaN quantum wells.[1]

Vertically emitting lasers are known to have several advantages over ordinary stripe lasers (small divergence of the light beam and the possibility of creating an array of lasers on a single growth substrate). However, the formation of highly reflective Bragg mirrors in the GaN/AlGaN system requires the growth of a large number of layers (>35 pairs).

It should also be noted that the specific gain coefficient of thick (~0.1 μm) InGaN layers at high excitation densities is so great that some investigators observed stimulated emission in the vertical direction with optical pumping.[2,3] On the other hand, the use of dense quantum-dot arrays in the II–VI system is known to permit the realization of lasing in the direction perpendicular to the surface even when highly reflective Bragg mirrors are not employed.[5]

In the present work we investigated the optical properties of a structure with 12 InGaN/GaN quantum wells. The structure was grown by metalorganic vapor-phase epitaxy under conditions conducive to breakup of the solid solution into indium-enriched InGaN nanodomains, which can be regarded as dense quantum-dot arrays.[6,7] The growth was carried out in a horizontal reactor with inductive heating. Hydrogen (for the growth of GaN) or argon (for the growth of InGaN/GaN) served as the carrier gas, trimethylgallium (TMG) and trimethylindium (TMI) served as the sources of the group-III elements, and ammonia served as the source of nitrogen. Polished (0001)$\pm30'$ sapphire was employed as the substrate. Before being inserted into the reactor, the substrate was degreased in organic solvents. A buffer layer of AlGaN was deposited at 530 °C. After the buffer layer was annealed at 1010 °C, an epitaxial layer of GaN with a thickness of 2.5 μm was deposited in an ammonia atmosphere at a temperature of 1050 °C and a pressure of 200 mbar. Then, the substrate temperature was lowered to 800 °C, the pressure was raised to 600 mbar, and a thin (~24 nm) layer of InGaN with a low (7–8%) indium content was grown in an argon atmosphere. Structures grown without such a low-temperature underlayer exhibited a low luminescence efficiency, which has also been noted by other researchers.[4] Quantum wells were formed by varying the substrate temperature from 730 to 850 °C (12 cycles) in the presence of constant fluxes of TMI and TMG. Such a method for forming a periodic multilayer structure permits fairly simple reconciliation of the need to lower the temperature during the growth of the InGaN layers and the need to raise the temperature to grow the GaN barrier layers. In this case variation of the TMI flux is superfluous, since the entry of In into InGaN is strongly reduced when the temperature is raised at low layer growth rates (~0.1 nm/s in the present case). Then the substrate temperature was raised to 1050 °C, and a GaN overlayer with a thickness of 0.1 μm was grown. The period of the multilayer structure and the mean composition with respect to In in the active region were determined from x-ray diffractometric data and were found to equal 12–13 nm and 8%, respectively. We estimate the effective thickness of the InGaN intrusion to be 4–5 nm on the basis of the temperature variation profile.

Photoluminescence (PL) was excited by a pulsed nitrogen laser ($\lambda=337.1$ nm) with a pulse power of 1.5 kW. When surface-emitted PL was observed, the beam was focused into a spot with a diameter of 400 μm (the excitation density was 1 MW/cm^2). To observe PL from an end sur-

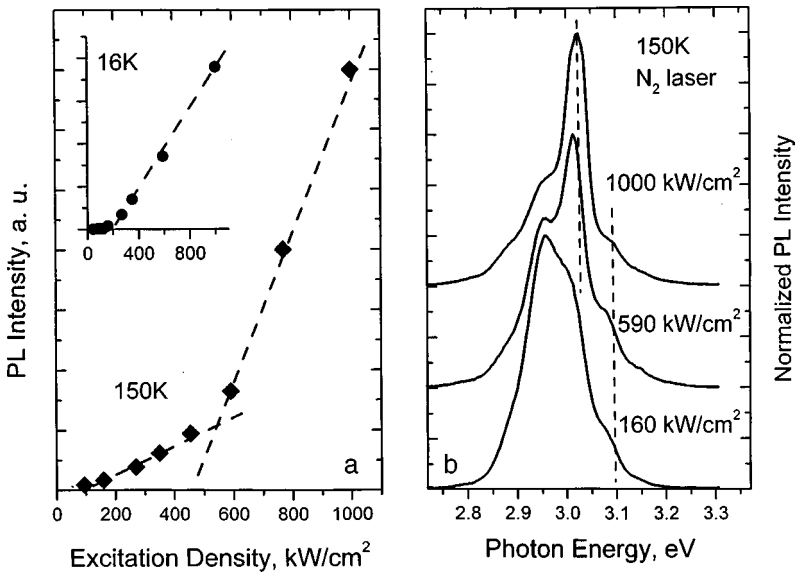

FIG. 1. Dependence of the surface-emitted photoluminescence intensity on excitation density at 150 K (the inset shows the dependence of the surface-emitted photoluminescence intensity on excitation density at 16 K) (a). Surface-emitted luminescence spectra recorded at various excitation densities (b).

face, a cavity with a length of 3 mm was cleaved, and the laser beam was focused into a spot measuring 5×0.3 mm on it by a cylindrical lens (the excitation density was 100 kW/cm^2). The pump density was lowered using neutral filters. Emission was detected by a cooled photomultiplier operating in a synchronous detection regime.

Figure 1 presents plots of the dependence of the surface-emitted photoluminescence intensity on excitation density at 16 and 150 K (Fig. 1a) and the PL spectra at various excitation densities and a temperature of 150 K (Fig. 1b). As is seen from the figure, at high excitation densities (600 kW/cm^2, 150 K) one of the modes in the luminescence spectrum modulated by the modes of the Fabry–Pérot microcavity formed by the GaN/air and GaN/sapphire-substrate interfaces intensifies sharply and begins to dominate the spectrum, while the dependence of the luminescence intensity on pump density exhibits a clear-cut threshold character. The pronounced single-mode character of the emission spectrum at high pump densities attests to the presence of feedback in the system, and the character of the far-field distribution[8] indicates passage into a lasing regime. According to our data, surface-emitting lasing has been observed for the first time in a multilayer structure with quantum-size InGaN/GaN intrusions.

The gain coefficient of the material of a multilayer structure at the lasing threshold can be estimated from the condition of equality between the losses due to the escape of radiation (α_{ext}) and the effective gain of the system (g_Σ):

$$\alpha_{\text{ext}}=\frac{1}{2L}\ln\left(\frac{1}{R_1R_2}\right)=g_\Sigma, \tag{1}$$

where R_1 and R_2 are the reflection coefficients of the GaN/Al_2O_3 (2.4%) and GaN/air (17%) interfaces and L is the cavity length. Inasmuch as the active region occupies only a small part of the total thickness of the structure, the gain coefficient of the active region should be no less than 2×10^5 cm^{-1}.

When the pump density is increased, a blue shift of the modes of the Fabry–Pérot cavity (a so-called chirp) is observed due to the variation of the refractive index in the active region. The largest shift is observed for the mode with the shortest wavelength (Fig. 2), while the long-wavelength modes are scarcely shifted. This effect can be described by the Kramers–Kroning relations, and its large value (2.6 nm) is caused by the enormous variation of the absorption (gain) coefficient in the active region. An interaction between the cavity modes and the absorption (gain) spectrum of the active medium was previously noted for surface-emitting lasers based on InGaAs/GaAs quantum dots.[9]

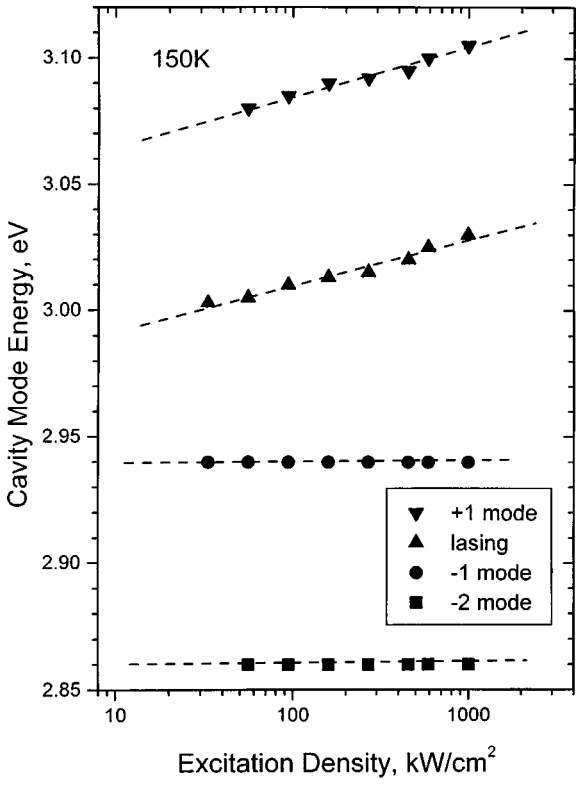

FIG. 2. Dependence of the position of the Fabry–Pérot cavity modes on excitation density at 150 K.

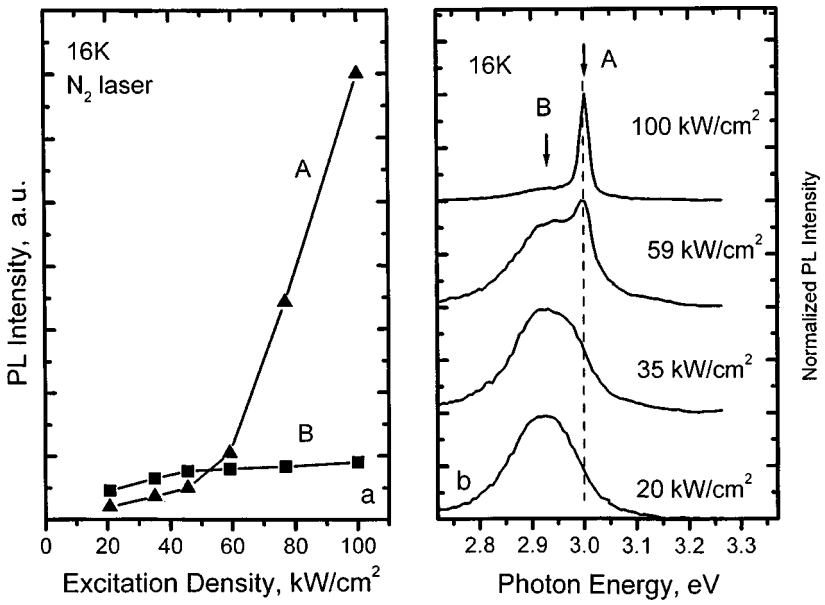

FIG. 3. Dependence of the photoluminescence intensity from an end surface on excitation density for two different lines at 16 K. The position of the lines is indicated by arrows in Fig. 3b (a). Luminescence spectra from an end surface recorded for various excitation densities (b).

Figure 3 presents plots of the dependence of the photoluminescence intensity from an end surface on excitation density for two different emission lines (Fig. 3a) and the PL spectra for various excitation densities at 16 K (Fig. 3b). The position of line *A* (3.002 eV) corresponds to the energy of the stimulated emission, and the position of line *B* (2.924 eV) corresponds to the spontaneous emission maximum. The PL line narrows sharply at pump densities of the order of 50 kW/cm^2, indicating a transition to a stimulated-emission regime. At the same time, a sharp increase in the intensity of line *A* is observed, and the growth of the intensity of line *B* (spontaneous emission) slows. It is noteworthy that stimulated emission in the direction parallel to the surface begins at significantly lower excitation densities than does surface-emitting lasing. When stimulated emission appears in the direction parallel to the surface, the radiative-recombination time decreases, preventing further growth of the gain for light emitted in the direction perpendicular to the surface. This phenomenon must be taken into account as a parasitic effect and must be maximally suppressed in designing surface-emitting lasers.

Figure 4 shows the temperature dependence of the threshold pump density for lasing in the vertical direction. At temperatures up to 120 K the threshold pump density varies slowly, and the characteristic temperature (T_0) is 480 K. Such a dependence is characteristic of lasers based on quantum-dot (QD) structures.[10] At higher temperatures the threshold pump density increases. This can be associated both with the thermal ejection of carriers from the QD's accompanied by their leakage into the GaN matrix and nonradiative recombination and with variation of the radiative-recombination time with temperature.[11] In the temperature range 100–200 K the increase in the threshold excitation density is described well by the empirical formula

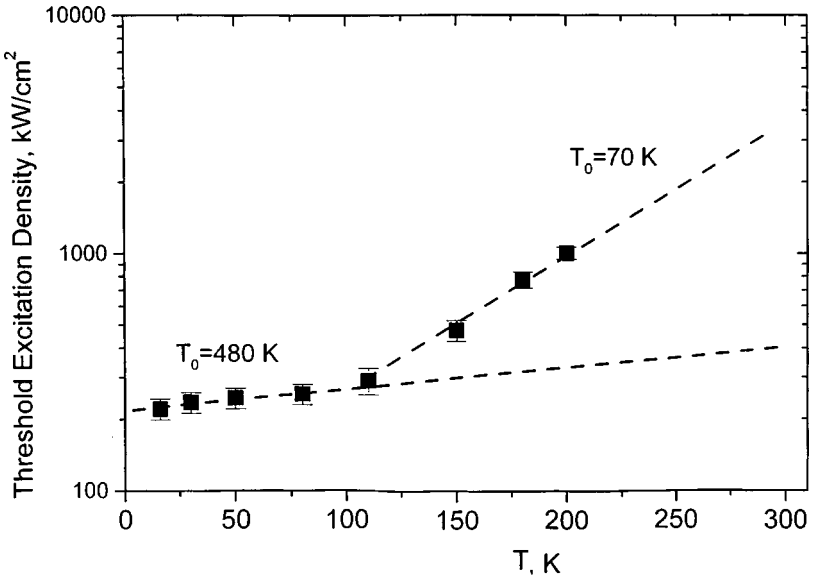

FIG. 4. Temperature dependence of the threshold excitation density for surface-emitting lasing.

$$P_{\text{th}} = P_0 \times \exp\left(\frac{T}{T_0}\right)$$

with the characteristic temperature $T_0 = 70$ K.

In the present work we showed that lasing in the vertical direction can be realized in a structure with several quantum-size InGaN/GaN intrusions even in the absence of highly reflective mirrors. The cavity for lasing in the vertical direction is formed by the GaN/Al_2O_3 and GaN/air interfaces.

[1] S. Nakamura, M. Senoh, S. Hagahama, N. Iwasa, T. Yamada, T. Matsushita, H. Kiyoku, Y. Sugimoto, T. Kozaki, H. Umemoto, M. Sano, and K. Chocho, Appl. Phys. Lett. **72**, 2014 (1998).
[2] S. T. Kim, H. Amano, and I. Akasaki, Appl. Phys. Lett. **67**, 267 (1995).
[3] M. Asif Kham, S. Krishnankutty, R. A. Skogman, J. N. Kuznia, D. T. Olson, and T. George, Appl. Phys. Lett. **65**, 520 (1994).
[4] S. Keller, B. P. Keller, D. Kapolnek, A. C. Abare, H. Masui, L. A. Coldren, U. K. Mishra, and S. P. Den Baars, Appl. Phys. Lett. **68**, 3147 (1996).
[5] I. L. Krestnikov, M. Strassburg, M. Caesar, V. A. Shchukin, A. Hoffmann, U. W. Pohl, D. Bimberg, N. N. Ledentsov, V. G. Malyshkin, P. S. Kop'ev, Zh. I. Alferov, D. Litvinov, A. Rosenauer, and D. Gethsen, in *Proceedings ICPS24, Jerusalem, August 2–7, 1998*, World Scientific, Singapore (1998).
[6] S. Nakamura, M. Senoh, S. Nagahama, N. Iwasa, T. Yamada, T. Matsushita, Y. Sugimoto, and H. Kiyoku, Appl. Phys. Lett. **70**, 2753 (1997).
[7] A. Vertikov, A. V. Nurmikko, K. Doverspike, G. Bulman, and J. Edmond, Appl. Phys. Lett. **73**, 493 (1998); K. Tachibana, T. Someya, and Y. Arakawa, Appl. Phys. Lett. **74**, 383 (1999); R. W. Martin, P. G. Middleton, K. P. O'Donnell, and W. Van der Stricht, Appl. Phys. Lett. **74**, 263 (1999).
[8] A. V. Sakharov (to be published).
[9] N. N. Ledentsov, D. Bimberg, V. M. Ustinov, M. V. Maximov, Zh. I. Alferov, V. P. Kalosha, and J. A. Lott, Semicond. Sci. Technol. **13**, 99 (1999).
[10] N. Kirstaedter, N. N. Ledentsov, M. Grundmann, D. Bimberg, U. Richter, S. S. Ruvimov, P. Werner, U. Gosele, J. Heydenreich, V. M. Ustinov, M. V. Maximov, P. S. Kop'ev, and Zh. I. Alferov, Electron. Lett. **30**, 1416 (1994).
[11] Y. Cho, G. H. Gainer, A. J. Fischer, J. J. Song, S. Keller, U. K. Mishra, and S. P. Den Baars, Appl. Phys. Lett. **73**, 1370 (1998).

Translated by P. Shelnitz

Fluctuational electromagnetic interaction of the tip of a scanning microscope with the surface of a solid

G. V. Dedkov and A. A. Kyasov

Kabardin-Balkar State University, Nal'chik
(Submitted December 22, 1998)
Pis'ma Zh. Tekh. Fiz. **25**, 10–16 (June 26, 1999)

A general formula for the lateral frictional force acting on the tip of a scanning microscope moving parallel to a surface with a velocity V is obtained within fluctuational electromagnetic theory. The contributions of various polarization mechanisms to this force are analyzed. The dependences of the lateral forces on the velocity, radius of curvature, and distance of the tip from the surface, as well as the temperature and the dielectric properties of the tribological contact are obtained. It is shown for the first time that the lateral forces can change sign and become accelerating for a definite combination of dielectric functions of the tip and the surface. © *1999 American Institute of Physics.* [S1063-7850(99)01806-6]

Experiments performed with atomic-force and other types of scanning probe microscopes raise several pressing questions concerning the role of the various mechanisms underlying the lateral frictional interaction of the sensitive element, i.e., the tip, with the sample surface. As was noted in Refs. 1–4, one of these mechanisms is the dynamic (which depends on the velocity of the tip) fluctuational electromagnetic interaction, which leads to a decelerating force of the form

$$\mathbf{F}=-\eta\mathbf{V}, \tag{1}$$

where the coefficient η depends on the shape of the tip and the distance z between its apex and the surface, as well as on the dielectric properties of the system. Formula (1) corresponds to the first nonvanishing term in the expansion in the velocity, which is valid at small $\mathbf{V}$.

For typical values of the scanning parameters (a frame advancement frequency equal to 1–10 kHz and a frame size equal to 10–1000 nm) the velocity of the tip falls in the range $10^{-6}-10^{-2}$ m/s, but in a vibratory regime it can reach 1–10 m/s. These or even somewhat greater velocities are possibly characteristic of the experimentally observed ''stick-slip'' motion of a tip in a stiffer contact.[5]

An analysis of the existing reports devoted to the calculation of η for a nonrelativistic spherical atom moving parallel to a surface reveals uncertainty both in the value of the exponent in the dependence of η on the distance z to the surface and in the value of the numerical coefficient. For example, an $\eta\sim z^{-10}$ dependence was obtained in one of the first studies focusing on this question,[6] and an $\eta\sim z^{-5}$ dependence was subsequently obtained in Refs. 7 and 8, as well as in our previous study.[9] In the present work, by not confining ourselves to the condition of a zero temperature T used in Ref. 9, we obtained a more general formula for the lateral force acting on a moving nonrelativistic atom:

$$F(z,V)=\frac{2\hbar}{\pi^2 V}\int d\omega\int\int dk_x\,dk_y k\exp(-2kz)\times\coth\left(\frac{\omega\hbar}{2kT}\right)\{(\omega+k_xV)[\Delta''(\omega)\alpha''(\omega+k_xV)-\Delta''(\omega+k_xV)\alpha''(\omega)]+(\omega-k_xV)\times[\Delta''(\omega)\alpha''(\omega-k_xV)-\Delta''(\omega-k_xV)\alpha''(\omega)]\}, \tag{2}$$

where $k=\sqrt{k_x^2+k_y^2}$, $\alpha''(\omega)=\mathrm{Im}(\omega)$, $\Delta''(\omega)=\mathrm{Im}(\varepsilon(\omega)-1/\varepsilon(\omega)+1)$, $\alpha(\omega)$ is the dynamic polarizability of the atom, and $\varepsilon(\omega)$ is the dielectric function of the surface. The integration is carried out over positive frequencies and positive values of the wave-vector projections k_x and k_y.

It is not difficult to see that the expansion of the force (2) into a series for small velocities (the velocities characteristic of probe microscopes can be considered small) contains only odd powers of V. In particular, in the linear approximation, after integration over the wave vectors, for η we have

$$\eta(z)=\frac{3\hbar}{8\pi z^5}\int_0^\infty d\omega\left\{2\left[\alpha''(\omega)\frac{d\Delta''(\omega)}{d\omega}-\Delta''(\omega)\frac{d\alpha''(\omega)}{d\omega}\right]+\omega\left[\alpha''(\omega)\frac{d^2\Delta''(\omega)}{d\omega^2}-\Delta''(\omega)\frac{d^2\alpha''(\omega)}{d\omega^2}\right]\right\}\coth\left(\frac{\omega\hbar}{2kT}\right). \tag{3}$$

The main difference between this formula and the analogous expression in Ref. 8 is that the dielectric part, rather than the Planck distribution, is differentiated under the integral sign [we note that the hyperbolic cotangent in (3), unlike the Planck distribution, also takes into account the zero-point vibrations]. Therefore, $\eta(z)\neq 0$ at $T=0$ [compare this with Eqs. (63) and (65) in Ref. 8]. In the latter case, after some

simplifications associated with integration by parts, formula (7) can be brought into the more compact form

$$\eta(z)=\frac{3\hbar}{4\pi z^5}\int_0^\infty d\omega\,\alpha''(\omega)\frac{d\Delta''(\omega)}{d\omega}. \tag{4}$$

We note that this formula is distinguished from the expression used in Refs. 2 and 3 by an additional coefficient equal to 1/2, since the term with the second derivative was not taken into account in (3) in those studies.

To calculate the decelerating force of an extended body (the microscope tip) moving with a velocity V over a surface, the spectrum of electromagnetic functions for a tip of arbitrary shape must be calculated as part of a rigorous solution. Since this is a very tedious task, in a first approximation we shall employ additive summation of the forces on the basis of the formulas obtained above. The possibility of employing the additivity approximation is supported by the results of the calculations of the van der Waals forces in Refs. 10–12, in which it was shown that the geometric effects do not exceed 20–25% in the worst case (they are more often considerably smaller), and do not influence the power law of the variation of the force with distance from the surface.

Assuming that the tip has the shape of a paraboloid of revolution [with the canonical equation for its surface $z=(x^2+y^2)/2R+h$, where R is the radius of curvature and h is the distance between the tip apex and the surface], let us integrate formula (3) over the tip volume after preliminarily expressing the polarizability $\alpha(\omega)$ of the atom according to the Clausius–Mossotti formula. As a result, in the linear approximation with respect to the velocity we obtain

$$\eta(z)=\frac{3}{64\pi}\frac{\hbar R}{h^3}J(\varepsilon_1(\omega),\varepsilon(\omega)). \tag{5}$$

Here the functional $J(\varepsilon_1(\omega),\varepsilon(\omega))$ is defined by the expression

$$\begin{aligned}J(\varepsilon_1(\omega),\varepsilon(\omega))=\int_0^\infty \coth\left(\frac{\omega\hbar}{2kT}\right)\Bigg\{2\Bigg[\tilde{\Delta}''(\omega)\frac{d\Delta''(\omega)}{d\omega}\\ -\Delta''(\omega)\frac{d\tilde{\Delta}''(\omega)}{d\omega}\Bigg]\\ +\omega\Bigg[\tilde{\Delta}''(\omega)\frac{d^2\Delta''(\omega)}{d\omega^2}\\ -\Delta''(\omega)\frac{d^2\tilde{\Delta}''(\omega)}{d\omega^2}\Bigg]\Bigg\}d\omega,\end{aligned} \tag{6}$$

where $\tilde{\Delta}''(\omega)=\mathrm{Im}[\varepsilon_1(\omega)-1/\varepsilon_1(\omega)+2]$ and $\varepsilon_1(\omega)$ is the dielectric constant of the tip.

The temperature dependence of $J(\varepsilon_1(\omega),\varepsilon(\omega))$ is strong if $\omega\hbar\leqslant 2kT$ and $\coth(x)\to x^{-1}$, and the main contribution to the integral is associated with the low-frequency portion of the spectrum. Since at room temperature $2kT\approx 0.05$ eV, the corresponding polarization mechanisms include dipolar relaxation in insulators, infrared absorption in ionic crystals, and low-frequency absorption in conductors (in the wavelength range 20 μm – 0.2 m). In these cases the friction coefficient η is clearly proportional to the temperature, if we disregard the influence of the latter on the dielectric constants appearing in the integral. For optical mechanisms of absorption the temperature dependence of the integrand in (6) vanishes, and we can use the following formula, which is similar to (4):

$$J(\varepsilon_1(\omega),\varepsilon(\omega))=2\int\tilde{\Delta}''(\omega)\frac{d\Delta''(\omega)}{d\omega}d\omega. \tag{7}$$

Let us move on to a numerical estimation of the friction forces in tribological contacts with different polarizability mechanisms, using known expressions for the dielectric functions:

a) the dielectric function for the orientational mechanism in the Debye approximation [τ is the relaxation time, and $\varepsilon(0)$ is the static dielectric constant]

$$\varepsilon(\omega)=1+\frac{\varepsilon(0)-1}{1-i\omega\tau}; \tag{8}$$

b) the dielectric function of ionic crystals near the infrared absorption peak [ω_0 is the frequency of the transverse optical phonon, $\varepsilon(\infty)$ is the high-frequency dielectric constant, and γ is the linewidth]

$$\varepsilon(\omega)=\varepsilon(\infty)+\frac{\varepsilon(0)-\varepsilon(\infty)}{1-(\omega/\omega_0)^2+i\gamma\omega/\omega_0^2}; \tag{9}$$

c) the dielectric function of conducting crystals in the Drude approximation [w_p is the plasma frequency, and $\varepsilon(0)=1$ in the case of metals]

$$\varepsilon(\omega)=\varepsilon(0)-\frac{(\omega_p\tau)^2}{1+(\omega\tau)^2}+\frac{i(\omega_p\tau)^2}{\omega\tau(1+(\omega\tau)^2)}. \tag{10}$$

Concrete numerical calculations of the integral J were performed: 1) for a contact between pieces of quartz glass [formula (6) for various values of $\varepsilon(0)$ and τ; the corresponding plots are shown in Fig. 1]; 2) a ZnS–ZnS contact [formula (7) for $\omega_0=0.005$ eV, $\varepsilon(0)=5.1$, $\varepsilon(\infty)=2.93$; the dependence on the linewidth γ is shown in Fig. 2]; 3) for a contact between conducting crystals [metals and semiconductors; the results of the calculations for various values of

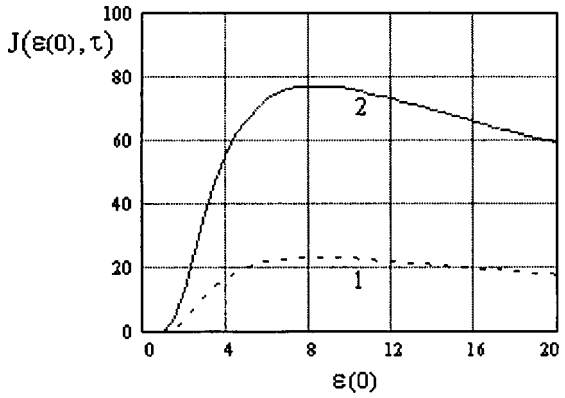

FIG. 1. Dependence of the integral J on the static dielectric constant and the relaxation time of a quartz–quartz contact in the case of an orientational dipole polarizability mechanism (1 — $\tau=3\times10^{-10}$ s, 2 — $\tau=10^{-9}$ s).

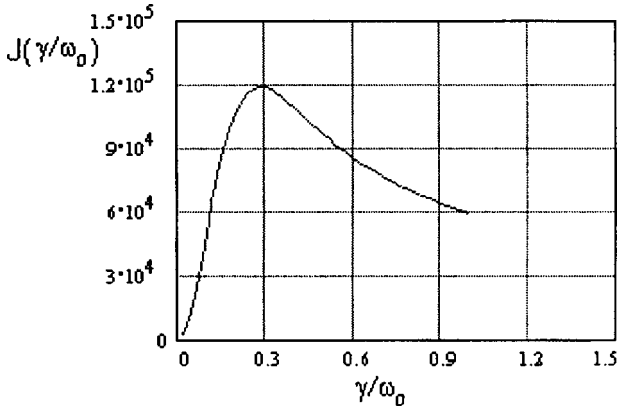

FIG. 2. Dependence of the integral J on the relative width of the infrared absorption line in a ZnS–ZnS tribological contact.

the relaxation time are listed in Table I (the values of the plasma frequencies of Ag and Au were set equal to 8.83 and 9.2 eV)]. In all cases the temperature was equal to 300 K. Substitution of the largest of the calculated values of J into Eqs. (5) and (1) gives estimates of the corresponding friction forces for $z=0.2$ mm, $R=20$ nm, and $V=1$ m/s at the 11 pN, 0.47 nN, and 0.36 pN levels. These values are within the experimental possibilities of modern probe microscopy.

TABLE I. Results of calculations of the integral J for conducting crystals.

Contact	τ, s	J
Si–Si	10^{-11}	9.6
Si–Si	10^{-15}	65.4
Ag–Ag	6.10^{-15}	76.2
Au–Au	3.8×10^{-15}	46.3
Si–Au	3.8×10^{-15}	16.7
Ge–Si	10^{-14}	−0.23
Ge–Au	3.8×10^{-15}	−8.2

A more intriguing result of the calculations (see Table 1) is the possibility of reversal of the sign of the coefficient η, i.e., we ultimately obtain an accelerating force on the tip for a definite combination of dielectric functions of the tribological partners.

Thus, the results of the present work attest to the possibility of experimentally detecting fluctuational electromagnetic forces of different sign with characteristic dependences on the temperature, tip radius, and distance between the tip apex and the surface. Measurements of these forces can provide a basis for applications of tribological contacts in the study of the dielectric properties of solids on the nanostructure level. In addition, they must be taken into account when neutral beams travel in straight and bent nanotubes (see, for example, Ref. 13).

[1] L. S. Levitov, Europhys. Lett. **8**, 499 (1989).
[2] G. V. Dedkov, in *Proceedings of the 8th International Conference on Tribology*, S. S. Eskildsen, D. S. Larsen, H. Reitz, E. L. Bienk, and S. A. Straede (Eds.), Aarhus, Denmark (1998), Vol. 1, p. 47. (the study cited as Ref. 17 of this paper should be replaced by Ref. 9 of the present work).
[3] G. V. Dedkov, Mater. Lett., (1998) (in print).
[4] G. V. Dedkov, Pis'ma Zh. Tekh. Fiz. **25**(2), 61 (1999) [Tech. Phys. Lett. **25**, 67 (1999)].
[5] M. A. Lanz, J. O'Shea, M. E. Welland *et al.*, Phys. Rev. B **55**, 10 776 (1997).
[6] W. L. Schaich and A. Harris, J. Phys. F: Met. Phys. **11**, 65 (1981).
[7] J. Mahanti, J. Phys. B: At. Mol. Phys. **13**, 4396 (1980).
[8] M. S. Tomassone and A. Widom, Phys. Rev. B **56**, 4938 (1997).
[9] A. A. Kyasov, in *Collected Scientific Papers* [in Russian], V. E. Fortov and E. A. Kuz'menkov (Eds.), IFVTAN, Moscow (1991) p. 122.
[10] Yu. N. Moiseev, V. M. Mostepanenko, and V. I. Popov, Phys. Lett. A **132**, 354 (1988).
[11] Yu. N. Moiseev, V. M. Mostepanenko, and V. I. Panov, Zh. Tekh. Fiz. **60**(1), 141 (1990) [Sov. Phys. Tech. Phys. **35**, 84 (1990)].
[12] P. Johansson and P. Apell, Phys. Rev. B **56**, 4159 (1997).
[13] G. V. Dedkov, Nucl. Instrum. Methods Phys. Res. B **143**, 584 (1998).

Translated by P. Shelnitz

Analysis of scenarios of the transition to chaos in a discrete two-mode model of a free-electron laser

A. P. Kuznetsov and A. P. Shirokov

Saratov Branch of the Institute of Radio Engineering and Electronics, Russian Academy of Sciences
(Submitted March 2, 1999)
Pis'ma Zh. Tekh. Fiz. **25**, 17–21 (June 26, 1999)

A discrete two-parameter two-dimensional mapping, which describes the dynamics of two modes in a free-electron laser (FEL), is investigated by nonlinear dynamics methods. © *1999 American Institute of Physics.* [S1063-7850(99)01906-0]

When a free-electron laser (FEL) is employed as a generator of coherent electromagnetic radiation, great importance is attached to determining the character of the interaction of the longitudinal modes, as well as of the various routes to the onset of a multiple-frequency regime. This problem can be solved using a discrete approximation, in which the interaction of the electrons with the electromagnetic wave is taken into account only at the ends of the interaction space of the FEL.[1,2] Presuming that the gain band of the generator contains many nonequidistant longitudinal modes, we can assume that the amplification of each parasitic mode is determined only by the field of the fundamental mode and depends weakly on the other parasitic modes. The following discrete mapping, which describes the dynamics of two modes in an FEL, was obtained within this approximation in Ref. 3:

$$R^{-1}x_{n+1}-x_n=L^3|J_0(y_n)J_1(x_n)|,$$
$$R^{-1}y_{n+1}-y_n=L^3|J_0(x_n)J_1(y_n)|, \quad (1)$$

where x_n and y_n are the reduced amplitudes of the fundamental and parasitic modes; n is the discrete time; R is the transmission coefficient, which is equal to the product of the reflection coefficients of the mirrors; L is the normalized length of the interaction space; and J_0 and J_1 are Bessel functions. Within the two-mode model, excitation of the fundamental mode in the absence of the competitive mode is described by J_1, and the influence of the competitive mode on it is described by J_0.

As was shown in Ref. 3, in the parameter plane of the transmission coefficient R and the normalized length of the interaction space L there are two lines: L_{st}, which corresponds to values of L at which excitation of the generator occurs at a single fundamental mode, and L_{cr}, which corresponds to excitation of the parasitic mode. At a small supercriticality $L>L_{cr}$, a steady-state regime with the generation mainly of two longitudinal modes sets in.

The relation (1), however, merits more detailed scrutiny. From the standpoint of the theory of dynamic systems, it is a discrete two-parameter two-dimensional mapping. Here we present the results of an investigation of this mapping using nonlinear dynamics methods.

A map of the dynamic regimes in the L, R plane and one magnified fragment of it are shown in Figs. 1 and 2. In these figures periodic regimes are indicated by different shades of gray, the numbers label the period of the cycle realized, and the letters s and n denote the cophasal and noncophasal regimes, respectively. Computer simulation reveals the L_{st} and L_{cr} lines, which, in terms of the discrete mapping, correspond to the following sequence of regimes. At $L<L_{st}$ there is a single stable fixed point at the origin of coordinates of the phase plane, i.e., at $x=0, y=0$. It becomes unstable at the $L=L_{st}$ line, and a new fixed point, for which $x>0$ and $y=0$, appears. As L increases further from L_{st} to L_{cr}, the value of x increases to a definite value, and at the moment when $L=L_{cr}$ a fixed point, for which $x>y>0$, appears in a soft manner. This corresponds to the birth of a second parasitic mode.

It is not difficult, however, to see that such a picture, which was predicted in Ref. 3, is observed only on the right-hand side of the map of dynamic regimes, i.e., at fairly large values of the transmission coefficient R. At small values of R the following occurs: the fixed point with the coordinates $x>0$, $y=0$ undergoes a period-doubling bifurcation, while the second mode remains undisturbed, and the birth of a

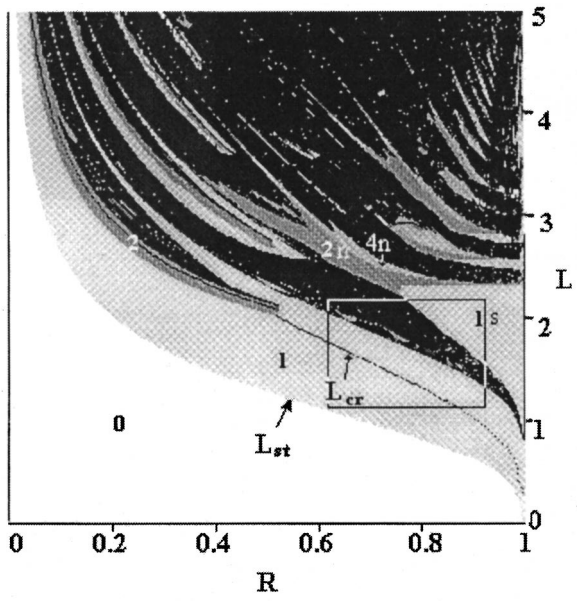

FIG. 1.

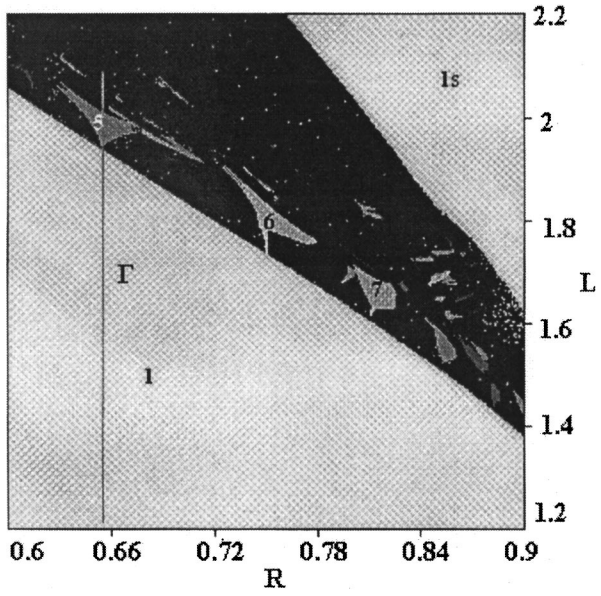

FIG. 2.

parasitic mode occurs only when L increases further. Thus, in the range $R<0.5$, of the two possible mechanisms for a loss of stability of the single-frequency regime, viz., the amplitude regime (which is caused by modulation of one longitudinal mode) and the frequency regime (which is caused by competition between different modes), only the first is realized in the two-mode model of an FEL investigated.

Let us next examine the behavior of the mapping (1) when L exceeds the critical value L_{cr}.

In the region $R<0.5$ the birth of two invariant curves from two points which previously belonged to a cycle of period 2 takes place on the x, y phase plane as L increases. (In terms of the original generator, self-modulation of the modes with incommensurate frequencies under consideration takes place). Then this ''2-torus'' breaks up through a lose of smoothness to form a chaotic attractor.

If the dimensionless length of the interaction space is increased at $R>0.5$, we discover a ''neutrality line,'' toward which numerous synchronization tongues extend. The magnified fragment of the map in Fig. 2 shows tongues, which correspond to rotation numbers equal to 1/5, 1/6, and 1/7. As we move along line Γ on the parameter plane with increasing L, computer simulation of the phase portraits reveals synchronization with the formation of a cycle of period 5. Then an invariant curve arises from each of the five points of the cycle. As L is increased further, ''corners'' appear on these curves, and an intricate attractor, which has a positive Lyapunov exponent, forms. Finally, after an even larger increase in L, two Lyapunov exponents become positive, attesting to the presence of hyperchaos in the system. As we move over the parameter plane, an invariant curve is observed near the left-hand boundary of the synchronization tongue with a rotation number of 1/5. This curve loses its smoothness and breaks up in accordance with the Afraĭmovich–Shil'nikov theorem to form a chaotic attractor.

Another region for the existence of a stable fixed point can be detected on the right-hand side of the map of dynamic regimes. In this case a regime of cophasal oscillations, in which $x=y$, is realized (i.e., in terms of the original system, the generation of a fundamental mode and a parasitic mode with equal amplitudes is observed). In Fig. 1 this region is labeled 1s. This regime of parameter variation also becomes unstable, and period doubling occurs. It is significant that the 2-cycle generator is asymmetric. Then a noncophasal 4-cycle and an 8-cycle appears, the boundaries of their regions of stability having a complex form. Thereafter, quasiperiodic, chaotic, and hyperchaotic regimes appear again.

We note that the regions of hyperchaos occupy a considerable fraction of the parameter plane, so that this regime is quite typical for the mapping (1).

Our treatment revealed fine details and interesting features of the complex regimes of a model mapping, which describes the dynamics of an FEL with a low-Q electrodynamic system. The results presented here, especially the map of dynamic regimes, can serve as a useful ''guide'' for computer investigations of the original equations in partial derivatives.

We express our thanks to S. P. Kuznetsov and D. I. Trubetskov for a useful discussion and for taking an interest in this work.

This work was supported by Russian Fund for Fundamental Research (RFBR) Grants No. 97-02-16414 and No. 96-15-96921.

[1] N. S. Ginzburg and S. P. Kuznetsov, in *Relativistic High-Frequency Electronics* [in Russian], Gor'kiĭ, (1981), No. 2, p. 101.
[2] A. P. Kuznetsov and A. P. Shirokov, Izv. Vyssh. Uchebn. Zaved., Ser. Prikl. Nelineĭnaya Din. **5**(6), 76 (1997).
[3] V. L. Bratman and A. V. Savilov, Izv. Vyssh. Uchebn. Zaved., Ser. Prikl. Nelineĭnaya Din. **2**(6), 27 (1994).

Translated by P. Shelnitz

Electric-field-controlled memory effect in heterostructures for gas sensors

R. B. Vasil'ev, M. N. Rumyantseva, L. I. Ryabova, B. A. Akimov, A. M. Gas'kov, M. Labeau, and M. Langlet

M. V. Lomonosov Moscow State University, Moscow; Institut National Polytechnique de Grenoble, St. Martin d'Hères, France

(Submitted March 3, 1999)
Pis'ma Zh. Tekh. Fiz. **25**, 22–29 (June 26, 1999)

A capacitive gas sensor has been created on the basis of an n-$SnO_2/SiO_2/p$-Si heterostructure with two successive oxide layers. The presence of polar C_2H_5OH, NH_3, and H_2O gas molecules in air leads to a significant increase in the capacitance of the structure at room temperature. An important feature of the adsorption process is a memory effect, which is confined to the possibility of maintaining the capacitance value after removal of the active component from the gas mixture. The possibility of quenching the accumulated useful signal by electric-field pulses has been realized for the first time as applied to gas sensors. © *1999 American Institute of Physics.* [S1063-7850(99)02006-6]

1. Resistive gas sensors with a working element based on metal oxides are widely used for detecting hydrogen, oxygen, carbon monoxide, hydrogen sulfide, and other gases in the atmosphere. Their mechanism of action is based on detecting a change in the conductivity of the oxide film under the conditions of gas adsorption. Optimization of the parameters of these sensors, i.e., their gas sensitivity, selectivity, speed, etc., requires the development of new approaches, including the creation of complex structures, whose electrophysical characteristics can be influenced by the adsorption of gases on artificially created interfaces.[1–5] A family of such structures has already been created, the simplest among them being a diode based on a nonohmic contact with an oxide film. More complicated MOS (metal-oxide-semiconductor) structures with a tunnel contact operate in a regime with either measurement of the capacitance or detection of a change in the threshold voltage of the structure. The operating principle of such structures is based on variation of the actual potential on the interface created by an externally applied bias in response to the formation of a dipolar layer of adsorbed gas molecules. In practice, this effect leads to displacement of the current-voltage (IVC) and capacitance-voltage (CVC) characteristics of the structure along the bias (V) axis. Thus, the useful signal recorded when the capacitance C is measured in an active gas medium at a fixed bias has a fundamental amplitude constraint, which is determined by the difference $\Delta C = C_{\max}(V<0) - C_{\min}(V>0)$ for the CVC's under stationary conditions.

2. The n-$SnO_2/SiO_2/p$-Si structures synthesized and investigated in the present work can be regarded as a combined variant of the structures described above. A cross-sectional view of these structures is shown in Fig. 1. Single-crystal p-type silicon with a resistivity $\rho = 10\ \Omega\cdot$cm served as the substrate. A SiO_2 underlayer with a thickness of 0.035 μm was deposited by the aerosol-gel method.[6] The SiO_2 obtained in such a way has several features which distinguish it from the thermally oxidized material traditionally employed as the insulating layer in MOS structures. The refractive index of the layer obtained equals 1.488, which is somewhat higher than the value for thermally grown silicon dioxide (1.47). A Fourier-transform IR-spectroscopic investigation of SiO_2 layers obtained by the aerosol-gel method showed that each layer contains residual charged radicals [alkoxy groups and protons (H^+)], which can form regions of mobile space charge.

A nanocrystalline SnO_2 film with a thickness of 0.80 μm was deposited by the pyrolysis of an aerosol.[7] The structure of the film was investigated using x-ray diffraction analysis, scanning electron microscopy, atomic-force microscopy, and Auger electron analysis. It was found that the film has a porous microstructure and consists of grains measuring 3–8 nm in diameter, which are assembled in agglomerates with a mean diameter of the order of 0.1 μm. The resistivity of the films was 10 $\Omega\cdot$cm. It was established by special measurements that the gold contact on the nanocrystalline SnO_2 film is ohmic.

3. The CVC's of the structure were measured in the system by determining the total impedance at a working frequency of 1 kHz. Since the structures investigated comprise a fairly complex system, a correct representation requires consideration of an equivalent circuit, which, in the general case, includes the capacitances on the grain boundaries of the nanocrystalline SnO_2 layer and the capacitances on the SnO_2/SiO_2 and SiO_2/Si interfaces, as well as the resistances corresponding to the various conductive channels. It is noteworthy that the structures have a finite conductivity (of the order of tens of μS) in the ac measurements. The factor responsible for the finite conductivity may be the presence of charged radicals and protons in the SiO_2 layer. The CVC's presented in this report can be regarded as plots of a certain effective capacitance of the entire structure as a whole. All the measurements were performed at $T = 20\,^{\circ}$C.

Figure 2 shows CVC's of the structures investigated, whose linear branches correspond to a positive bias applied to the Al/Si contact. Curve *1* corresponds to the ground state of the structure with a low value of $C(V=0) = 0.1$ nF. In the

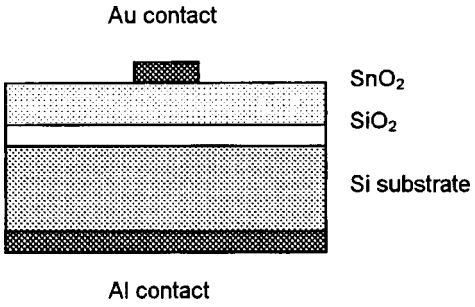

FIG. 1. Cross-sectional view of an n-$SnO_2/SiO_2/p$-Si heterostructure.

presence of polar gas molecules, such as H_2O, C_2H_5OH, or NH_3, a significant increase in capacitance is observed on the backward branch of the CVC. Curves *2–4* were obtained after a 10-min exposure of the structure to various gas mixtures (*2* — 1% C_2H_5OH in air, *3*— 1% H_2O in air, *4* — 1% NH_3 in air). A prolonged exposure (more than 10 h) leads to saturation of the gas sensor signal. Curve *5* in Fig. 2 corresponds to the zero-bias saturation level $C=5.8$ nF obtained after holding in air with 1% H_2O for 24 h at room temperature. It is important to note that the CVC's of the structures investigated differ qualitatively from the data obtained by Lundstrom for $Pd/SiO_2/Si$ structures.[1–3] The adsorption of gas molecules in n-$SnO_2/SiO_2/p$-Si structures leads to a significant increase in the capacitance, while the CVC's for the structures investigated in Ref. 3 are shifted along the V axis.

4. The kinetics of the variation of the capacitance in response to periodic variation of the composition of the gas medium at zero bias are shown in Fig. 3. A single cycle includes holding of the structure in air for 1 h followed by replacement of the gas medium by a mixture of air with 1% NH_3 for 2 min. As can be seen from the figure, the capacitance increases proportionally to the holding time in the gas mixture containing NH_3.

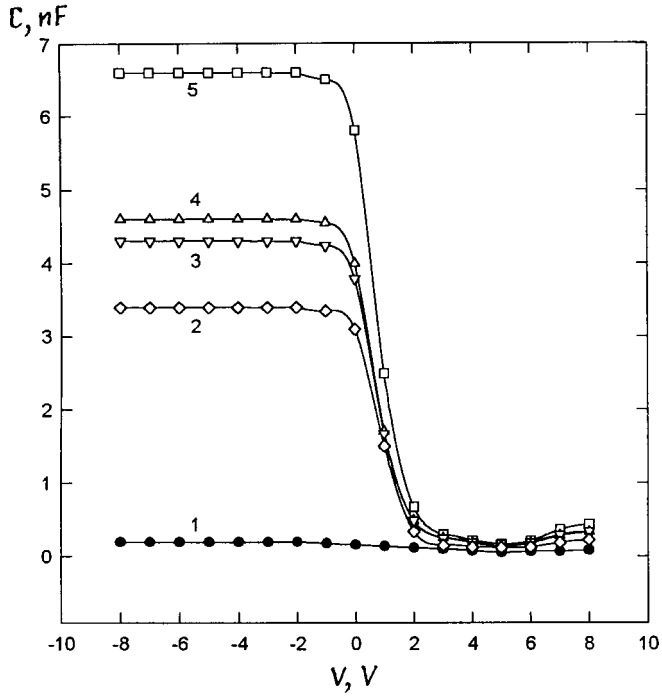

FIG. 2. Typical capacitance-voltage characteristics of an n-$SnO_2/SiO_2/p$-Si structure in air (curve *1*) after a 10-min exposure to mixtures of air and 1% C_2H_5OH (*2*), 1% H_2O (*3*), and 1% NH_3 (*4*) and after a 24-h exposure to a mixture of air and 1% H_2O (*5*). $T=20$ °C.

An important feature of the structures investigated is their ability to maintain the useful signal $C(t)$ for a long time

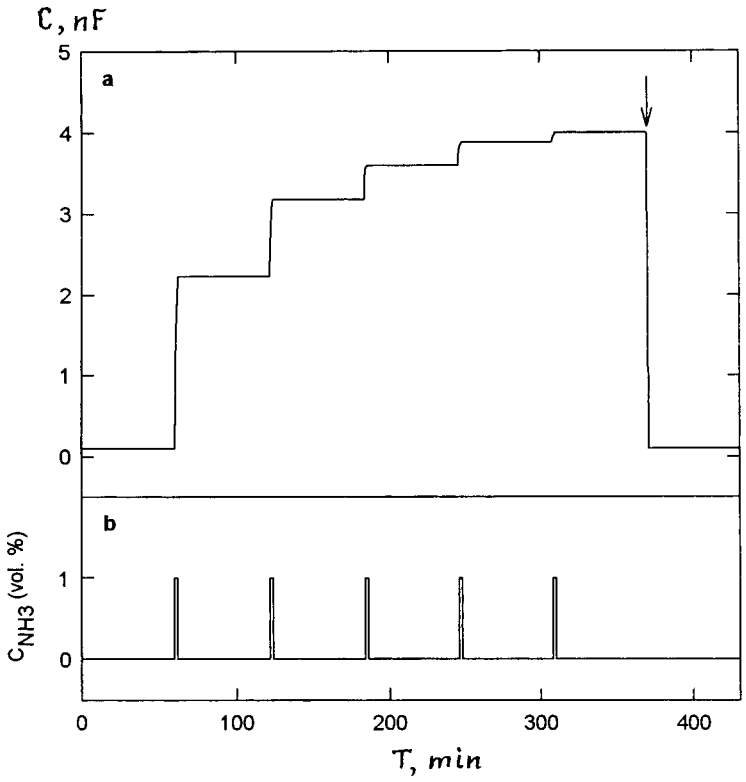

FIG. 3. Kinetics of the variation of the capacitance C of an n-$SnO_2/SiO_2/p$-Si structure in response to periodic variation of the composition of the gas phase. The arrow indicates the time of supply of a quenching electric-field pulse of reverse polarity with $V=-8$ V at $T=20$ °C (a). Temporal variation of the concentration of NH_3 in air (b).

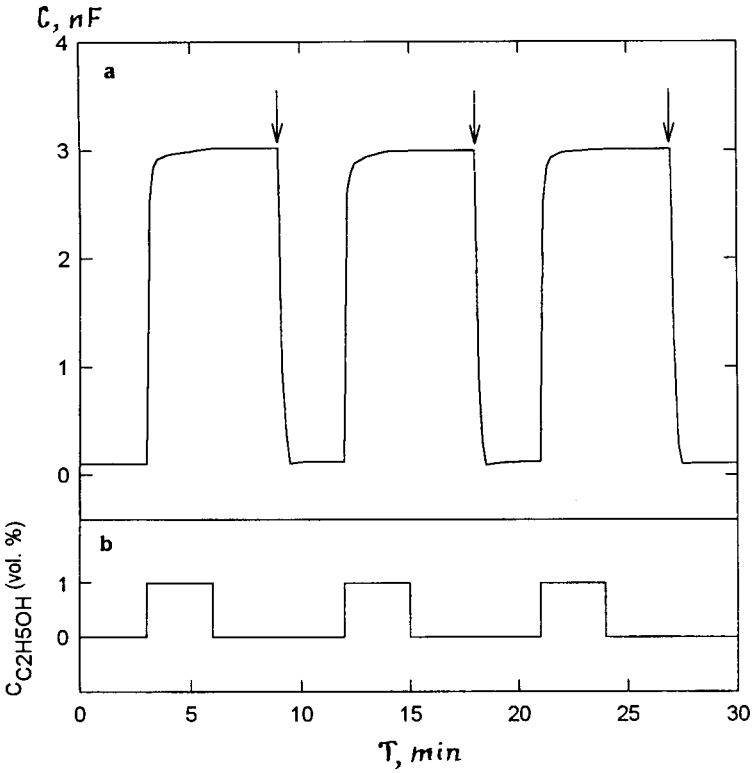

FIG. 4. Kinetics of the variation of the capacitance C of an n-$SnO_2/SiO_2/p$-Si structure in response to periodic variation of the composition of the gas phase. The arrows indicate the times of supply of a quenching electric-field pulse of reverse polarity with $V=-8$ V at $T=20$ °C (a). Temporal variation of the concentration of C_2H_5OH in air (b).

after the active component has been removed from the gas mixture. This property underlies the memory of the system for an external disturbance and permits the use of the structures under consideration as sensors which can operate in a dosimetric regime. The capacitance level achieved in the NH_3 atmosphere remains unchanged after holding in air for more than 50 h. Similar plots of $C(t)$ are observed when gas mixtures containing ethanol and water are used. The gas sensitivity S determined as the ratio $C(t)/C(t=0)$ after a 24-h exposure to gas mixtures containing 1% NH_3, C_2H_5OH, or H_2O was equal to 44, 33, and 58, respectively.

It should be stressed that the capacitative memory discovered in the n-$SnO_2/SiO_2/p$-Si structures does not have any analogs. In practice, for all the types of structures employed as capacitive gas sensors the times for a rise or fall in the useful signal in response to a change in the composition of the gas medium at a fixed temperature are comparable and are of the order of several seconds at room temperature.

5. A return to the ground state of a structure with a low capacitance value (curve *1* in Fig. 2) can be achieved by supplying an electric-field pulse of reverse polarity with an amplitude of the order of 10–15 V. Successive quenching pulses do not influence the sensor properties of the structure, as is illustrated in Fig. 4, which shows the variation of the capacitance of a structure in response to the periodic admission of a gas mixture containing ethanol. The possibility of quenching the accumulated capacitive signal by an electric field can be regarded as one of the most important advantages of the structures under consideration, since the speed of ordinary gas sensors can be increased only by heating the structure and, as a rule, their range of working temperatures is consequently in the range 100−160 °C.

6. The mechanism for the adsorption and desorption of polar gas molecules, which determines the CVC's of the structures investigated, is fairly complicated, and additional experiments, including some with simpler model objects, are needed to understand it. At the present time, we can only presume that the adsorption of molecules on the interface between the nanocrystalline SnO_2 and SiO_2 layers can be accompanied by polarization of the weakly bonded alkoxy groups and H^+ ions in the SiO_2 underlayer. The polarization process leads to the appearance of an internal electric field, which holds the adsorbed molecules on the interface even after removal of the source of polar molecules, and is thus responsible for the capacitive memory effect. The application of a pulse of an external field leads to the depolarization of SiO_2, desorption of the polar molecules, and a return of the system to the low-capacitance ground state. This hypothesis is indirectly confirmed by the fact that attempts to reproduce the capacitive memory effect in structures with thermally oxidized SiO_2, as well as in structures without nanocrystalline SnO_2 were unsuccessful.

More definite statements can be made regarding the prospects of the practical utilization of the structures investigated for creating gas sensors of a new type. Among their main advantages we can mention the possibility of realizing a dosimetric measurement regime together with fast quenching of the accumulated capacitive signal by electric-field pulses at room temperature in the open air. It is important to mention the broad possibilities of modifying the parameters of a sensor by varying its configuration (the thicknesses of the layers and the area of the upper gold contact), as well as by doping the nanocrystalline tin dioxide with various impurities.

[1] I. Lundstrom, S. Shivaraman, C. Svensson, and L. A. Lundkvist, Appl. Phys. Lett. **26**, 55 (1975).
[2] I. Lundstrom, S. Shivaraman, and C. Svensson, J. Appl. Phys. **46**, 3876 (1975).
[3] I. Lundstrom, Sens. Actuators **1**, 403 (1981).
[4] W. P. Kang and C. K. Kim, Appl. Phys. Lett. **63**, 421 (1993).
[5] W. P. Kang and C. K. Kim, Sens. Actuators B **22**, 47 (1994).
[6] N. Primeau, C. Vautey, and M. Langlet, Thin Solid Films (1997).
[7] M. N. Rumyantseva, A. M. Gaskov, L. I. Ryabova, J. P. Senator, B. Chenevier, and M. Labeau, Mater. Sci. Eng., B **41**, 333 (1996).

Translated by P. Shelnitz

Statistics of normal-phase clusters and magnetic-flux trapping in films of high-T_c superconductors

Yu. I. Kuz'min and I. V. Pleshakov

A. F. Ioffe Physicotechnical Institute, Russian Academy of Sciences, St. Petersburg; Center for Research on Engineering and Applied Sciences, UAEM, 62210, Cuernavaca, Morelos, Mexico
(Submitted March 15, 1999)
Pis'ma Zh. Tekh. Fiz. **25**, 30–36 (June 26, 1999)

The morphological properties of YBCO superconducting films and their relationship to magnetic and transport phenomena are considered. A geometric probability analysis of the principal statistical characteristics of normal-phase clusters is performed, and their influence on the dynamics of trapped magnetic flux under the action of a pulsed transport current is revealed. The superconducting film is treated as a percolation system. It is found that the critical currents have a statistical distribution, which is specified by the morphology of the material being studied. The critical current for passage of the film into the resistive state is found. © *1999 American Institute of Physics.* [S1063-7850(99)02106-0]

One of the promising ways to optimize the properties of superconducting materials is to raise the critical current by creating artificial pinning centers.[1–4] If a superconductor contains isolated normal-phase fragments in its bulk, they can effectively trap magnetic flux and keep vortices from moving under the effect of the Lorentz force. The purpose of the present work was to study the geometric statistical properties of normal-phase clusters and their effect on magnetic-flux trapping and on the critical currents in high-T_c superconductors.

The object of investigation was a YBCO superconducting film containing normal-phase fragments with an assigned texture. The *a* and *b* axes are oriented in the substrate plane; the normal-phase inclusions were created during growth of the film at the sites of defects on the boundary with the substrate and have a columnar structure directed along the *c* axis. The scale of the inhomogeneities along this axis significantly exceeds the film thickness; therefore, the distribution of the magnetic flux is two-dimensional. The relative coverage of the film surface by the normal phase is 19.5%. This value is significantly smaller than the percolation threshold for the transfer of magnetic flux in the transverse direction (50% in the case of two-dimensional percolation[5,6]). At the same time, the superconducting phase occupies 80.5% of the surface, ensuring percolation of the transport current in the plane of the film in the superconducting percolation cluster. Such a structure provides for effective pinning and thereby raises the critical current, since the magnetic flux is trapped in the finite normal-phase clusters and vortices cannot penetrate them without crossing the infinite superconducting cluster.

To analyze the geometric statistical characteristics of normal-phase clusters which play the role of pinning centers, an electron photomicrograph of a film containing 256 such clusters with a total area of 18.97 μm^2 was scanned. Figure 1 presents a histogram of a sampling of areas of normal-phase clusters, where the number N of clusters having areas which fall within the respective class interval is plotted along the vertical axis, and the number of the class interval n is plotted along the horizontal axis. The maximum and minimum cluster areas are equal to $S_{\max}=0.3684$ μm^2 and $S_{\min}=0.0021$ μm^2, respectively, the sample mean $\overline{S}=0.0741$ μm^2, the sample standard deviation $\sigma_s=0.0696$ μm^2, and the standard error (i.e., the standard deviation for the mean cluster area) $s=\sigma_s/\sqrt{256}=0.00435$ μm^2. The significant asymmetry of the distribution ($\gamma=1.7$), as well as the statistically insignificant (6%) discrepancy between the sample mean and the standard deviation, allow us to conclude that there is an exponential distribution of areas of the normal-phase clusters, whose probability density has the form

$$f(S)=\frac{1}{\overline{S}}\exp\left(-\frac{S}{\overline{S}}\right), \tag{1}$$

where S is the area of a normal-phase cluster.

During the experiments the sample was cooled in a magnetic field to liquid-nitrogen temperature, and the critical currents of the film were determined from the change in magnetization under the effect of transport-current pulses. When the sample was cooled in a magnetic field directed along the *c* axis to temperatures below the critical point, the magnetic flux was trapped in normal-phase clusters. The passage of current in the (a,b) plane caused a change in magnetization due to the depinning of magnetic flux from clusters in which the pinning force is weaker than the Lorentz force created by the transport current. Since a superconducting percolation cluster is formed in the film, when magnetic flux is released from pinning centers, the vortices must cross a region occupied by the superconducting phase.

In the subsequent treatment it must be taken into account that high-T_c superconductors are characterized by a short coherence length,[7] because of which weak links readily form in these materials. Such structural defects, as grain boundaries, crystallites, and especially twin boundaries, which would simply serve as scattering centers if the coherence

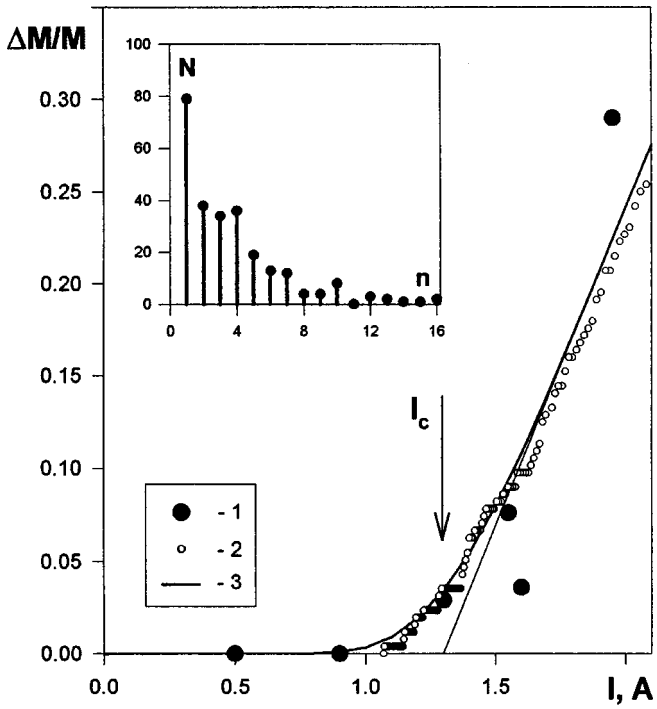

FIG. 1. Effect of a pulsed transport current on trapped magnetic flux: *1* — change in magnetization; *2* — empirical distribution function of the critical currents; *3* — exponential-hyperbolic distribution of the critical currents. Here I_c is the critical current for passage into the resistive state. The inset shows a histogram of a sampling of areas of normal-phase clusters, *N* is the number of clusters whose areas fall in the respective class interval, and *n* is the number of the class interval.

length were large, lead to the formation of weak links over a broad range of spatial scales in high-T_c superconductors. Therefore, around each normal-phase cluster there are always weak links, along which vortices travel primarily under the action of the Lorentz force.[8–12] The larger are the dimensions of the cluster, the more such weak sites are found along the perimeter of the superconducting space surrounding it and, therefore, the smaller is the critical current at which the release of magnetic flux from a given pinning center occurs. Thus, each normal-phase cluster has its own value of the critical current. On the basis of these geometric arguments, we presume that the critical current is inversely proportional to the perimeter P of the normal-phase cluster: $I \propto 1/P$. For its part, $P \propto \sqrt{S}$; therefore, $I \propto 1/\sqrt{S}$. We shall assume that the concentration of weak links per unit of length of the perimeter is constant for all clusters and that all clusters of equal area have the same pinning force. Then for geometrically similar clusters the critical current equals $I = \beta/\sqrt{S}$, where β is the form factor.

When a transport current flows, magnetic flux is depinned first from clusters which have a small pinning force, a small critical current, and, accordingly, large dimensions. Therefore, the change in the magnetization M under the action of a transport current is proportional to the number of all the normal-phase clusters whose critical current is less than the assigned value. The relative change in magnetization can be expressed in terms of the accumulated probability function $F = F(S)$ for the distribution of areas of the normal-phase clusters, which is a measure of the number of clusters whose area does not exceed an assigned value of S:

$$\frac{\Delta M}{M} = 1 - F(S), \quad \text{where} \quad F(S) \equiv \int_0^S f(S)\, dS. \tag{2}$$

Since, in accordance with the assumptions made, $S = \beta^2/I^2$, the exponential distribution of cluster areas (1) generates an exponential-hyperbolic distribution of critical currents:

$$\frac{\Delta M}{M} = \exp\left(-\frac{\beta^2}{SI^2}\right). \tag{3}$$

Thus, the entire distribution of critical currents determined by the geometric statistical properties of the normal-phase clusters can be scanned in the changes in the trapped magnetic flux caused by transport-current pulses of different amplitude. The results of such measurements are presented in Fig. 1. Each of the filled circles shows the change in magnetization of the film when a single current pulse with a duration of 100 ms is passed through it. Thermomagnetic instability, which is unavoidable when a constant current of the same amplitude is passed, does not manage to develop during such a short-lived disturbance, and the sample remains superconducting up to the maximum values of the pulse amplitude. The transverse cross-sectional area of the film was 4×10^{-5} cm^2. The measurements of the magnetization were performed using a Hall sensor with a sensitivity of 30 μV$\cdot$Gs^{-1} at a minimum measurable value of the magnetic field equal to 0.02 G.

In order to establish the relationship between the dynamics of the trapped magnetic flux and the geometric morphological properties of the superconducting structure of the film, we calculated the empirical distribution function $F^* = F^*(S)$ of the areas of the normal-phase clusters, which gives a statistical estimate of the accumulated probability function $F = F(S)$ [formula (2)]. The value of $F^*(S)$ for each order statistic was calculated as the relative number of clusters whose areas do not exceed a given value S. A coordinate transformation of the form $\{F^* \to 1 - F^*, S \to \beta/\sqrt{S}\}$ gives an empirical distribution function of the normal-phase clusters with respect to their critical currents, which is a statistical analog of the distribution function (3). The distribution of critical currents thus obtained is shown in Fig. 1 (unfilled circles). The form factor $\beta = 0.649$ A$\cdot\mu$m was calculated as a result of regression analysis: the data from the magnetic measurements (filled circles) were approximated by the exponential-hyperbolic distribution (3) using the least-squares method (curve *3*).

It is important to note that the unfilled circles are also experimental and reflect the morphological properties of the superconducting structure of the film.

As can be seen from the figure, curve *3* provides an essentially ideal description of the constant magnetization at currents less than 1 A. In the sample there are no pinning centers with such small critical currents, and since the pinning force is smaller in larger clusters, the constancy of the trapped flux in this range of transport currents is attributed to the absence of normal-phase clusters having a perimeter which exceeds a certain threshold value. The area of the

largest cluster in the sampling equals $S_{\max}=0.3684\ \mu\text{m}^2$, which corresponds to a critical current $I_{\min}=\beta/\sqrt{S}_{\max}=1.07$ A. The unfilled circles on the plot of the empirical distribution function of critical currents begins at just this value (see Fig. 1).

Each normal-phase cluster has its own value of the critical current, which makes its own contribution to the statistical distribution. This distribution can be used to find the critical current I_c, whose continuous passage causes the sample to pass into the resistive state. Figure 1 shows how to determine I_c from the x intercept of the tangent passing through the point of inflection on curve *3*. The coordinates of the point of inflection are $I=\beta\sqrt{2/(3\bar{S})}$ and $\Delta M/M=\exp(-3/2)$; the current for the transition to the resistive state is $I_c=(2/3)^{3/2}\beta/\sqrt{\bar{S}}$. The value for the film investigated is $I_c=1.3$ A, which agrees well with the data from independent measurements of critical currents.

The main result of the present work is the establishment of the decisive influence of the morphology of a superconducting structure, i.e., the statistical properties of the normal-phase clusters, on the trapping of magnetic flux and the critical currents of high-T_c superconductor films. Information on the statistical distribution of the critical currents can be obtained from the statistical properties of the geometric structure of the film. This is of direct interest for optimizing the parameters of superconducting materials, particularly for increasing the critical currents.

This work was carried out with partial financing within the Integration Program (Grant No. 679).

[1] L. Krusin-Elbaum, G. Blatter, J. R. Thompson, D. K. Petrov, R. Wheeler, J. Ullmann, and C. W. Chu, Phys. Rev. Lett. **81**, 3948 (1998).
[2] Ch. Jooss, R. Warthmann, H. Kronmüller, T. Haage, H.-U. Habermeier, and J. Zegenhagen, Phys. Rev. Lett. **82**, 632 (1999).
[3] M. R. Beasley, in *Percolation, Localization and Superconductivity (NATO Advanced Study Institutes Series, Ser. B: Physics, Vol. 109)*, A. M. Goldman and S. A. Wolf (Eds.), Plenum Press, New York (1984), pp. 115-143.
[4] A. Davidson, M. R. Beasley, and M. Tinkham, IEEE Trans. Med. Imaging **MAG-11**, 276 (1975).
[5] R. Zallen and H. Scher, Phys. Rev. B **4**, 4474 (1971).
[6] D. Stauffer, Phys. Rep. **54**, 2 (1979).
[7] J. E. Sonier, R. F. Kiefl, J. H. Brewer, D. A. Bonn, S. R. Dunsiger, W. N. Hardy, R. Liang, R. I. Miller, D. R. Noakes, and C. E. Stronach, Phys. Rev. B **59**, R729 (1999).
[8] Yu. I. Kuzmin, A. P. Paugurt, I. V. Pleshakov, and S. V. Rasumov, Supercond. Sci. Technol. **7**, 41 (1994).
[9] M. J. M. E. DeNivelle, G. J. Gerritsma, and H. Rogalla, Phys. Rev. Lett. **70**, 1525 (1993).
[10] T. Higuchi, S. I. Yoo, and M. Murakami, Phys. Rev. B **59**, 1514 (1999).
[11] A. Pautrat, Ch. Simon, A. I. Rykov, and S. Tajima, Phys. Rev. B **59**, 199 (1999).
[12] F. S. Jelila, J.-P. Maneval, F.-R. Ladan, F. Chibane, A. Marie-de-Ficquelmont, L. Méchin, J.-C. Villégier, M. Aprili, and J. Lesueur, Phys. Rev. Lett. **81**, 1933 (1998).

Translated by P. Shelnitz

Influence of the nonideality factor on the formation of a near-surface picosecond laser plasma

M. A. Yakovlev

N. É. Bauman Moscow State Technical University, Moscow
(Submitted March 2, 1999)
Pis'ma Zh. Tekh. Fiz. **25**, 37–43 (June 26, 1999)

It is shown numerically that the influence of the nonideality factor leads to an increase in the breakdown time of a dense near-surface gas by a picosecond laser pulse. [S1063-7850(99)02206-5]

The development of high-speed laser technologies with extremely rapid transfer of energy to matter (on the pico- and subpicosecond time scales) has been drawing increasingly greater attention to the interaction of ultrashort high-power laser pulses with various types of condensed matter.

When matter is irradiated by picosecond or shorter pulses ($\tau_p \leqslant 10^{-11}$ s), the interaction has a pronounced nonequilibrium character. In particular, since the characteristic values of the electron-lattice and electron-electron relaxation times in a metal target irradiated by high-power picosecond pulses are $\tau_{el} \sim 10^{-10}$ s and $\tau_{ee} \sim 10^{-15}$ s, respectively, the lattice is scarcely heated during a pulse, while the electron temperature tracks the temporal variation of the irradiation pulse.[1]

The ultrafast ionization of a near-surface dense gas (with a breakdown time $\tau_I \ll \tau_{el}$) was numerically simulated in Ref. 2. It was shown that the decisive role in the breakdown of a dense near-surface gas is played by the electrons of the electron boundary layer,[3] and the threshold values of the near-surface gas pressure p_a and the laser emission intensity I_{em} at which ultrafast ionization of the gas (the formation of a picosecond laser plasma) takes place were determined in the case of argon: $p_a \sim 100$ at and $I_{\text{em}} \sim 10^{16}$ W/m^2.

It should be noted that a picosecond laser plasma has the characteristic properties of a low-temperature, weakly ionized plasma. In particular, the nonideality properties of a dense cold plasma begin to be manifested at the pressures indicated above[4] and lead to lowering of the ionization potential of the atoms as a consequence of the interaction of the charged particles through the dense neutral gas by polarization[5] and exchange[6] mechanisms, which was not taken into account in the calculations in Ref. 2.

We also note that there has recently been a lively discussion of an exchange mechanism involving an acoustic field for the attraction of particles of like charge in connection with the problem of the formation of ordered structures in a nonideal dusty plasma.[7,8]

This report describes a numerical investigation of the effect of the lowering of the ionization potential $I \rightarrow I - \Delta I$ in a dense near-surface, weakly ionized plasma on the formation of a picosecond laser plasma. According to Refs. 5 and 6, the decrease in the ionization potential ΔI due to the polarization and exchange mechanisms is

$$\Delta I = U_e + U_i + U_{ii}, \tag{1}$$

where

$$\Delta I = \left(\frac{\hbar^2 \sqrt{\pi \sigma_e}}{m} + \frac{e^2 \alpha_a}{\varepsilon_0 d_0} + \frac{8 n_i \sigma_{ia}^2(q^+)}{9 m_i v_T^2} \right) n_a. \tag{2}$$

Here σ_e is the cross section for the elastic scattering of low-energy electrons on a gas atom; m and m_i are, respectively, the effective masses of an electron and an ion; n_i and n_a are the concentrations of ions and the neutral gas; α_a and d_0 are the polarizability and effective diameter of an atom; $\sigma_{ia}(q^+)$ is the Fourier transform of the ''ion-atom'' interaction; $q^+ \approx m_i v_T / \hbar$; and v_T is the thermal velocity of the atoms.

Thus, at high pressures it can be assumed that the decrease in the ionization potential is linearly dependent on the concentration of the neutral gas.

In the case of argon under the conditions considered above ($T_a \sim 300$ K, $n_a \sim 10^{27}$ m^{-3}) the effects of the physical mechanisms cited on the lowering of the ionization potential are comparable (U_e, $U_i \sim U_{ii}$), but the role of the exchange mechanism begins to increase as the temperature of the neutral gas decreases and the extent of ionization increases.

It should also be noted that under the conditions of a picosecond laser plasma there are additional constraints on the decisive physical factors, i.e., in order for the polarization and exchange mechanisms to be able to influence the electrophysical properties of a picosecond laser plasma, their characteristic times τ_{pol} and τ_{exch} must not exceed the pulse duration $\tau_p \sim 10^{-12}$ s.

Since the polarization interaction is of an electromagnetic nature, it is manifested under essentially any conditions [$\tau_{\text{pol}} \sim (n_a \times n_e)^{-1/3} \times \text{s}^{-1} \sim 10^{-15}$ s]. On the other hand, the exchange mechanism can manifest itself only at fairly high concentrations of the neutral gas: $\tau_{\text{exch}} \sim v_\phi^{-1} n_a^{-1/3} < \tau_p$. Thus, taking into account that the phase velocity of sound in a dense gas $v_\phi \gg v_T$ (Ref. 6), we find that the exchange mechanism for lowering the ionization potential can operate in the case of argon at $T_a \sim 300$ K only at a concentration of the neutral gas $n_a \geqslant 10^{27}$ m^{-3}, i.e., at a pressure of about a hundred atmospheres or more.

Evaluations of the expression (2) reveals that the decrease in the ionization potential in argon under the condi-

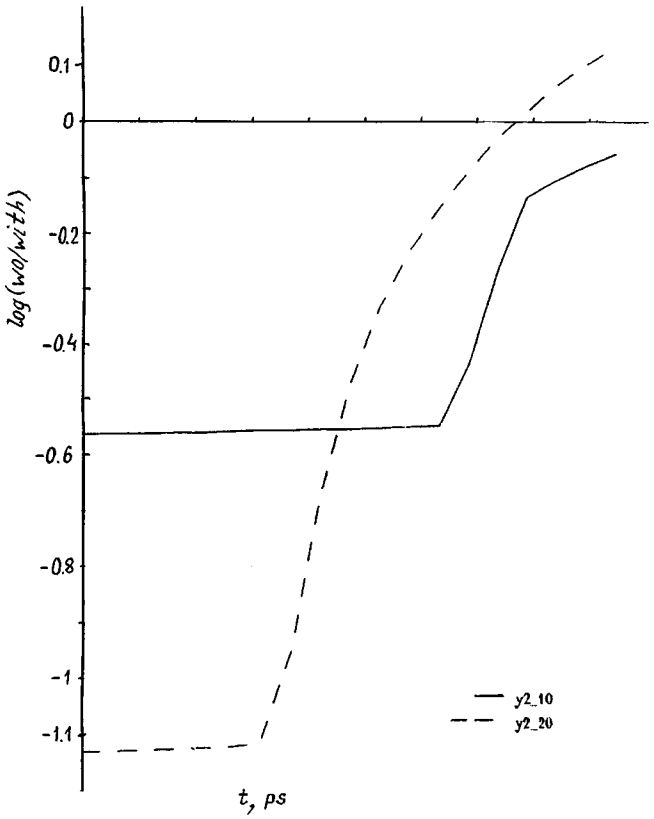

FIG. 1. Ratio of the concentrations of ions on a logarithmic scale as a function of time.

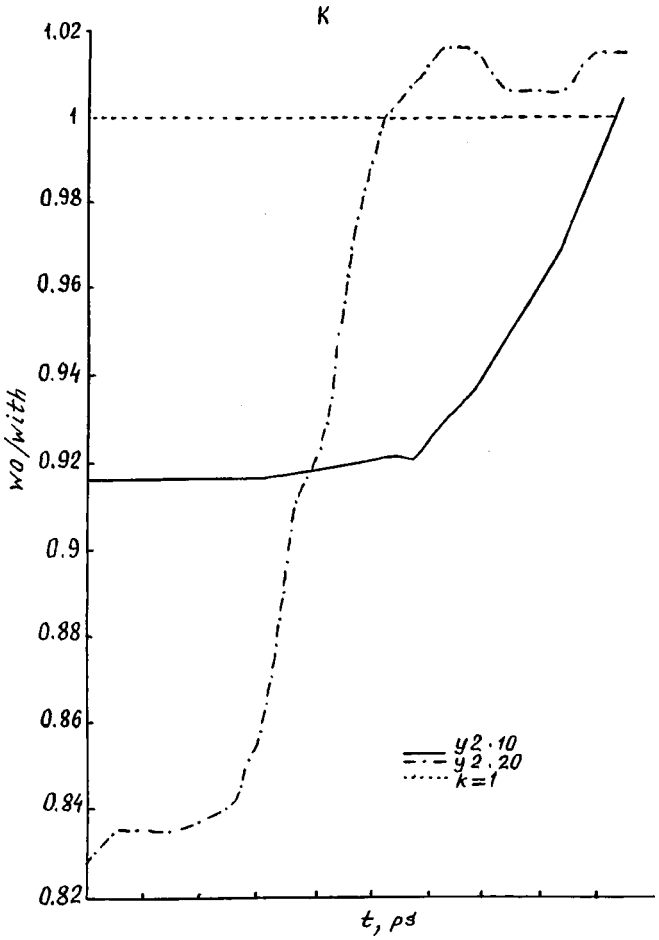

FIG. 2. Relative breakdown rate of a dense near-surface gas with consideration of the correction for nonideality.

tions indicated above reaches values of $\sim 0.15I$, i.e., the lowering of the ionization potential can have an appreciable effect on the formation of a picosecond laser plasma.

To describe the kinetics of the ionization of a gas, we solved a system of equations, which combines the heat-conduction equations for the electron temperature, the continuity equations of the electronic and ionic components, and Maxwell's equations for the electric field of an electromagnetic wave and the field of uncompensated space charge, in analogy to Ref. 2.

In contrast to Ref. 2, here we take into account the decrease in the ionization potential (2), which leads to a change in the form of the heat-conduction equation in the gas ($z>0$):

$$\frac{3}{2}k\frac{\partial T_e}{\partial t}=\frac{1}{n_e}\frac{\partial}{\partial z}\left[\chi_e\frac{\partial T_e}{\partial z}\right]-\frac{3m}{M}k(T_e-T_a)\nu_e$$

$$-\left(I-\Delta I+\frac{3}{2}kT_e\right)\nu_I+\frac{e^2|E|^2\nu_e}{2m(\omega^2+\nu_e^2)}, \qquad (3)$$

where M is the mass of a gas atom; I is the ionization potential; ν_e is the frequency of electron collisions in the gas, which is equal to the sum of the electron-ion and electron-atom collisions; and ν_I is the ionization frequency calculated from the classical Thompson formula.[9] The frequency of electron-atom collisions was calculated using the known temperature dependence of the transport scattering cross section of electrons on atoms of inert gases.[10] The following numerical parameters of the problem were chosen for the calculations: an emission wavelength $\lambda=1.06$ μm; an emission intensity $I_{\rm em}\sim 3\times10^{15}-3\times10^{16}$ W/m^2; refractive indices of the metal at the specified wavelength $\kappa_r=1.5$ and $\kappa_i=10.1$ (which corresponds to a concentration of conduction electrons in the metal $n_m=4\times10^{28}$ m^{-3}); a gas concentration $n_a=10^{27}-10^{28}$ m^{-3} (a pressure $p=40-400$ at); and an ionization potential $I=15.8$ eV (which corresponds to argon). In addition, the initial temperature T_{A0} was varied from 300 to 3000 K, which did not noticeably influence the results obtained, and the dimensions of the calculation region were $l_m=10\kappa_i^{-1}k_0^{-1}$ and $l_a=2\lambda$.

The principal finding is as follows: the lowering of the ionization potential leads to a smoother course of the ionization process.

As the calculations in the time interval from 0.1 to 3 ps showed, all other conditions being equal, a gas which has a higher ionization potential (below the label ''wo'' corresponds to such a gas) is nevertheless ionized more rapidly than a gas with a lowered ionization potential (for which the label ''with'' is used below) (Fig. 1).

Here curve $y2\_10$ corresponds to an amplitude of the electromagnetic wave $E=2\times10^9$ V/m and a concentration of the neutral gas $n_a=10\times10^{27}$ m^{-3}, and curve $y2\_20$ corresponds to $E=2\times10^9$ V/m and $n_a=20\times10^{27}$m^{-3}, respectively.

To account for this phenomenon, we must compare the effective rates of development of the ionization process of the gas (the breakdown rate) without (k_{wo}) and with consideration of the lowering of the ionization potential (k_{with}). Following Ref. 12, we can estimate the ratio between k_{with} and k_{wo} under the conditions considered:

$$\frac{k_{\text{wo}}}{k_{\text{with}}} \approx \frac{(I-\Delta I)}{I} \frac{\nu_{\text{wo}}}{\nu_{\text{with}}}, \tag{4}$$

where ν_{wo}, ν_{with} and $\sigma_I(T)$, $\sigma_{I-\Delta I}(T)$ are, respectively, the frequencies and cross sections of collisions of an electron with a neutral atom without and with consideration of the lowering of the ionization potential:

$$\nu_{\text{wo}} = n_a v_{T_{\text{wo}}} \sigma_I(T), \quad \nu_{\text{with}} = n_a v_{T_{\text{with}}} \sigma_{I-\Delta I}(T). \tag{5}$$

With consideration of (5), the expression (4) can be written in the form

$$\frac{k_{\text{wo}}}{k_{\text{with}}} \approx \frac{(I-\Delta I)}{I} \frac{v_{T_{\text{wo}}} \sigma_I(T)}{v_{T_{\text{with}}} \sigma_{I-\Delta I}(T)}. \tag{6}$$

The lowering of the ionization potential in the initial stage leads to a more intense ionization process and, accordingly, to a greater loss of thermal energy from the electrons ($v_{T_{\text{with}}} < v_{T_{\text{wo}}}$). In addition, another factor which raises the ratio (6) is the fact that, according to Ref. 10, in the electron energy range considered ($\sim 1-10$ eV) the collision cross section of electrons with atoms increases with temperature, i.e., $\sigma_{I-\Delta I} < \sigma_I$; therefore, the ratio (6) can exceed unity. This explains the paradox of a relative increase in the breakdown time of a gas with lowering of the ionization potential (Fig. 2, where $k \equiv k_{\text{wo}}/k_{\text{with}}$).

[1] S. I. Anisimov, A. M. Bonch-Bruevich, M. A. El'yashevich *et al.*, Zh. Tekh. Fiz. **36**, 1273 (1966) [Sov. Phys. Tech. Phys. **11**, 945 (1967)].
[2] A. V. Ivlev, M. A. Yakovlev, and A. N. Bordenyuk, Zh. Tekh. Fiz. **68**(8), 48(1998) [Tech. Phys. **43**, 921 (1998)].
[3] A. V. Ivlev, K. B. Pavlov, and M. A. Yakovlev, Zh. Tekh. Fiz. **64**(9), 50 (1994) [Tech. Phys. **39**, 888 (1994)].
[4] V. E. Fortov and I. T. Yakubov, *Nonideal Plasmas* [in Russian], Énergoatomizdat, Moscow (1994), 368 pp.
[5] V. A. Alekseev and A. A. Vedenov, Usp. Fiz. Nauk. **102**, 665 (1970).
[6] A. A. Vlasov and M. A. Yakovlev, Teor. Mat. Fiz. **34**, 198 (1978).
[7] M. Nambu and H. Akama, Phys. Fluids **28**, 2300 (1985).
[8] M. Nambu, S. Vladimirov, and P. Shilka, Phys. Lett. A **203**, 40 (1995).
[9] Yu. P. Raizer, *Gas Discharge Physics* [Springer-Verlag, Berlin–New York (1991); Nauka, Moscow (1987), 592 pp.].
[10] L. J. Kieffer, At. Data **2**, 293 (1971).
[11] I. A. Zel'dovich and Yu. P. Raizer, *Physics of Shock Waves and High-Temperature Hydrodynamic Phenomena* [Academic Press, New York (1966-1967); Nauka, Moscow (1966), 688 pp.].
[12] N. I. Koroteev and I. L. Shumaĭ, *Physics of High-Power Laser Radiation* [in Russian], Moscow, Nauka (1991), 312 pp.

Translated by P. Shelnitz

White-light fiber-optic intermode interferometer

O. I. Kotov, L. B. Liokumovich, S. I. Markov, A. V. Medvedev, and V. M. Nikolaev

St. Petersburg State Technical University, St. Petersburg
(Submitted March 15, 1999)
Pis'ma Zh. Tekh. Fiz. **25**, 44–50 (June 26, 1999)

An interferometric system with a low-coherence light source and two multimode fiber-optic light guides operating in an intermode interference regime is considered theoretically. It is shown that the employment of fiber-optic intermode interferometers significantly expands the range of permissible mismatch between the lengths of the reference and signal interferometers. Mismatch up to a few centimeters is possible for light-emitting diodes (LED's). The use of multimode light guides and intermode interference facilitates the construction of systems with fibers of great length and matching to an optical source. © *1999 American Institute of Physics.* [S1063-7850(99)02306-X]

White-light fiber-optic interferometers are used to measure vibrations, pressure, temperature, linear movements, etc.[1] They have a number of special features and generally employ fibers to supply the light fluxes and convey them away. Classical interferometers of the Fabry–Pérot, Michelson, and Mach–Zehnder types with small dimensions ($\sim 10^{-3}-10^{-2}$ m) are employed as the sensitive elements in such systems.

However, in some cases the use of white-light (low-coherence) interferometry with extended fiber-optic interferometers ($\sim 10^{2}-10^{3}$ m) is attractive, for example, in signaling devices and distributed sensors. It is difficult to use the known white-light systems because of the complexity of equalizing the lengths of the reference and signal interferometers to within $\sim 10^{-6}$ m. Just such equalization of the arms is employed for absolute measurements.

This paper examines a white-light system, which employs fiber-optic intermode interferometers.[2,3] It permits the use of light guides of great length and the determination of disturbances by measuring the displacement of interference bands with considerable relaxation of the requirements for equality between the lengths of the reference and signal interferometers.

In the proposed system (Fig. 1) two multimode fiber-optic light guides with identical parameters and lengths L_1 and L_2 are considered.

To simplify the mathematical expressions, we assume that the light guides are isotropic and lossless, as well as regular, i.e., free of mode conversion.

Then the field for the component at a frequency ω at the inlet end surface of the first light guide can be written in the form

$$E_1(x,y,L_1,\omega)=\sum_{i=1}^{N} c_i E_i(x,y)\cdot \nu(\omega)\exp\{-j\beta_i L_1 - j\varphi_i\}, \tag{1}$$

where N is the number of propagating modes, c_i, β_i, φ_i, and E_i are the amplitude factor, the propagation constant, the initial phase, and the distribution function of the transverse coordinates of the ith mode, and $\upsilon(\omega)$ is the spectral function of the source field:

$$\langle \nu^*(\omega)\nu(\omega')\rangle = G(\omega)\delta(\omega-\omega'). \tag{2}$$

Here $\delta(\omega)$ is the Dirac delta function, and $G(\omega)$ is the normalized spectral power density of the optical source:

$$\int_0^\infty G(\omega)\, d\omega = 1. \tag{3}$$

The latter is related, in turn, to the complex coherence function $\gamma(\tau)$ of the source:

$$\gamma(\omega)=\int_0^\infty G(\omega)e^{-j\omega\tau}d\omega. \tag{4}$$

The mode functions E_i are orthonormalized:

$$\int_S E_i E_k^*\, ds = \begin{cases} 1, & i=k, \\ 0, & i\neq k. \end{cases} \tag{5}$$

The field at the outlet end surface of the second light guide can be written in a similar manner:

$$E_2(x,y,L_2,\omega)=\sum_{n=1}^{N} D_n E_n\cdot \nu(\omega)\ \exp\{-j\cdot\beta_n L_2\}. \tag{6}$$

Next, the coefficients D_n must of defined in terms of the coefficients C_i. For this purpose we equate the fields at the outlet of the first light guide after the spatial filter (we assume that it is infinitely thin) and at the entrance to the second light guide (for $L_2=0$):

$$\sum_{n=1}^{N} D_n E_n\cdot \nu(\omega)=\sum_{i=1}^{N} c_i E_i|_{S_1}\cdot \nu(\omega)\ \exp\{-j\cdot\beta_i L_1 - j\varphi_i\}, \tag{7}$$

where $E_i|_{S_1}$ is the field of the ith mode after filtration in an aperture S_1.

Multiplying through (7) by E_n^* and performing the integration over the entire transverse cross section, with consideration of the orthnormality of the E_n we obtain

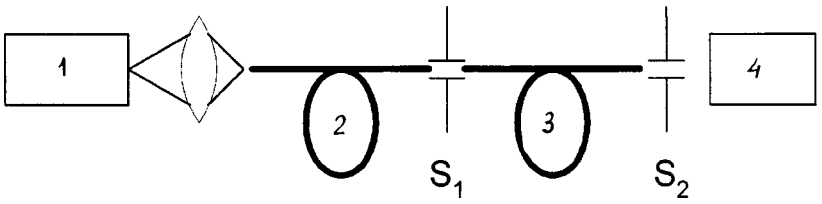

FIG. 1. Structural scheme of intermode interferometers with a low-coherence source: *1* — low-coherence optical source, *2* — reference intermode interferometer, *3*— signal intermode interferometer, S_1, S_2 — spatial filters, *4* — photoreceiver.

$$D_n=\sum_{i=1}^{N} c_i\cdot\exp\{-j\cdot\beta_i L_1-j\varphi_i\}\cdot K_{in}, \tag{8}$$

where we have introduced the notation

$$K_{in}=\int_S E_i|_{S_1}E_n^*\,ds. \tag{9}$$

The coefficients K_{in} can be interpreted as the coupling coefficients of the ith and nth modes in an ''inhomogeneity'' of aperture S_1.

The field at the outlet from the second wavelength can be written in the form

$$E_2(x,y,L_2,\omega)=\sum_{n=1}^{N} E_n(x,y)\cdot\nu(\omega)e^{-j\cdot\beta_n L_2-j\varphi_n}\times\left[\sum_{i=1}^{N} c_i K_{in}\cdot e^{-j\cdot\beta_i L_1-j\varphi_i}\right]. \tag{10}$$

To find the intensity detected by the photoreceiver, we must perform some transformations:

$$I_2(L_2)=\int_0^{\infty}\int_{S_2} E_2(x,y,L_2,\omega)E_2^*\,ds\,d\omega, \tag{11}$$

where S_2 represents the aperture of the second spatial filter.

In order to integrate over the frequency, we must specify the spectrum of the optical source [the function $G(\omega)$] and the frequency dependence of β_i.

We assume that the spectrum of the source is Gaussian:

$$G(\omega)=\frac{1}{\Gamma\sqrt{\pi}}e^{-\frac{(\omega-\omega_0)^2}{\Gamma^2}}, \tag{12}$$

where Γ is the half-width of the line at the level of the maximum value.

For $\beta_i(\omega)$ we utilize the expansion in a Taylor series:

$$\beta_i(\omega)=\beta_i(\omega_0)+(\omega-\omega_0)\frac{1}{V_i}+\ldots, \tag{13}$$

where $V_i=(\delta\beta_i/\delta\omega)^{-1}$ is the group velocityof the ith mode at the central frequency.

Integration over the frequency gives integrals of the form

$$\int_0^{\infty} G(\omega)e^{-j(\beta_i-\beta_k)L}\,d\omega = \cos[\beta_i(\omega_0)-\beta_k(\omega_0)]L\cdot e^{-\frac{L^2\Gamma^2}{4}\cdot[\tau_i(\omega_0)-\tau_k(\omega_0)]^2}, \tag{14}$$

where $\tau_i(\omega_0)$ is the group delay time of the ith mode at the central frequency (ω_0) per unit of light-guide length.

The last exponential multiplier defines the coherence function of the light source $\gamma(\tau)$, and for $L\neq 0$ it represents a small, nearly zero quantity. Therefore, only the terms with exponents containing multipliers of the form (L_1-L_2), which make a nonzero contribution under the condition $L_1\approx L_2$, remain in $I_2(L_2)$.

Under these conditions the expression for I_2 takes the form

$$I_2(L_2)=\sum_{n=1}^{N}\sum_{i=1}^{N}\left(\int_{S_2}E_n^2\,ds\right)c_i^2k_{in}^2 +2\sum_{i\neq k}^{N}\sum_{k}^{N}\left(\int_{S_2}E_iE_k^*\,ds\right)\times c_ic_kk_{ik}^2\cos[\{\beta_i(\omega_0)-\beta_k(\omega_0)\}\times(L_1-L_2)]\cdot e^{-[\tau_i(\omega_0)-\tau_k(\omega_0)]^2\cdot\frac{\Gamma^2}{4}(L_1-L_2)^2}. \tag{15}$$

A simpler expression is obtained for the two-mode regime ($N=2$):

$$I_2(L_2)=c_1^2k_{11}^2\int_{S_2}E_1^2\,ds+c_2k_{21}^2\int_{S_2}E_1^2\,ds+c_1k_{12}^2\int_{S_2}E_2^2\,ds +c_2k_{22}^2\int_{S_2}E_2^2\,ds+2c_1c_2k_{12}^2\left(\int_{S_2}E_1E_2\,ds\right)\times\cos[\{\beta_i(\omega_0)-\beta_k(\omega_0)\}\times(L_1-L_2)]e^{-[\tau_1-\tau_2]^2\cdot\frac{\Gamma^2}{4}(L_1-L_2)^2}. \tag{16}$$

Equation (16) was used to calculate the plot of $I_2(L_1-L_2)/I_0$ shown in Fig. 2 (I_0 is the constant component of the output intensity). The following conditions were imposed in the calculation:

the modes are identically excited: $c_1=c_2$;

the diaphragms S_1 and S_2 close off half of the core of the light guides, leading to the approximate relations

$$k_{11}=k_{22}=k_{12}=k_{21}=0.5;$$

$$\int_{S_{1,2}}E_{1,2}^2\,ds=\int_{S_{1,2}}E_1E_2\,ds=0.5;$$

the difference between the propagation constants ($\beta_1-\beta_2$) and the difference between the group delays ($\tau_1-\tau_2$) were determined for a two-mode graded-index light guide using the formulas[4]

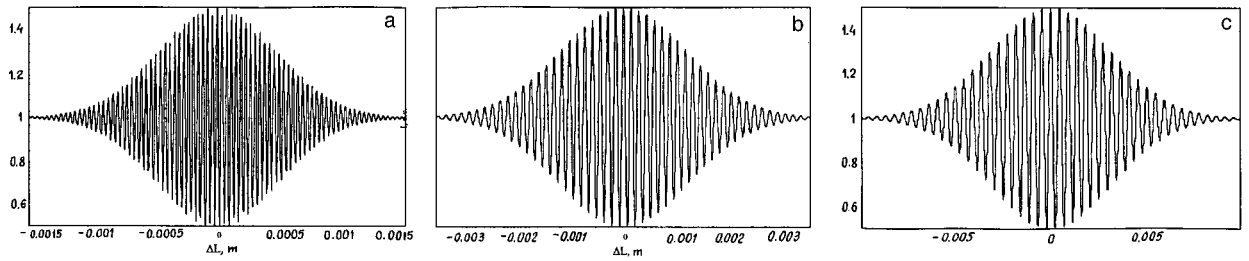

FIG. 2. Dependence of the output intensity on the difference between the lengths of the light guides (L_1-L_2): a — $\lambda=0.85$ μm, $\Delta=2\times10^{-2}$, b — $\lambda=1.3$ μm, $\Delta=8\times10^{-3}$, c — $\lambda=1.55$ μm, $\Delta=3\times10^{-3}$.

$$\beta_1-\beta_2=\frac{2\pi n_1}{\lambda}\cdot\frac{3}{4}\Delta,$$

$$\tau_1-\tau_2=\frac{n_1}{c}\cdot\frac{3}{4}\Delta, \text{ where } \Delta=(n_1-n_2)/n_1.$$

The width Γ of the emission line of the optical source was chosen to correspond to spontaneous emitters of the LED type:[5] $\Gamma\approx8\times10^{13}$ rad/s. We note that $\Gamma\sim2kT$ (k is the Boltzmann constant, and T is the temperature of the light-emitting diode) and does not depend on the working wavelength λ.[5]

As can be seen from the figure, the half-width of the correlation maximum $\Delta L_{0.5}$ depends strongly on Δ (i.e.,on the numerical aperture of the light guide) and reaches almost 1 cm for $\Delta=3\times10^{-3}$. At the same time, variation of the wavelength λ of the light does not influence $\Delta L_{0.5}$, but does determine the number of interference maxima within the correlation peak.

The contrast of the interference oscillations reaches a maximum value of 50% when $L_1-L_2=0$. Problems associated with insufficient contrast of the signal can be solved when multielement and differential reception methods are employed.

[1] K. Weir, K. T. V. Grattan, and A. W. Palmer, Proc. SPIE **2248**, 307 (1994).
[2] M. Spajer, B. Carquille, and H. Maillotte, Opt. Commun. **60**(15), 261 (1986).
[3] P. Hlubina, J. Mod. Opt. **41**, 1001 (1994).
[4] *Fundamentals of Optical Fiber Communications*, M. K. Barnoski (Ed.), Academic Press, New York (1976) [Russ. transl., Sov. Radio, Moscow (1980), 232 pp.].
[5] J. Gowar, *Optical Communication Systems*, Prentice-Hall, Englewood Cliffs, NJ (1984) [Russ. transl., Radio i Svyaz', Moscow (1989), 504 pp.].

Translated by P. Shelnitz

Controlling spatiotemporal chaos in a chain of bistable oscillators

B. P. Bezruchko and M. D. Prokhorov

Saratov Branch of the Institute of Radio Engineering and Electronics, Russian Academy of Sciences
(Submitted November 17, 1998)
Pis'ma Zh. Tekh. Fiz. **25**, 51–57 (June 26, 1999)

The processes in coupled oscillators and their control under bistability conditions are considered. The possibility of stabilizing spatially homogeneous states is demonstrated. © *1999 American Institute of Physics.* [S1063-7850(99)02406-4]

1. The processes in spatially distributed (multidimensional) oscillatory systems are often simulated by oscillators coupled to one another in a chain or an array. Such ensembles have also been used successfully as models of distributed media. A chain of identical dissipative oscillators closed in a ring, in which the oscillators are subjected to cophasal excitation by a periodic external force, can be used to analyze the possibility of controlling chaos. The elements of the chain are nonlinear, capable of undergoing regular and chaotic oscillations, and bistable. The last property means that two different forms of steady motions can take place at fixed values of the parameters. Bistability is typical of nonautonomous oscillatory systems at nonlinear resonance, where hysteresis is observed when the parameters are varied. The coupling between the elements of the chain is symmetric and local (the elements interact only with neighbors), as well as diffusive (dissipative). The problem of controlling spatiotemporal chaos is considered in its classical form, i.e., stabilization of motions in an unstable limit cycle embedded in a chaotic attractor by small changes in a controlling parameter.[1–5] The possibility of stabilizing spatially homogeneous states of an ensemble of bistable elements using an element-by-element regulation procedure[6] and the effectiveness of this approach in the presence of noise are demonstrated.

2. The following discrete model was investigated under the condition that the elements in the chain are identical and their excitation is cophasal:

$$x_{n+1}^m=(1-2k)f(x_n^m)+k[f(x_n^{m+1})+f(x_n^{m-1})], \qquad (1)$$

where x is a dynamic variable, $n=0,1,2,\ldots$ is the discrete time, m is the number of the element in the chain, and k is the coupling coefficient. The boundary conditions are periodic: $x_n^1=x_n^{M+1}$, where M is the number of elements in the chain. The basic chain element $f(x_n^m)$ is a mapping, which reflects the temporal dynamics of an oscillator. We used the multimodal multiparameter mapping

$$x_{n+1}=f(x_n)=x_n\exp[-d/N]\cos\left[\frac{2\pi}{N(1+\beta x_n)}\right]+A, \qquad (2)$$

whose parameters characterize the amplitude (A) and normalized frequency (N) of the external periodic disturbance, the dissipation (d), and the nonlinearity (β). The mapping (2) has both regular and chaotic solutions, qualitatively describes the temporal dynamics of a nonlinear dissipative oscillator and the structure of its bifurcation sequences in the region of the existence of subharmonic oscillations and their evolution to chaos, as well as reflects such nonlinear phenomena as hysteresis, bistability, and multistability.[7,8] The form of a steady multistable oscillatory state is specified by the initial conditions.

At certain values of the parameters the system of equations (1) and (2) goes over to a regime of developed spatiotemporal chaos.[9,10] The attractors corresponding to such states contain a set of saddle periodic orbits, which can be stabilized by a controlling disturbance acting on the parameters of the system.

3. Spatially homogeneous states of the chain were stabilized for two typical cases: for values of the parameters corresponding to an absence of hysteresis and the associated bistability in the elements of the chain and for the presence of bistability in a single element. In accordance with the control procedure used,[6] the controlling disturbance is imposed on the parameter A of each of the coupled oscillators. Thus, the parameter A depends both on the moment in time and on the number of the element m and can be written in the form

$$A=A_n^m=A_0+\tilde{A}_n^m, \qquad (3)$$

where A_0 is the constant component and $\tilde{A}_n^m$ is the variable component. Each of the elements in the chain is successively subjected to the control procedure as its dynamic variable x_n^m comes into the vicinity of the state being stabilized.

The states stabilized in our work are fixed points $\bar{x}$ of the mapping (2). Then, when x_n^m enters a small vicinity of $\bar{x}$, we can write

$$x_{n+1}^m=\bar{x}+\tilde{x}_{n+1}^m, \quad x_n^m=\bar{x}+\tilde{x}_n^m, \qquad (4)$$

where $\tilde{x}_{n+1}^m$ and $\tilde{x}_n^m$ are small perturbations. Substituting (3) and (4) into (1) and linearizing the expression obtained, we obtain the equation for a fixed point

$$\bar{x}=A_0+\bar{x}\exp[-d/N]\cos\left[\frac{2\pi}{N(1+\beta\bar{x}}\right] \qquad (5)$$

and a linearized equation for the perturbations $\tilde{x}_{n+1}^m$, from which we find the value $\tilde{A}_n^m$, at which the perturbation $\tilde{x}_{n+1}^m$ becomes equal to zero:

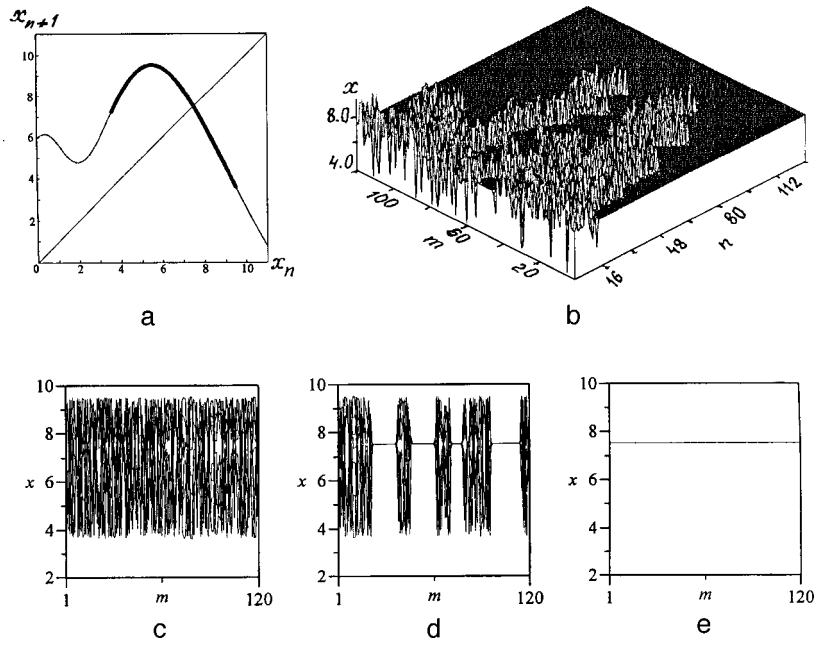

FIG. 1. a — Plot of the mapping (2) for $A=6$, $d=0.2$, $N=0.5$, and $\beta=0.2$ (the chaotic attractor isindicated by the thick line); b — spatiotemporal diagram of the establishment of a homogeneous regime of period 1; c — regime of developed spatiotemporal chaos; d–e — controlled transition to a spatially homogeneous regime of period 1 (e); d — intermediate stage of the transition.

$$\tilde{A}_n^m = -\exp[-d/N]\Bigg\{(1-2k)(x_n^m-\overline{x})\times\Bigg(\overline{x}\sin\Bigg[\frac{2\pi}{N(1+\beta\overline{x})}\Bigg]\frac{2\pi\beta}{N(1+\beta\overline{x})^2}+\cos\Bigg[\frac{2\pi}{N(1+\beta\overline{x})}\Bigg]\Bigg)+k\Bigg(x_n^{m+1}\cos\Bigg[\frac{2\pi}{N(1+\beta x_n^{m+1})}\Bigg]+x_n^{m-v}\cos\Bigg[\frac{2\pi}{N(1+\beta x_n^{m-1})}\Bigg]-2\overline{x}\cos\Bigg[\frac{2\pi}{N(1+\beta\overline{x})}\Bigg]\Bigg)\Bigg\}. \quad (6)$$

The controlling disturbance acts when two conditions are satisfied simultaneously, viz., $|x_n^m-\overline{x}|<\varepsilon$ and

$$\Bigg|k\Bigg\{\Bigg(x_n^{m+1}\cos\Bigg[\frac{2\pi}{N(1+\beta x_n^{m+1})}\Bigg]-\overline{x}\cos\Bigg[\frac{2\pi}{N\Big(1+\beta\overline{x}\Big]}\Bigg)+\Bigg(x_n^{m-1}\cos\Bigg[\frac{2\pi}{N(1+\beta x_n^{m-1})}\Bigg]-\overline{x}\cos\Bigg[\frac{2\pi}{N(1+\beta\overline{x})}\Bigg]\Bigg)\Bigg\}\Bigg|<\varepsilon,$$

i.e., when both terms in (6) are relatively small.

4. Let us first examine the controlled transition from a regime of spatiotemporal chaos to a spatially homogeneous regime for values of the parameters at which the chain elements have a single fixed point of period 1. The plot of the function (2) for such values of the parameters and the chaotic attractor which exists for them are shown in Fig. 1a. The single orbit of period 1 appearing in the chaotic attractor with these values of the parameters (Fig. 1) can be stabilized by a controlling disturbance of the form (6) using the scheme described above. The magnitude of the controlling disturbance decreases with time. We note that the stabilization of regimes with time and in space takes place only when there is weak coupling between the elements of the chain. For example, $k=0.005$ for the plots in Figs. 1c–1e. This is because the algorithm used is based on a method of successive stabilization of the elements in the chain, and the weaker is the coupling between the elements, the longer will the element subjected to the controlling disturbance reside in the vicinity of the unstable state being stabilized and, consequently, the higher will be the probability of cluster formation.

Let us now consider the stabilization of spatially homogeneous states of period 1 for the second typical case, in which the parameters of the system are such that bistability is observed in the elements of the chain and two chaotic attractors coexist in them. The plot of the mapping (2) corresponding to this situation and the forms of the chaotic attractors are presented in Fig. 2a. For the values of the parameters chosen the system has three unstable fixed points, two of which appear in a chaotic attractor. If the initial conditions in all the elements of the chain are assigned in the basin of attraction of one chaotic attractor, the situation is similar to the one considered above for the absence of bistability. Then, each orbit of period 1 appearing in the attractor is stabilized in the chain according to the scheme described. If the initial conditions are such that some of the elements in the chain undergo oscillations in one chaotic attractor and others do so in the other chaotic attractor, a fairly broad window with respect to ε and, therefore, a larger value of the controlling disturbance are required to stabilize any of the regimes of period 1. This condition is fundamental, since regardless of the strength of the coupling between the elements the oscillations of an individual oscillator can occur in the absence of the controlling disturbance in only one of the attractors. Therefore, stabilization of the fixed point appearing in the

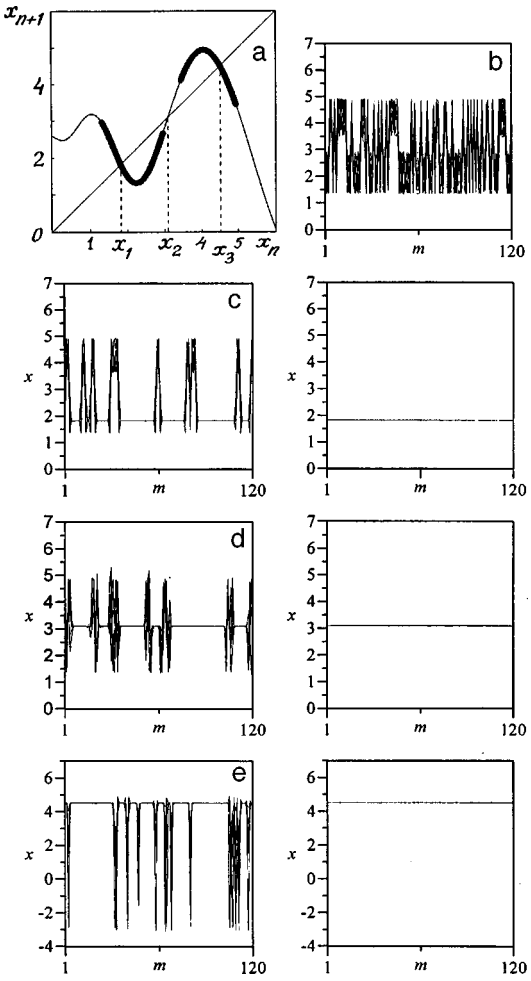

FIG. 2. a — Plot of the mapping (2) for $A=2.6$, $d=0.15$, $N=0.28$, and $\beta=0.2$ (the coexisting chaotic attractors are indicated by the thick lines); b — regime of developed spatiotemporal chaos in a region of bistability; c–e — controlled transition to spatially homogeneous regimes of period 1 (right-hand column) with various oscillation amplitudes: c — $x=x_1$, d — $x=x_2$, e — $x=x_3$ (left-handcolumn — intermediate stage of the transition).

other attractor is possible only for a value of ε greater than the interval with respect to x between the boundaries of the chaotic attractors. The results demonstrating the controlled transition to each of the three possible spatially homogeneous regimes of period 1, including the one which does not belong to either of the attractors, are shown in Fig. 2.

The magnitude of the controlling disturbance needed to bring the chain into a spatially homogeneous regime in the bistability region can be reduced significantly, if random noise is allowed to act on the system. Owing to the presence of noise, switching between the bistable states becomes possible, and the oscillations of an individual oscillator can take place alternately near each chaotic attractor. By supplying noise to the system and simultaneously applying a controlling signal to it, we can try to force the oscillations of all the elements of the chain to move into the vicinity of only one selected chaotic attractor. Thereafter, the noise can be removed, and stabilization of the spatially homogeneous regime of period 1 appearing in that attractor can easily be achieved. For the case depicted in Fig. 2b the application of random noise with a maximum amplitude having an absolute value $\Delta=0.2$ to the system led to fourfold decreases in the absolute values of the controlling signal and the interval ε in which control takes place.

5. The approach used can be applied to the stabilization of spatially homogeneous and spatially periodic regimes with different temporal and spatial periods, as well as to the stabilization of spatial regimes in a two-dimensional array of bistable oscillators.

This work was performed with support from the Russian Fund for Fundamental Research (Grant No. 96-02-16755), as well as the Federal Special-Purpose Program ''Integration'' (Grant No. 696.3).

[1] E. Ott, C. Grebogi, and J. A. Yorke, Phys. Rev. Lett. **64**, 1196 (1990).
[2] H. Gang and Q. Zhilin, Phys. Rev. Lett. **72**, 68 (1994).
[3] D. Auerbach, Phys. Rev. Lett. **72**, 1184 (1994).
[4] R. V. Sole and L. M. Prida, Phys. Lett. A **199**, 65 (1995).
[5] R. O. Grigoriev, M. C. Cross, and H. G. Shuster, Phys. Rev. Lett. **79**, 2795 (1997).
[6] V. V. Astakhov, V. S. Anishchenko, G. I. Strelkova, and A. V. Shabunin, IEEE Trans. Circuits Syst. **42**, 352 (1995).
[7] B. P. Bezruchko, M. D. Prokhorov, and E. P. Seleznev, Chaos Solitons Fractals **5**, 2095 (1995).
[8] B. P. Bezruchko, M. D. Prokhorov, and E. P. Seleznev, in *Lectures on Microwave Electronics and Radiophysics. 10th Winter Workshop* [in Russian], Saratov, (1966), Vol. 2, pp. 35-42.
[9] K. Kaneko, Physica D **34**, 1 (1989).
[10] A. P. Kuznetsov and S. P. Kuznetsov, Izv. Vyssh. Uchebn. Zaved. Radiofiz. **34**, 1079 (1991).

Translated by P. Shelnitz

Radial-slit erosion discharge

S. E. Emelin, A. P. Kovshik, E. I. Ryumtsev, and V. S. Semenov

Scientific-Research Institute of Physics and Scientific-Research Institute of Radiophysics, St. Petersburg State University

(Submitted March 10, 1999)
Pis'ma Zh. Tekh. Fiz. **25**, 58–61 (June 26, 1999)

A new type of erosion discharge, which is distinguished by the stability of the formation and ease of observation of its nonequilibrium plasma in the form of radially propagating, solitary waves, is described. © *1999 American Institute of Physics.* [S1063-7850(99)02506-9]

Among the electric discharges in a stream of gas[1] there are variants which create a highly nonequilibrium plasma in some regimes.[2] Such regimes are distinguished by a reduced gas temperature, instability of the discharge current, and a tendency for the appearance of propagating forms. The appearance of these features is accompanied by an increase in the role of the metastable states and the sequential ionization mechanism.

The plasma of an electric discharge in a stream of a dispersed condensed phase[3] or an erosion capillary discharge[4] has a number of structural features,[5] a low temperature, an elevated electron density, a high electric field intensity, and an increased lifetime after the current is interrupted. In Refs. 6 and 7 these features were associated with the metastability of the energy states of a plasma based on degraded polymers and metals and with the effects of their transport in the metastable material. The features discovered are consistent with the general picture of a dynamic structural transition.[8]

It can be presumed that the nonequilibrium character of the plasma[2] can be enhanced significantly by supplementing the ionization-wave propagation conditions with the conditions characteristic of an erosion discharge.[4] This idea can be realized in a radial-slit erosion discharge, which can be created by placing two walls composed of a readily vaporized dielectric, for example, a polymer,[7] near consumable jackknife electrodes.[2]

The design of the slit discharger (Fig. 1) used to create a transverse discharge is an assembly of two parallel poly(methyl methacrylate) disks *1* with a diameter of 100 mm and a thickness of 25 mm, which are clamped to one another by steel pins *2* and separated by thin ($\sim$1 mm) polyethylene spacers *3* and *4*. The angle between consumable electrodes *5* wasincreased in comparison to Ref. 2 to 300°. Steel electrodes *5* with a diameter of 2 mm were partially insulated by polyethylene tubes *6* and were placed in grooves *7* below the surface of one of the disks *1*. To assign the initial form of the discharge propagation front, the insulating interelectrode spacer *4* has a circular head with a diameter of $\sim$10 mm, and its center coincides with the center of the slit. Ten limiting spacers *3* are positioned in the slit opening with an azimuthal separation of 30°. To improve the stability of the functioning of the discharger at large currents, the errors in the height of the slit must be kept smaller than 5%.

The electrical circuit is similar to the one employed in Ref. 4 and contains a 10-kV accumulator with a capacitance $C=0.8$ mF, a current-limiting resistor with $R=1-500\ \Omega$, and a 30-kV igniting pulsed transformer.

Upon ignition, breakdown occurs between the nearby electrode ends on the surface around the head of the interelectrode spacer, and a discharge in the form of an incomplete disk appears in the radial slit. Then, if the current through the discharger and the active resistance exceeds a certain critical value, which depends on the accumulator voltage, the discharge extends to a shorter distance along the radius, the larger is the current. If the critical value of the current is not exceeded, the discharge propagates rapidly along the radius after a sufficient quantity of vaporized polymer accumulates in the slit (Fig. 2). As a result, The voltage drop on it gradually rises to the total value, and the current decreases to zero with ultimate interruption of the current. When the accumulator voltage is increased sufficiently, the discharge reaches the limiting spacers during propagation and is fixed on them, and the trailing edge of the current pulse is very steep. In the range of currents from a few kiloamperes to tens of amperes the characteristic self-cut-out pulse duration is 0.1–1 ms. Interruption of the current is accompanied by a sound resembling a gunshot. The color of

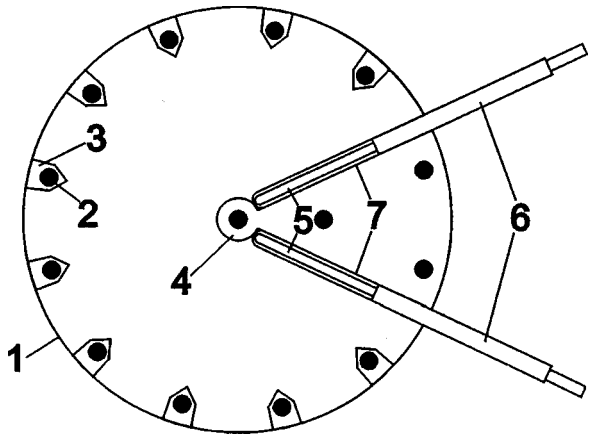

FIG. 1. Design of a slit discharger: *1* — disk, *2* — pins, *3* — limiting spacers, *4* — interelectrode spacer,*5* — electrodes, *6* — insulating tubes, *7* — grooves

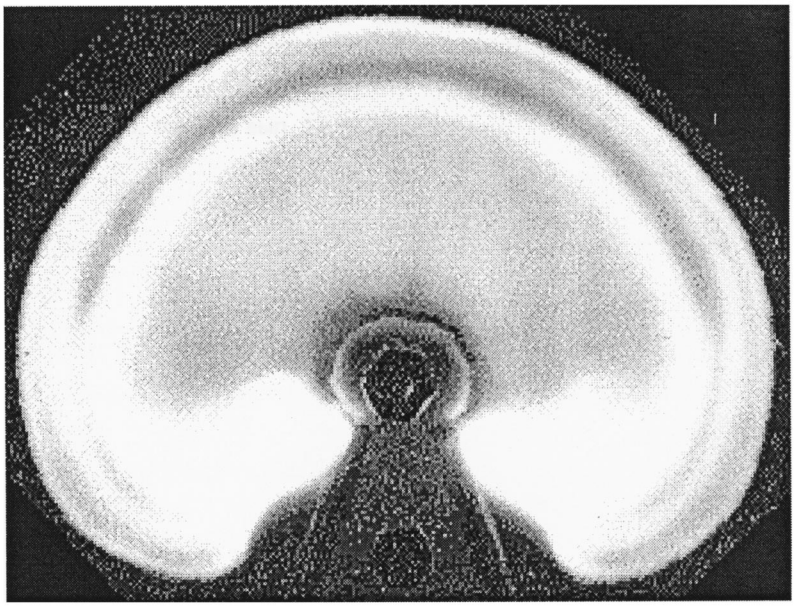

FIG. 2. Integrated image of a radial-slit erosion discharge.

the luminescence of a static discharge is red to the eye, and the color of a moving discharge is blue.

The existence of a discharge in a thin slit is closely related to its interaction with the readily vaporized wall material, which is present in two principal forms: in the form of a wall surface and in the form of an aerosol produced as a result of vaporization of the wall and degradation of the polymer by the discharge. In a low-temperature regime the principal mechanism of energy loss and loading of the discharge is the depletion of charges as a result of their attachment to the wall surface and aerosol particles. The metastability of the bound states of the charges leads to a decrease in their recombination rate. This causes, first, a delay and prolongation of the wall vaporization process, so that it takes place mainly behind the moving discharge, creating a region of increased aerosol density and pressure on the small-radius side. Second, the energy stored in the aerosol which has passed through the discharge facilitates ionization and thereby promotes propagation toward regions of lower pressure, i.e., toward the large-radius side.

Thus, the combination of the nonequilibrium nature of the plasma, the metastability of its energy states, and the propagation of the discharge until interruption of the current is an attribute of the nonstationary regime of a radial-slit aerosol discharge. It can have numerous scientific and technical applications. The formation of a nonequilibrium dense plasma in a transverse discharge, the investigation of its interaction with matter, the creation of shock waves, the development of a high-power electric commutator, etc. can be cited as examples.

[1] Yu. P. Raizer, *Gas Discharge Physics*, 2nd ed., Springer, Berlin–New York (1997) [Russ. original, Nauka, Moscow (1992), 536 pp.].
[2] V. D. Rusanov *et al.*, Dokl. Akad. Nauk **332**, 306(1993) [Phys. Dokl. **38**, 398 (1993)].
[3] V. V. Kudinov *et al.*, *Plasma Deposition of Coatings* [in Russian], Nauka, Moscow (1990), 408 pp.
[4] R. F. Avramenko *et al.*, Zh. Tekh. Fiz. **60**(12), 57 (1990) [Sov. Phys. Tech. Phys. **35**, 1396 (1990)].
[5] S. B. Leonov and M. B. Pankov, Khim. Fiz. **16**, 144 (1997).
[6] S. E. Emelin *et al.*, Pis'ma Zh. Tekh. Fiz. **23**(19),54 (1997) [Tech. Phys. Lett. **23**, 758 (1997)].
[7] S. E. Emelin and A. P. Kovshik *et al*. in *Reports to the 5th Inter. Conference: Current Problems in the Electrophysics and Electrohydrodynamics of Fluids* [in Russian], St. Petersburg, (1998), pp. 103–106.
[8] G. E. Skvortsov, Pis'ma Zh. Tekh. Fiz. **25**, 81 (1999) [Tech. Phys. Lett. **25**, 35 (1999)].

Translated by P. Shelnitz

Self-reproduction of multimode Hermite–Gaussian beams

S. N. Khonina, V. V. Kotlyar, and V. A. Soĭfer

Institute of Image-Processing Systems, Russian Academy of Sciences, Samara
(Submitted November 25, 1998)
Pis'ma Zh. Tekh. Fiz. **25**, 62–69 (June 26, 1999)

The condition for the self-reproduction of multimode Hermite–Gaussian beams is obtained and analyzed. Partial self-reproduction planes are also considered. A numerical example is presented. © *1999 American Institute of Physics.* [S1063-7850(99)02606-3]

When several types of coherent light fields propagate in a homogeneous space, self-reproduction, i.e., repetition of the intensity distribution in a transverse cross section, can be observed. The repetition or self-reproduction of light fields with a transverse periodic structure is called the Talbot effect.[1] A general condition which must be satisfied by light fields having longitudinal periodicity was derived by Montgomery.[2]

Single-mode light beams are examples of self-reproducing beams with a period equal to zero. They include Bessel modes,[3] as well as similarity-conserving Hermite–Gaussian and Laguerre–Gaussian modes.[4] The conditions for the rotation of modal light beams, which are also examples of fields with longitudinal periodicity (to within scale), were obtained in Refs. 5–8. The condition under which the intensity distribution of a multimode Laguerre–Gaussian beam will self-reproduce to within scale at several distances was obtained in Ref. 9.

In this paper a similar condition is derived for multimode Hermite–Gaussian (HG) beams. Self-reproduction is demonstrated for concrete modal beams using numerical simulation.

Let us consider a multimode HG beam propagating in free space. The complex amplitude of such a beam can be written in the form

$$E(x,y,z)=\sum_{m,n=0}^{N} C_{mn}\Psi_{mn}(x,y,z), \tag{1}$$

where

$$\Psi_{mn}(x,y,z)=\frac{\omega_0}{\omega(z)}\exp\left[i(m+n+1)\,\eta(z)-\frac{ik(x^2+y^2)}{2R(z)}-\frac{x^2+y^2}{\omega^2(z)}\right]H_m\left(\frac{\sqrt{2}x}{\omega(z)}\right)H_n\left(\frac{\sqrt{2}y}{\omega(z)}\right), \tag{2}$$

$$\omega(z)=\omega_0\left(1+\frac{z^2}{z_0^2}\right)^{1/2}, \quad R(z)=z\left(1+\frac{z_0^2}{z^2}\right),$$

$$\eta(z)=\arctan\left(\frac{z}{z_0}\right), \tag{3}$$

z is the longitudinal Cartesian coordinate, x and y are the transverse coordinates, ω_0 is the radius of the Gaussian beam at $z=0$, $\omega(z)$ is the radius of the Gaussian beam at any z, $R(z)$ is the radius of curvature of the Gaussian beam, $z_0=k\omega_0^2/2$ is the Rayleigh parameter of the Gaussian beam, $H_m(x)$ is a Hermite polynomial, k is the wave number, and C_{mn} are complex coefficients.

The expression for the light intensity in a transverse cross section of an HG beam has the form

$$I(x,y,z)=\frac{\omega_0^2}{\omega^2(z)}\exp\left[-2\frac{x^2+y^2}{\omega^2(z)}\right]\times\left\{\sum_{m,n=0}^{N}|C_{mn}|^2H_m^2\left(\frac{\sqrt{2}x}{\omega(z)}\right)H_n^2\left(\frac{\sqrt{2}y}{\omega(z)}\right)+\sum_{m,n}^{N}\sum_{m',n'}^{N}|C_{mn}C_{m'n'}|H_m\left(\frac{\sqrt{2}x}{\omega(z)}\right)\times H_{m'}\left(\frac{\sqrt{2}x}{\omega(z)}\right)H_n\left(\frac{\sqrt{2}y}{\omega(z)}\right)H_{n'}\left(\frac{\sqrt{2}y}{\omega(z)}\right)\cos\Phi_{m'n'}^{mn}\right\}, \tag{4}$$

where

$$\Phi_{m'n'}^{mn}=\arg C_{mn}-\arg C_{m'n'}+[(m-m')+(n-n')]\,\eta(z). \tag{5}$$

In order for the intensity distribution (4) at the distance z_1 to be repeated to within scale at the distance z_2, the functions (5) in each term in Eq. (4) must satisfy the condition

$$\Phi_{m'n'}^{mn}(z_2)=\Phi_{m'n'}^{mn}(z_1)+2\pi l, \quad l=1,2,3,\ldots. \tag{6}$$

Substituting the function (5) into Eq. (6), we obtain an expression for the distance z_2:

$$z_2=\frac{z_1+z_0\tan\left(\frac{2\pi l}{p}\right)}{1-\frac{z_1}{z_0}\tan\left(\frac{2\pi l}{p}\right)}, \tag{7}$$

where

$$p=(m-m')+(n-n'). \tag{8}$$

The presence of the parameter l in formula (7) shows that for a pair of modes with the numbers (m,n) and

(m',n') there can be several distances at which the transverse intensity distribution of their sum recorded at a certain z_1 will be repeated.

Let us consider the example of a pair of modes with $p=20$ and find the distances at which the intensity distribution recorded for $z_1=0$ is repeated:

$$z_{l,p}=z_0\tan\left(\frac{2\pi l}{p}\right), \quad l=1,2,3,\ldots. \tag{9}$$

In this case we obtain five repetitions with increasing period, one of which appears at infinity:

$$z_{1,20}=0.3249\cdot z_0, \quad z_{2,20}=0.7265\cdot z_0, \quad z_{3,20}=1.3764\cdot z_0,$$

$$z_{4,20}=3.0777\cdot z_0, \quad z_{5,20}=\infty.$$

It is understood that all the variations appearing in the interval $[0,z_{1,p}]$ will be repeated in the subsequent periods $[z_{l,p},z_{l+1,p}]$ with a rate that slows with increasing l.

Let us next consider methods for choosing the mode numbers for a self-reproducing beam of the type (1) containing more than two terms.

If a pair of modes with the numbers (m,n) and (m',n') and $p_0=(m-m')+(n-n')$ is chosen, the addition of modes with the same phase velocities, i.e., with the numbers (m'',n'') which are such that

$$m''+n''=m+n \quad \text{or} \quad m''+n''=m'+n', \tag{10}$$

permits the formation of a beam which self-reproduces at the same distances (7) as the original pair of modes. This is because the additional modes will give only two values: $p'=p_0$ and $p'=0$. When $p=0$, the dependence on z in (5) vanishes, as in the case of a stable beam. An example of such a multimode beam with $p_0=20$ is provided by the combination of seven modes $(0,1)+(1,0)+(10,11)+(11,10)+(9,12)+(8,13)+(0,20)$.

Another degree of freedom for choosing the numbers of the additional modes appears, if we consider the following repetition condition for (7):

$$z_{l,p}=z_{l',p'}. \tag{11}$$

For example, if a pair of modes with the numbers (m,n) and (m',n') and $p_0=(m-m')+(n-n')$ is chosen, then for repetition at the same distances the difference between the numbers of the additional modes must be

$$p=|p_0|q, \quad q=0,1,2,\ldots, \tag{12}$$

and the numbers of the additional modes are found from the following relation:

$$m''+n''=m+n+|p_0|q, \quad q=0,1,2,\ldots. \tag{13}$$

For example, if a $(1,1)+(5,5)$ beam repeats its initial (at $z_1=0$) transverse intensity distribution at the distance [see (9)]

$$z_{1,8}=z_0\tan\left(\frac{\pi}{4}\right)=z_0,$$

a $(1,1)+(0,2)+(5,5)+(4,6)+(9,9)+(8,10)$ beam will repeat at the same distance:

$$z_{1,8}=z_{2,16}=z_0.$$

TABLE I. Positions of the self-reproduction points.

Value of $\lvert p_0\rvert$	Self-reproduction points z_{l,p_0}
$\lvert p_0\rvert<4$	None
$\lvert p_0\rvert=4$	$z_{1,p_0}=\infty$
$4<\lvert p_0\rvert<8$	$z_0<z_{1,p_0}<\infty$
$\lvert p_0\rvert=8$	$z_{1,p_0}=z_0$, $z_{2,p_0}=\infty$
$8<\lvert p_0\rvert<12$	$0<z_{1,p_0}<z_0<z_{2,p_0}<\infty$
$\lvert p_0\rvert=12$ [a]	$0<z_{1,p_0}<z_0<z_{2,p_0}<\infty$, $z_{3,p_0}=\infty$

[a]The pattern subsequently repeats with a multiple increase in the number of self-reproduction points.

It is interesting that the positions of the repetitions of the initial (at $z_1=0$) intensity distribution relative to z_0 can be predicted as a function of the value of $|p_0|$ in (13) (see Table I).

If the distances z_1 and z_2 in (7) are assigned, the numbers of the HG modes which must appear in the beam in order for it to have similar transverse intensity distributions at these distances will satisfy the condition

$$\frac{2\pi l}{p}=\arctan\left[\frac{z_0(z_2-z_1)}{z_2z_1+z_0^2}\right], \quad |p|>4l. \tag{14}$$

It follows from Eq. (14) that the distances z_1 and z_2 cannot be assigned arbitrarily.

Apart from the distances for self-reproduction of the intensity distribution at z_1, the distances of the ''fractional'' period (4) can be interesting. Here we can draw an analogy to ''fractional'' Talbot period for lattices.[11] The distances for one qth of the self-reproduction period will be described in the following manner ($z_1=0$):

$$z_{l,p}^q=z_0\tan\left(\frac{2\pi}{q}\cdot\frac{l}{p}\right), \quad l=1,2,3,\ldots. \tag{15}$$

The value $q=2$ corresponds to a ''half-period.'' In this case for odd $l=2s+1$ and $s=0,1,2,\ldots$ instead of the addition of the cross terms in (4) we have subtraction: $\cos(x\pm\pi l)=-\cos(x)$, which can be defined as quasicontrasting. A similar situation is observed at half of the Talbot period for lattices,[11] where the shift of the original lattice image appears as contrasting.

Figure 1 presents the results of the numerical simulation for a three-mode $(1,1)+(5,5)+(9,9)$ HG beam. All the modes appear in the composition of the beam with equal weights. The following parameters were used: the arrays measured 512×512 pixels, the region for variation of the arguments was $x,y\in[-0.5\ \text{mm},0.5\ \text{mm}]$, the wavelength was $\lambda=0.63\ \mu$m, the radius of Gaussian beam was $\omega_0=0.1$ mm, and the Rayleigh parameter was $z_0=k\omega_0^2/2=49.63$ mm.

Using the expression (15), we can obtain the following distances for self-reproduction (for $q=2$ and even l) and quasicontrasting (for $q=2$ and odd l) ($z_1=0$):

$$z_{2,8}^2=z_0\tan\left(\pi\frac{1}{4}\right)=z_0\approx49.63, \quad z_{4,8}^2=z_0\tan\left(\pi\frac{1}{2}\right)=\infty,$$

$$z_{1,8}^2=z_0\tan\left(\pi\frac{1}{8}\right)\approx20.71, \quad z_{3,8}^2=z_0\tan\left(\pi\frac{3}{8}\right)\approx120.71.$$

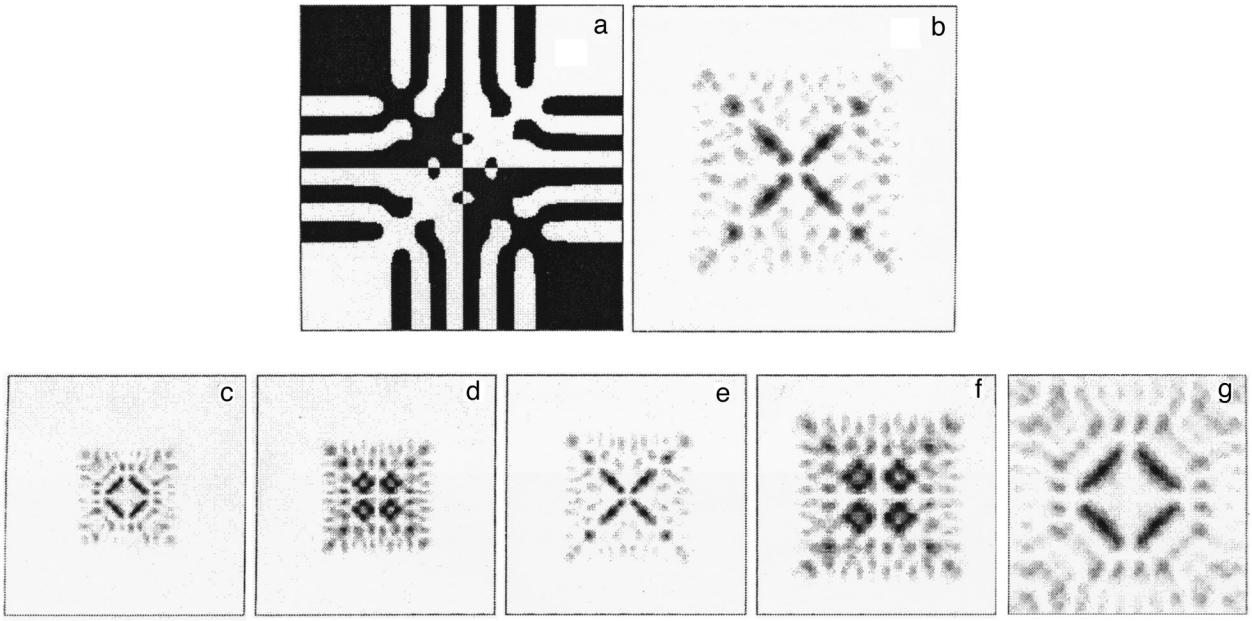

FIG. 1. Binary phase (a) (white — 0, black — π), intensity (b) in the $z=0$ plane, and intensity distributions in the following planes: $z=20.71$ mm (c), $z=33.16$ mm (d), $z=49.63$ mm (e), $z=74.27$ mm (f), $z=120.71$ mm (g).

For a quarter-period we have the following distances (for $q=4$, $l=2s+1$, $s=0,1,2\ldots$):

$$z_{1,8}^4=z_0\tan\left(\frac{\pi}{2}\cdot\frac{1}{8}\right)\approx 9.87,\quad z_{3,8}^4=z_0\tan\left(\frac{\pi}{2}\cdot\frac{3}{8}\right)\approx 33.16,$$

$$z_{5,8}^4=z_0\tan\left(\frac{\pi}{2}\cdot\frac{5}{8}\right)\approx 74.27,\quad z_{7,8}^4=z_0\tan\left(\frac{\pi}{2}\cdot\frac{7}{8}\right)\approx 249.51.$$

Figure 1a shows a binary phase (white — 0, black — π), and Fig. 1b shows the intensity in the $z=0$ plane (the size corresponds to the size of the aperture, 1 mm). The ensuing figures show the intensity distributions at various distances: $z_{1,8}^2=20.71$ mm (c), $z_{3,8}^4=33.16$ mm (d), $z_{2,8}^2=z_0=49.63$ mm (e), $z_{5,8}^4=74.27$ mm (f), and $z_{3,8}^2=120.71$ mm (g) (the size of each frameis equal to 1.6 mm).

It is seen from Fig. 1 that the intensity patterns at $z_1=0$ (b) and $z=z_0$ (e) coincide to within scale. The same agreement is observed for $z=20.71$ mm (c) and $z=120.71$ mm (g). Their repetition can also be predicted using formula (7).

For a quarter-period the similarity of the intensity distribution patterns in Figs. 1d and 1f is possible only if $\arg C_{mn}-\arg C_{m'n'}=0$ (this condition was satisfied in our case).

Thus, the condition [formulas (7) and (8)] which must be imposed on the mode number of an HG beam in order for self-reproduction to occur has been obtained in this work. The condition for partial self-reproduction has also been considered. A numerical example for a three-mode HG beam with two self-reproduction planes has been presented.

This work was carried out with support from the Russian Fund for Fundamental Research (Grants Nos. 98-01-00894 and 99-01-00430).

[1] H. F. Talbot, Philos. Mag. **9**, 401 (1936).
[2] W. D. Montgomery, J. Opt. Soc. Am. **57**, 772 (1967).
[3] J. Durnin, J. Opt. Soc. Am. A **4**, 651 (1987).
[4] A. Yariv, *Introduction to Optical Electronics*, 2nd ed., Holt, Rinehart and Winston, New York (1976) [Russ. transl., Vysshaya Shkola, Moscow (1983)].
[5] E. Abramochkin and V. Volostnikov, Opt. Commun. **102**, 336 (1993).
[6] Y. V. Schechner, R. Piestun, and J. Shamir, Phys. Rev. E **54**, 50 (1996).
[7] V. V. Kotlyar, V. A. Soifer, and S. N. Khonina, J. Mod. Opt. **44**, 1409 (1997).
[8] V. V. Kotlyar, V. A. Soĭfer, and S. N. Khonina, Pis'ma Zh. Tekh. Fiz. **23**(17), 1 (1997) [Tech. Phys. Lett. **23**, 657 (1997)].
[9] R. Piestun, Y. V. Schechner, and J. Shamir, Opt. Lett. **22**, 200 (1997).
[10] V. V. Kotlyar, S. N. Khonina, and V. A. Soifer, Optik (Stuttgart) **108**, 20 (1998).
[11] J. Westerholm, J. Turunen, and J. Huttunen, J. Opt. Soc. Am. A **11**, 1283 (1994).

Translated by P. Shelnitz

Nonlinear zero-range potential model for the scattering of sound intensity by a Helmholtz resonator

O. S. Pershenko and I. Yu. Popov

St. Petersburg State Institute of Fine Mechanics and Optics (Technical University)
(Submitted October 22, 1998)
Pis'ma Zh. Tekh. Fiz. **25**, 70–75 (June 26, 1999)

The scattering of an intense sound wave by a Helmholtz resonator can be described by a nonlinear (to take into account the hydrodynamic effects in the resonator throat) zero-range potential model. The case in which the wave is linear everywhere except in the resonator throat is considered. A comparison with the results of other models is made. © *1999 American Institute of Physics.* [S1063-7850(99)02706-8]

The problem of the Helmholtz resonator, i.e., a resonator with a small orifice, was first posed by Rayleigh at the beginning of this century.[1] Many approaches to the problem have been developed since then. The leading-order terms of the asymptotic expansion (in the small orifice diameter ε) have been obtained (on a rigorous mathematical basis) for solving the scattering problem (see, for example, the review in Ref. 2). Since the problem is complicated, various models have been proposed for solving it. We shall proceed within the so-called zero-width-slit model, which is based on operator extension theory[5] and is similar to the zero-range potential method in quantum mechanics.[3,4] The model problem is considerably simpler than the fundamental problem; nevertheless, it yields the leading-order terms of the asymptotic expansion under consideration. In addition, it permits the use of the powerful machinery of operator theory. Therefore, there should be interest in expanding the area of application of the model, which is the purpose of the present work. We note that all the approaches mentioned above were developed for a linear Helmholtz resonator. However, it is known that this resonator is not linear in the case of intense sound.[6–8] This calls for taking into account the hydrodynamic effects in describing oscillations in the resonator throat. Several models of such a resonator were proposed in Refs. 9–11. In this paper we present another model, which can be called the nonlinear zero-range potential model. A comparison with the results in Ref. 9 will be made. The proposed model is a natural generalization of the corresponding linear model; therefore, we shall first briefly describe the linear variant.[12]

Let Ω^{in} be a closed bounded region in $\mathbf{R}^3$, and let Ω^{ex} be a half-plane, so that $\Omega^{\text{ex}} \cap \Omega^{\text{in}} = r_0$. We consider the Laplace operator $-\Delta = -(\Delta^{\text{in}} \oplus \Delta^{\text{ex}})$ with the Neumann boundary condition. We narrow it to a set of smooth functions that vanish at the point r_0. The closure of the operator obtained will be symmetric with the defect indices (2, 2). Its self-conjugate extensions also provide a model which interests us. Without describing all the possible extensions here (see Refs. 5 and 12), we shall consider only the one which is most natural from the physical standpoint, whose domain of definition consists of all the elements of the form

$$u = u_0^{\text{in,ex}} + \xi_+^{\text{in,ex}} G_+^{\text{in,ex}}(r, r_0, k_0), \quad r \in \Omega^{\text{in,ex}},$$

where u_0^{in} (u_0^{ex}) is from the Sobolev space $H_2(\Omega^{\text{in}})$ ($H_2(\Omega^{\text{ex}})$), $G_+^{\text{in,ex}}$ is the Green's function for the region $\Omega_+^{\text{in,ex}}$, and k_0^2 is some negative number (a regular value of the operator). In addition, the following relation holds:

$$\xi_+^{\text{in}} = \xi_+^{\text{ex}}, \quad \xi_-^{\text{in}} = -\xi_-^{\text{ex}}, \tag{1}$$

where $\xi_-^{\text{in,ex}} = u_0^{\text{in,ex}}(r_0)$. For the extended (model) operator under consideration, the solution of the problem of the scattering of a plane wave has the form:[5,12]

$$\psi(r, \nu, k) = \begin{cases} \psi_0(r, \nu, k) + b_{\text{ex}} G^{\text{ex}}(r, r_0, k), & r \in \Omega^{\text{ex}}, \\ b_{\text{in}} G^{\text{in}}(r, r_0, k), & r \in \Omega^{\text{in}}, \end{cases} \tag{2}$$

where

$$\psi_0(r, \nu, k) = e^{ik(r,\nu)} + e^{ik(r,\nu^*)}$$

is the sum of the incident and reflected plane waves (in the absence of an orifice), $k\nu$ ($k\nu^*$) is the wave vector of the incident (reflected) wave, and

$$b_{\text{in}} = b_{\text{ex}} = \frac{\psi_0(r_0, \nu, k)}{D_{\text{in}} + D_{\text{ex}}},$$

$$D_{\text{in,ex}} = (G^{\text{in,ex}}(r, r_0, k) - G^{\text{in,ex}}(r, r_0, k_0))\big|_{r=r_0}.$$

We note that

$$D_{\text{in}} = (\lambda - \lambda_0) \sum_{n=1}^{\infty} \frac{|\Psi_n(r_0)|^2}{(\lambda_n - \lambda)(\lambda_n - \lambda_0)},$$

where $\lambda_0 = k_0^2$, λ_n is an eigenvalue of theoperator $-\Delta^{\text{in}}$, and Ψ_n is the corresponding eigenfunction.

It was shown in the preceding studies that the model parameter λ_0 can be chosen such that the model solution would give the leading-order term of the asymptote in the slit width ε for the corresponding solution of the ''real'' problem with an orifice of diameter ε (Ref. 12).

Let us now move on to the nonlinear variant of the model. We note that in the analysis of the scattering of intense sound by a Helmholtz resonator we have nonlinear effects only in the resonator throat.[9] Therefore, we introduce only one nonlinearity, viz., the one corresponding to a ''non-

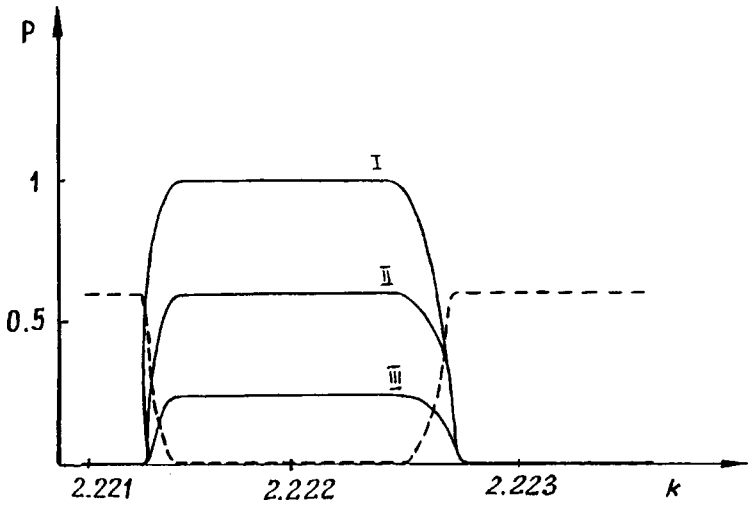

FIG. 1. Dependence of the absorption coefficient on k in the vicinity of the resonance value 2.22144 (in dimensionless form). Values of the parameters: *I* — $k_0=7$, $\alpha=1$, $\beta=1$; *II* — $k_0=7$, $\alpha=1.3$, $\beta=1$; *III* — $k_0=7$, $\alpha=2$, $\beta=1$. The dashed curve corresponds to the second (''nonphysical'') solution with the following values of the parameters: $k_0=7$, $\alpha=1.3$, $\beta=1$.

linear'' point orifice, into the model. The starting point of the construction is the same as before, but we construct the extension itself differently. We choose the nonlinear coupling $\xi_{\pm}^{\text{in}}$, $\xi_{\pm}^{\text{ex}}$ (i.e., the extended operator will be nonlinear). In the linear case one of the selection rules for the extensions was the requirement that they be self-conjugate. In the nonlinear case this requirement no longer exits. Taking into account that the resonator must be linear for sound waves of small amplitude, we can examine a quadratic nonlinearity, which is a perturbation of the linear self-conjugate extension (1):

$$\xi_{+}^{\text{in}}=\xi_{+}^{\text{ex}}+\alpha(\xi_{+}^{\text{ex}})^2,$$
$$\xi_{-}^{\text{in}}=-\xi_{-}^{\text{ex}}+\beta(\xi_{-}^{\text{ex}})^2, \tag{3}$$

where α and β are constants. We obtain the solution for the scattering of a plane wave in the form

$$\psi(r,\nu,k)=\begin{cases}\psi_0(r,\nu,k)+a_{\text{ex}}G^{\text{ex}}(r,r_0,k), & r\in\Omega^{\text{ex}},\\ a_{\text{in}}G^{\text{in}}(r,r_0,k), & r\in\Omega^{\text{in}},\end{cases} \tag{4}$$

where $\psi_0(r,\nu,k)$ is the same as in the linear case. Taking into account (3), we find

$$a_{\text{in}}=a_{\text{ex}}+a_{\text{ex}}^2,$$

$$(a_{\text{ex}}+a_{\text{ex}}^2)D_{\text{in}}=-a_{\text{ex}}D_{\text{ex}}-\psi_0+\beta(a_{\text{ex}}^2D_{\text{ex}}^2+2\psi_0D_{\text{ex}}a_{\text{ex}}+\psi_0^2),$$

where $\psi_0=\psi_0(r_0,\nu,k)$. Therefore,

$$a_{\text{ex}}=\frac{-A^{\pm}\sqrt{A^2-4\psi_0(\beta\psi_0-1)(\beta D_{\text{ex}}^2-\alpha D_{\text{in}})}}{2(\beta d_{\text{ex}}^2-\alpha D_{\text{in}})}, \tag{5}$$

$$A=2\beta\psi_0D_{\text{ex}}-D_{\text{ex}}-D_{\text{in}}.$$

Thus, we have two solutions. If

$$(2\beta\psi_0D_{\text{ex}}-D_{\text{ex}}-D_{\text{in}})^2=4\psi_0(\beta\psi_0-1)(\beta D_{\text{ex}}^2-\alpha D_{\text{in}}),$$

they coincide. The corresponding value k is a bifurcation point. The coefficient P ($P=|a_{\text{ex}}/\phi_0|^2$) characterizes the absorption of power. Let k_1^2 be the first positive eigenvalue of $-\Delta_{\text{in}}$ (which corresponds to the first resonant frequency). When the minus sign is chosen in (5), we have $P=1$ at the resonance frequency. In addition, as the nonlinearity is diminished, this solution tends to the solution obtained in the linear case, i.e., this choice of sign corresponds to the common physical situation. The other solution gives $P=1(\alpha^2\psi_0^2)$ at resonance. Generally speaking, it is a non-

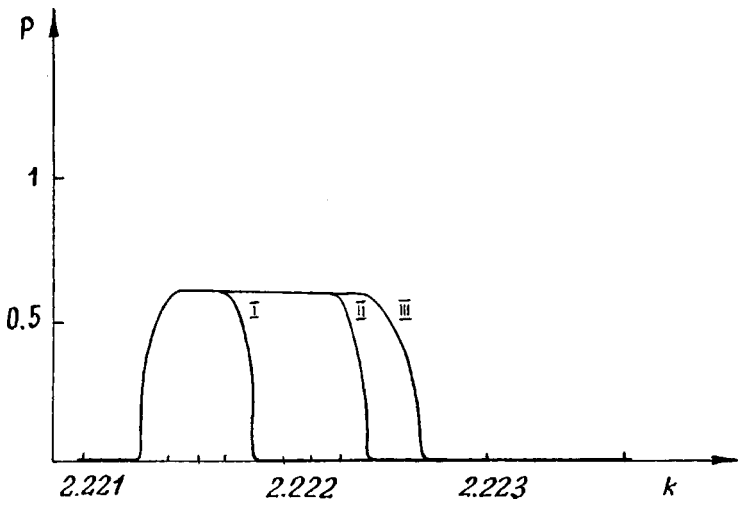

FIG. 2. Dependence of the absorption coefficient on k in the vicinity of the resonance value 2.22144 (in dimensionless form). Values of the parameters: *I* — $k_0=3$, $\alpha=1.3$, $\beta=1$; *II* — $k_0=6$, $\alpha=1.3$, $\beta=1$; *III* — $k_0=7$, $\alpha=1.3$, $\beta=1$.

physical solution. However, it may correspond to another physical situation, viz., the presence of an acoustically active medium (for example, bubbles in a liquid) in the orifice zone. The behavior of this solution is similar to what was described in papers on an ''acoustic laser.''[13]

For the solution of the first type with a suitable choice of parameters, the behavior of $K(k)$ near the resonance frequency is similar to the dependence described in Ref. 9. The choice of parameters was empirical both in our model and in the model in Ref. 9. One difference is that our model generally gives sharper resonance peaks. The dependences on the model parameters α and k_0 are shown in Figs. 1 and 2, respectively. The influence of β is similar to the influence of α, but is weaker. The parameter α characterizes the strength of the nonlinearity, and k_0 is related to the width of the orifice.

This work was partially supported by a grant from the Russian Fund for Fundamental Research (RFBR).

[1] O. M. Lord Rayleigh, Proc. R. Soc. London, Ser. A, No. 638, 265 (1916).
[2] R. R. Gadyl'shin, Usp. Mat. Nauk **52**(1), 3 (1997).
[3] B. S. Pavlov, Usp. Mat. Nauk **42**(6), 99 (1987).
[4] Yu. N. Demkov and V.N. Ostrovskii, *Zero-Range Potentials and Their Applications in Atomic Physics*, Plenum Press, New York (1988) [Russ. original, Izd. LGU, Leningrad (1975), 240 pp.].
[5] I. Yu. Popov, J. Math. Phys. **33**, 3794 (1992).
[6] U. Ingard, J. Acoust. Soc. Am. **25**, 1037 (1953).
[7] G. B. Thurston, L. E. Hargrove, and B. D. Cook, J. Acoust. Soc. Am. **29**, 992 (1957).
[8] A. Cummings, J. Acoust. Soc. Am. **79**, 942 (1986).
[9] O. V. Rudenko and K. L. Khirnykh, Akust. Zh. **36**, 527 (1990) [Sov. Phys. Acoust. **36**, 293 (1990)].
[10] A. A Zaikin and O. V. Rudenko, Akust. Zh. **42**, 378 (1996) [Acoust. Phys. **42**, 329 (1996)].
[11] J. J. Keller and E. Zauner, Z. Angew. Math. Phys. **46**, 297 (1995).
[12] I. Yu. Popov, Mat. Sb. **181**, 1366 (1990).
[13] S. T. Zavtrak, Phys. Rev. E **51**, 2480 (1995).

Translated by P. Shelnitz

Investigation of mechanical stresses in strained solids on models of conducting polymer composites

Dzh. N. Aneli, D. I. Gventsadze, and M. M. Bolotashvili

Institute of Mechanical Engineering, Georgian Academy of Sciences, Tbilisi
(Submitted December 21, 1998)
Pis'ma Zh. Tekh. Fiz. **25**, 76–82 (June 26, 1999)

A method for measuring mechanical stresses in the bulk of machine parts, which simplifies the known methods and does not require significant destruction of the test sample, is proposed.
 [S1063-7850(99)02806-2]

The evaluation of the stressed state of structural elements and machine parts reduces mainly to the determination of strains upon loading.[1] Theoretical calculations are usually performed using methods based on the resistance of materials and the theory of elasticity. However, in practice, especially in the case of machine parts of complex design, difficulties of a mathematical character arise when the external loading scheme is fairly complex, and the solution is either excessively cumbersome or totally impossible due to a lack of a series of experimental data. In these cases, the theoretical methods have been successfully supplemented by experimental methods, which permit faster and more accurate achievement of the goal than do analytical methods, as well as testing of the accuracy and correctness of the approximate calculation methods. Among the experimental calculation methods, the photoelasticity or polarization-optical method is most often employed.[2] This method is based on the ability of certain transparent materials to alter their optical properties as a result of their deformation upon loading. Despite the perfection and universality of this method, it is characterized by some inaccuracies. They are associated chiefly with the special features of the mechanical properties of polymer materials. For example, in accordance with the photoelasticity method, to study the stressed state in the bulk of the transparent polymeric solid serving as the model object, the material must be cut into thin plates after removal of the load, interference patterns in the form of bands of isoclines and isochromes are obtained from each of them by passing monochromatic light through them, and a far from simple analysis is performed, in which equations with many parameters must be solved. It is assumed here that the strains and, accordingly, the stresses in the sample remain unchanged after removal of the load. This assumption is supported by the fact that a stress is ''frozen'' in a material loaded at elevated temperatures (below the melting point) and then cooled under the load to room temperature. However, it should be taken into account that errors in the estimation of the magnitude and distribution of the mechanical stresses clearly arise because the test sample is sawed into thin plates. The mechanical stresses appearing when the material is sawed are superimposed on the stresses being investigated. The resultant error will be greater, the thinner are the plates cut. Therefore, the photoelasticity method is classified as a destructive testing method, which lowers the value of this method to a definite extent.

For the purpose of simplifying the procedure for measuring mechanical stresses in the bulk of machine parts of various design and improving the correctness of the measurements, we propose a method for measuring mechanical stresses in the bulk of model solids essentially without significant destruction of the test sample. The method is based on the dependence of the resistivity of a conducting polymer composite on applied mechanical load.

Let us examine the proposed method in greater detail. It is known[3] that the resistivity of a polymer composite consisting of a polymer binder and a conducting filler is limited by the mean distance between filler particles, i.e., the resistivity of a composite increases with increasing values of this distance and decreases with decreasing values. According to experimental data, in a region of elastic strains the logarithm of the resistivity of a material increases linearly in response to a tensile strain and decreases in response to a compressive strain.[4] Such a dependence is stipulated by the conduction mechanism of conducting composites.[5] In practice, situations frequently arise in which individual portions of machine parts are subjected to nonuniform loading (for example, the teeth of gear drives). Loading anisotropy causes strain anisotropy and, accordingly, stresses in the bulk of the sample. Also, if the sample is made from a conducting composite, then in the case under discussion the microstructure at individual sites will depend on the local strain, and, accordingly, the resistivity at individual sites will, in turn, reflect their stressed state. Thus, the distribution of the stresses in the bulk of a sample can be obtained by measuring local resistivities.

The method just described of estimating the distribution of the stresses in the bulk of a sample of a solid underlies the experimental procedure.

The material needed, i.e., a conducting polymer composite based on a polymer binder with high physicomechanical characteristics and a conducting filler (carbon black, graphite, metal powders), is first obtained using a technology which ensures that the samples have the required mechanical and conducting properties. Greater attention is focused on obtaining a material with a highly uniform distribution of the

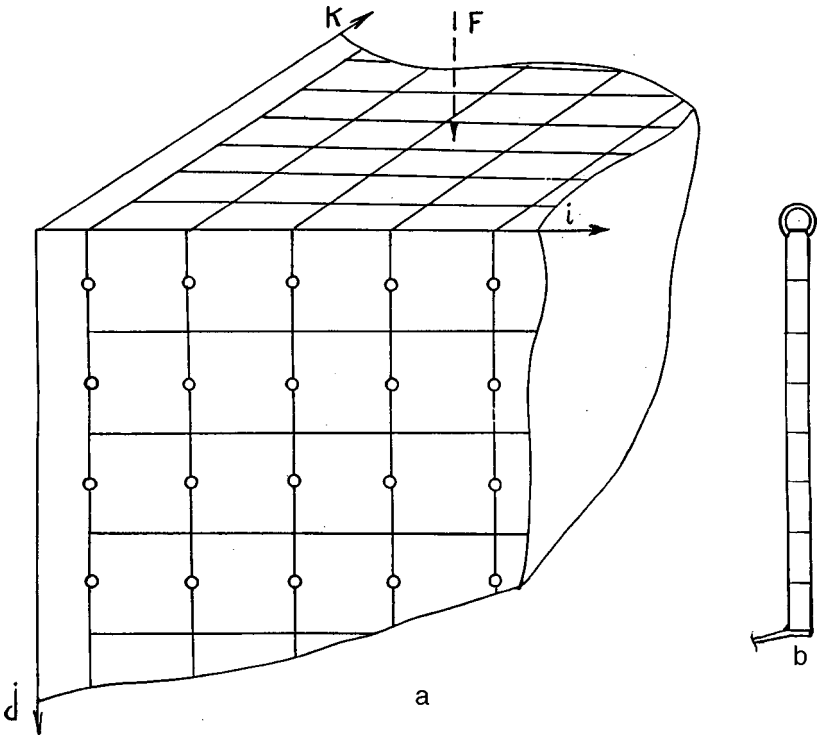

FIG. 1. Model sample of a conducting polymer composite with a grid drawn on it, as well as holes (a) and probe electrodes (b).

filler particles in the polymer matrix. The shape and dimensions of the model sample are chosen in accordance with the problem posed. In our experiment we used a sample in the form of a parallelepiped measuring $80\times50\times30$ (mm). A square grid is drawn on two adjacent planes of the parallelepiped, as shown in Fig. 1a. As the density of the grid points is increased, the possibility of increasing the accuracy of the measurement of the distribution of stresses in the bulk upon loading increases, if the grid is drawn between neighboring grid points.

The next step in preparing the sample is to drill thin (1–1.5 mm) holes in the sample perpendicular to one of the faces of the parallelepiped with the grid between grid points (Fig. 1a). Metal (steel) probe electrodes are inserted through the holes to measure the resistivity between neighboring holes at a definite depth in the sample. The probes are coated with an insulating lacquer except at their ends (Fig. 1b). A contact loop made from a thin $(0.2-0.3$ mm) bronze wire is soldered to one end of the probe, and a current lead is soldered to the other end.

An experiment to measure local stresses is carried out in the following manner: probe electrodes are inserted into neighboring holes to the same depth. The flexible loops on the electrode tips with a diameter slightly larger than the holes ensure reliable contact with the body of the sample at the depth selected. The other ends of the electrodes are connected to a sensitive tensometer (we used an ISD-3 static strain meter). In the present case the role of the strain sensor (strain resistor) is performed by the resistance of an elementary cube with an edge equal to the side of an elementary square in the grid. The local resistivities R_{ijk} are measured as the probes are displaced by equal distances into the interior of the sample, and in order to avoid the edge effect, the measurements of the local resistivity should be performed between holes at distances no less than 4.5 mm from the edge of the sample. Measurements are performed both before and after the load is applied. The local resistivity of each elementary cube must be measured before the load is applied, because the preparation of a conducting composite with exceptionally high electrical uniformity (for example, with respect to the resistivity) is essentially impossible (i.e., the original values of the resistivity of these cubes differ from one another by a certain amount), and the changes in resistivity in response to small strains can lie within the spread of the original values of the resistivity of the elementary cubes. However, things are simplified by the fact that the plots of the logarithm of the resistivity R_{ijk} versus ε_{ijk} recorded for any elementary cube are linear, have the same slope relative to the rectangular coordinate axes (Fig. 2), and are satisfactorily described by the equation

$$l_n R_{ijk}=I_n R_{ijk}\varepsilon_{ijk}, \tag{1}$$

where R_{ijk} is the initial value of the resistivity of the respective elementary cube.

We shall utilize the familiar dependence of the mechanical stresses of a solid on elastic strain (Hooke's law), which, in our case, takes the form

$$\sigma_{ijk}=E\varepsilon_{ijk}, \tag{2}$$

where E is the relaxational Young's modulus of the test material.

By combining Eqs. (1) and (2) we obtain formula (3), which can be used to calculate the local stresses:

$$\sigma_{ijk}=E\ln(R^0_{ijk}/R_{ijk}). \tag{3}$$

The application of the proposed method for calculating local stresses by measuring the local resistivities of a model is illustrated below in the example of elastic deformation of

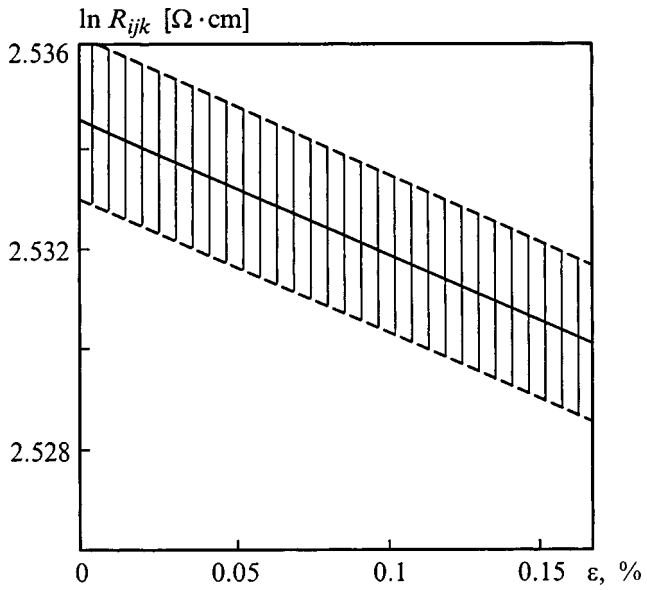

FIG. 2. Dependence of the resistivity of elementary cubes on strain for a composite based on polycarbonate with a graphite filler (30 wt. %). The hatched area shows the dispersion of this dependence due to the variability of the original resistivity values of the individual elementary cubes.

a sample in the form of a parallelepiped obtained from a composite material based on polycarbonate and graphite.

This material was obtained in the following manner. A mixture of Diflon polycarbonate with GM-G graphite (30 wt. %) was heated in a mold under a pressure of 10 MPa at 250 °C for 10 min and then cooled without pressure to 200 °C and finally to room temperature under a pressure of 100 MPa (Refs. 5 and 6).

The numerical values of the local stresses calculated from formula (3) in the case of a parallelepiped measuring $80\times50\times30$ (mm) under a 0.1-MPa load are listed in Table I.

TABLE I. Values of local stresses (in MPa) for layer $k=4$ for the coordinates 4,0,4 of the point ($d=3$ mm) of application of the load ($F=1$ kgf).

	i							
j	0.11	0.26	0.34	0.92	0.90	0.34	0.25	0.08
	0.13	0.27	0.42	0.56	0.53	0.39	0.25	0.10
	0.12	0.18	0.38	0.35	0.32	0.36	0.17	0.08
	0.10	0.15	0.16	0.24	0.21	0.16	0.15	0.07
	0.06	0.12	0.14	0.15	0.13	0.14	0.11	0.04
	0.02	0.06	0.09	0.08	0.06	0.07	0.04	0.01
	0.01	0.02	0.04	0.04	0.03	0.03	0.02	0.01
	0.00	0.00	0.01	0.02	0.02	0.02	0.01	0.00

As expected, in accordance with the data in the table, the largest mechanical stresses in the model appear in regions near the point of application of the load and gradually decrease with increasing distance from that point in the radial directions. The character of the distribution of the local stresses in the loaded model agrees well with the data obtained by other methods.[1,2]

It should be noted that the present method enables us to study the kinetics of the variation of local stresses after unloading, as well as under the conditions of loading in a dynamic regime.

[1] G. Ya. Pochtovik and A. B. Zlochevskiĭ, *Methods and Means for Testing Structural Elements* [in Russian], Vysshaya Shkola, Moscow (1973).
[2] A. J. Durelli and W. F. Riley, *Introduction to Photomechanics*, Prentice-Hall, Englewood Cliffs, NJ (1965) [Russ. transl., Mir, Moscow (1970)].
[3] V. E. Gul' and L. Z. Shenfil', *Conducting Polymer Composites* [in Russian], Khimiya, Moscow (1984).
[4] Dzh. N. Aneli and G. M. Topchishvili, Kauch. Rezina, No. 9, 10 (1987).
[5] J. N. Aneli, L. M. Khananasvili, and G. E. Zaikov, *Structuring and Conductivity of Polymer Composites*, Nova Science Publishers, New York (1998).
[6] Dzh. R. Aneli, D. I. Gventsadze, I. G. Mamasakhlisov, and I. P. Kaverkin, Plast. Massy, No. 3, 31 (1983).

Translated by P. Shelnitz

Generation of a homogeneous plasma in a glow discharge with a hollow anode and a wide-aperture hollow cathode

N. V. Gavrilov, D. R. Emlin, and S. P. Nikulin

General Physics Institute, Russian Academy of Sciences, Moscow; Institute of Electrophysics, Russian Academy of Sciences, Ekaterinburg
(Submitted December 23, 1998)
Pis'ma Zh. Tekh. Fiz. **25**, 83–88 (June 26, 1999)

The principles for designing electrode systems for sources of ion beams of large cross section on the basis of a glow discharge are considered, and a system with combined magnetic and electrostatic confinement of the fast electrons in a wide-aperture hollow cathode and the generation of an ion-emitting plasma in the anode cavity is proposed. It is shown that the system investigated generates a plasma with a nearly homogeneous distribution of the ion emission current density at low gas pressures and can be effectively used to obtain ion beams over a broad range of energies. © *1999 American Institute of Physics.* [S1063-7850(99)02906-7]

The employment of a glow discharge in sources of broad ion beams[1,2] provides for increased reliability and simple operation of the sources, as well as a considerable increase in the duration of the generation of beams of chemically active gases, in comparison to hot-cathode systems.[3] The main problems arising in such applications of glow discharges include the need to reduce the admission of gas to the level of hot-cathode ion sources in order to maintain the breakdown strength of the accelerating gap, as well as to lower the pressure in the working chamber in order to optimize the ion-treatment conditions. A solution to this problem has been achieved using a hollow-cathode glow discharge of specific design.[4] However, the radial distribution of the plasma density in such systems is inhomogeneous, making it difficult to obtain a beam of large cross section. In addition, the achievement of a high current density in low-energy ion beams is hampered by the negative influence of the near-cathode layer, which is characterized by a considerable (up to 1 kV) potential drop and a large thickness, comparable to the diameter of the openings in the emitter.

A significant improvement in the character of the distribution and the formation of a homogeneous plasma in a considerable portion of the cathode cavity can be ensured when weak magnetic fields are applied.[5] Sources of broad high-energy (tens of kiloelectron volts) ion beams with a hollow cathode in a magnetic field have been developed and effectively employed, but the formation of a high-current low-energy beam requires a decrease in the potential difference $\Delta\varphi$ between the emitterand the plasma,[6,7] which hampers ignition of the discharge. A decrease in $\Delta\varphi$ can be achieved in another plasma-emission system,[7] in which the ion-emitting plasma is created in an anode cavity communicating with the cathode cavity through a small aperture. However, in such a system the radial distribution of the plasma density is highly inhomogeneous, making it difficult to form a broad beam. For this reason, a study of the possibility of obtaining a dense homogeneous plasma in hollow-anode systems is of great interest.

An inhomogeneous distribution appears in the anode cavity, because electrons enter it through a narrow near-axial opening. The diameter of the exit aperture of a hollow cathode can be increased without destroying the stability of the discharge, if there is magnetic confinement of the fast electrons along with electrostatic confinement in the hollow cathode. The efficiency of such a combined technique of electron confinement, which is often employed in cylindrical magnetron sputtering systems,[8] is attributed to the fact that the application of a longitudinal magnetic field sharply reduces the velocity of the fast particles starting from the cylindrical cathode surface toward the exit aperture. As a result, the residence time of the fast electrons in the cavity increases, and they manage to effect a number of ionization acts in it sufficient for sustaining the discharge.

The electrode system used in the experiment is shown in Fig. 1. The dimensions of hollow cathode 1 were varied during the experiments, and the diameter of its exit aperture d had values of 1, 5, and 8 cm. The diameters of hollow anode 2 and the cathode were equal to 13 cm, and their lengths were equal to 6–8 cm. Emitter 3 had a cathodic or floating potential. The flux of gas (argon) admitted into the

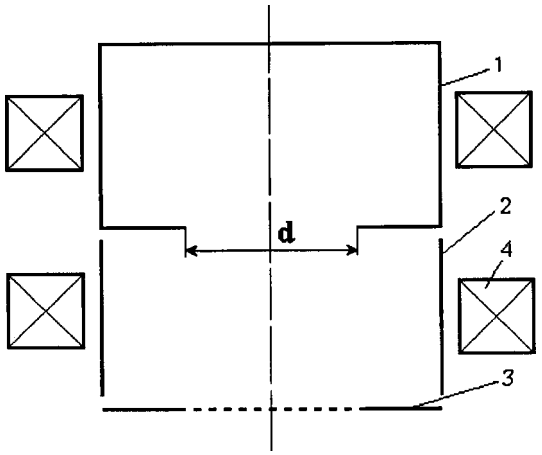

FIG. 1. Electrode system of a glow-discharge plasma-emission system.

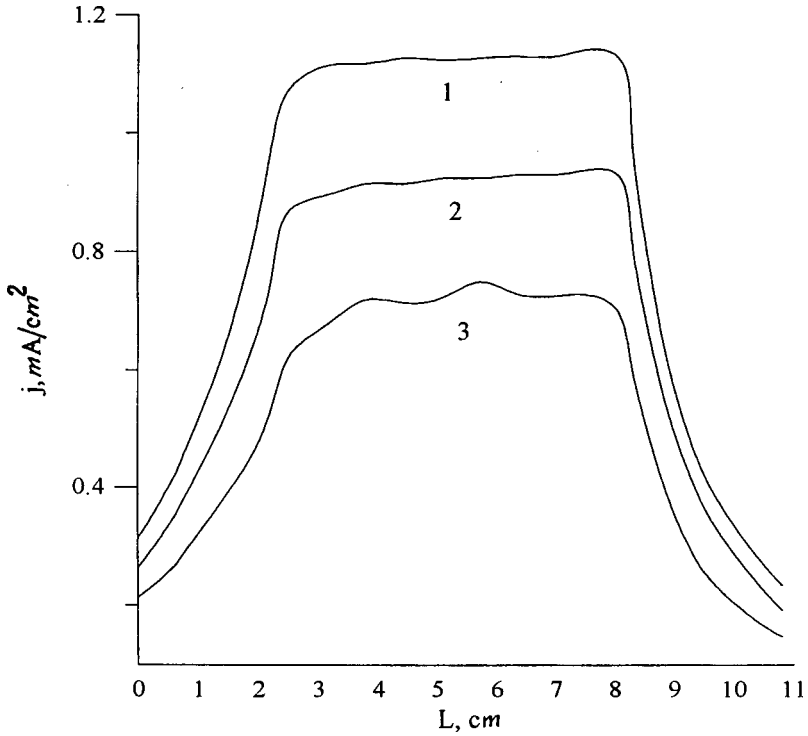

FIG. 2. Radial profiles of the ion emission current density for discharge currents equal to 0.8 (1), 0.6 (2), and 0.4 A (3). The magnetic induction was $B=10^{-2}$ T.

cathode cavity was 10 cm^3/min, and the pressure in the vacuum chamber did not exceed 10^{-2} Pa. The magnetic field ($B=0-30$ mT) was induced by two coils 4. The discharge current was varied in the range 0.1–1 A.

The results of the experiments show that the character of the radial distribution of the plasma density varies significantly as d is increased. When $d=1$ cm, the radial profile of the saturation ion current density from the plasma in the plane of electrode 3 has a sharp maximum on the axis of the system, and when the aperture diameter is increased, a plateau, whose width is close to d, appears on the distribution. Figure 2 shows the profiles obtained using a cathode with $d=8$ cm for various values of the discharge current with a floating potential on electrode 3. As B is increased, the ion emission current density j increases, and the discharge ignition voltage U decreases (Fig. 3) with a resultant significant decrease in the cost of an ion in the beam. The character of the distribution does not vary significantly, whereas in other plasma-emission systems an increase in B generally leads to a drastic increase in the inhomogeneity of the plasma, and in systems of the inverted magnetron type it leads to a decrease in the emission current.

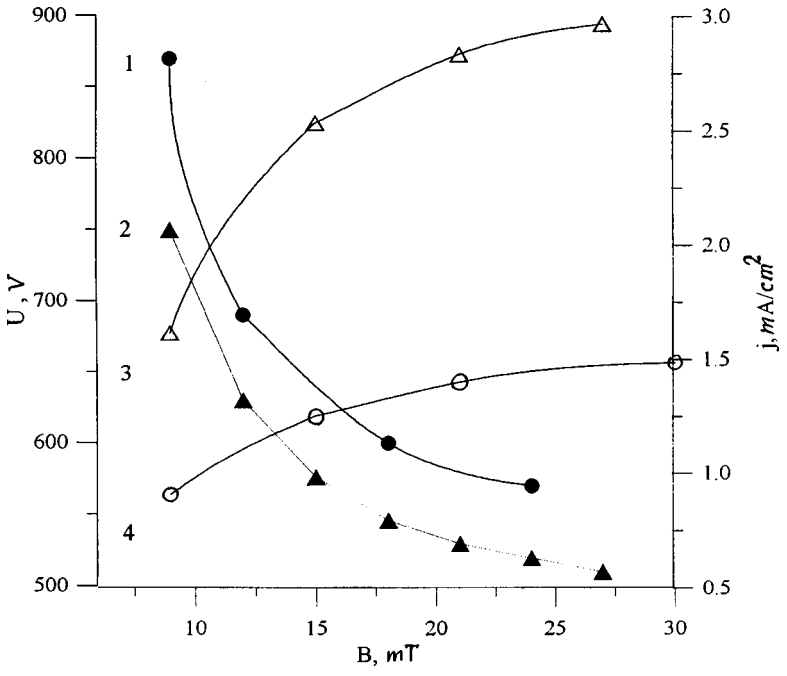

FIG. 3. Dependence of the discharge ignition voltage (1, 2) and the ion emission current density (3, 4)on magnetic field induction with cathodic (2, 3) and floating (1, 4) potentials on the emitter. The discharge current was 0.7 A.

In the experiments with an inhomogeneous magnetic field (in this case a different current was passed through the coils) it was found that the ignition voltage is influenced predominantly by the field in the cathode region and that the efficiency and character of the distribution of the ion emission current is influenced by the field strength in the anode region of the discharge, creating a possibility for independent optimization of the conditions for sustaining the discharge and ion emission from the plasma.

When electrode *3* was under a cathodic potential, ignition of the discharge was facilitated significantly, and the cutoff pressure and ignition voltage of the discharge decreased (Fig. 3). The emission current density was 1.5–2 times higher than with a floating potential, but the character of its radial distribution remained unchanged. However, the results of the calculations and experiments show that the cathode layer hinders achievement of the optimal form of the emission plasma surface when a low-energy beam ($\sim$1 keV) is generated. This leads to considerable losses of ions on the screen electrode and calls for an increase in the field intensity in the accelerating gap. Therefore, it is preferable to use systems with a cathodic potential on the emitter, which have a higher energy efficiency, in sources of ions of higher energies (tens of kiloelectron volts). As for sources of low-energy ion beams, as has already been noted above, here it is better to use systems with a floating potential on the emitter, for which $\Delta\varphi$ is small.

The results obtained in the present work make it possible to obtain ion beams of large cross section over a broad range of energies and provide for significant improvement in the parameters of glow-discharge sources of gas ions.

This work was carried out within an NIS-IPP project according to contracts Nos. 774233 and 857153 with the Brookhaven National Laboratory, U.S.A.

[1] N. V. Gavrilov, G. A. Mesyats, and G. V. Radkovskii *et al.*, Surf. Coat. Technol. **96**, 81 (1997).
[2] A. B. Vizir', E. M. Oks, P. M. Shchanin, and G. Yu. Yushkov, Zh. Tekh. Fiz. **67**(6), 27 (1997) [Tech. Phys. **42**, 611 (1997)].
[3] H. R. Kaufman, J. J. Cuomo, and J. M. E. Harper, J. Vac. Sci. Technol. **21**, 725 (1982).
[4] A. S. Metel', Zh. Tekh. Fiz. **54**, 241 (1984) [Sov. Phys. Tech. Phys. **29**, 141 (1984)].
[5] N. V. Gavrilov, G. A. Mesyats, S. P. Nikulin *et al.*, J. Vac. Sci. Technol. A **14**, 1050 (1996).
[6] S. P. Nikulin, in *Proceedings of the 17th ISDEIV*, Berkeley, CA (1996), Vol. 2, pp. 659–661.
[7] V. V. Bersenev, N. V. Gavrilov, and G. V. Radkovskiĭ, in *Abstracts of Reports to the 4th All-Russian Conference on Modifying the Properties of Structural Materials by Beams of Charged Particles* [in Russian], Tomsk (1996), pp. 66–68.
[8] J. A. Thornton and A. S. Penfold, *Cylindrical Magnetron Sputtering*, Academic Press, New York (1978), 113 pp.

Translated by P. Shelnitz

Evaluation of the mechanical properties of multicomponent materials of stochastic structure

V. N. Leĭtsin and Yu. N. Sidorenko

Tomsk State University
(Submitted December 2, 1997)
Pis'ma Zh. Tekh. Fiz. **25**, 89–94 (June 26, 1999)

A new algorithm for simulating the mechanical behavior of a composite material of stochastic structure is proposed. The use of a model material, which is composed according to the parameters of the shape, size, and orientation distributions of the components in the real composite, as a standard medium is proposed. A procedure is proposed for determining the bounds of the interval of microvolume sizes in the model material which ensure that it is locally representative. The possibility of preliminarily estimating these bounds from the parameters of the distributions of geometric characteristics of the microvolumes, which does not require the solution of a sequence of inverse problems, is demonstrated. [S1063-7850(99)03006-2]

One of the basic techniques in the mechanics of composites is utilization of the concept of an effective medium. The properties of the effective medium are specified as the properties of a standard material, which is most often either a reduced (homogeneous) material or a material with a regular structure.[1] In the former case there is no possibility for obtaining information on the distribution of microstresses, and in the latter case it is impossible to take into account the concentration inhomogeneity and the chaotic character of the reinforcement, which are characteristic of many real composites.

The use of a model material composed of a matrix randomly filled by discrete inclusions as a standard material is proposed. A geometric model of the structure is constructed using Neumann's method from the parameters of the shape, size, and orientation distributions of the inclusions. This permits direct simulation of the features of the structure and, as a consequence, the mechanical response of real composites. The macroscopic properties of the model material are assumed to be effective and are determined by the methods of stochastic mechanics from the distributions of local properties.[2] The local mechanical properties are determined by the response of microvolumes of the model material to external loading. The problem of selecting the sizes of these microvolumes which ensure that they are representative in the local sense is considered. A three-phase model of a composite[3] is used to determine the parameters of the mechanical response of a microvolume in a uniform field of external disturbances.

The problem posed is solved in a planar formulation by finite element analysis as applied to estimating the elastic properties of a fiber-filled composite when it is loaded transversely to the direction of the fibers. Figure 1a presents the model structure of such a material and its characteristics. The relative characteristic size of the fragment of the structure of the model material investigated is $D/B=50$, and the volume fraction of the inclusions equals 0.46. The dependence of the variance σ^2 of the volume ratio between the components on L/B for a random sampling of fragments is presented in Fig. 1b. It is seen that there is a characteristic range of microvolume sizes ($L_0<L/B<L_1$), which corresponds to the region of the abrupt change in the character of $\sigma^2(L/B)$. The elastic properties are characterized by the following values of the Lamé constants: $\lambda_i/\lambda_m=6$ and $\mu_i/\mu_m=6.6$ (the subscripts m and i label the matrix and the inclusions). The calculation scheme is shown in Fig. 1c. The conditions of ideal mechanical contact are satisfied on the interfaces between the components. The loading conditions simulate the case of uniaxial macroscopic stretching.

Figures 2a and 2b present the results of the application of the proposed scheme for determining elastic properties to two randomly selected points in the model material in cases of stretching in mutually orthogonal directions. The relative size L/B of each fragment of the structure was varied in the range $1.5\ldots7.5$. The volume ratio between the components C was also determined for each fragment. A correlation is observed between the changes in the level of variations of the volume ratio of the components in the material and the levels of variation of the local effective elastic properties as the size L/B of the model fragment is varied. The results presented show that there are considerable differences between the mechanical responses of microvolumes corresponding to different points in the model structure, which do not vanish as the size of the fragments increases. This supports the claim in Ref. 1 that a faithful estimation of the effective mechanical properties of a material requires the use of information on the distribution functions of its local properties.

The dependence of the statistical parameters of the distributions of the elastic properties and the volume ratios of the components in microvolumes of the model composite on their sizes in a randomly formed sampling was investigated. Figures 2c and 2d present plots of the distribution densities ofthe relative elastic moduli E/E_m and G/G_m for samplings

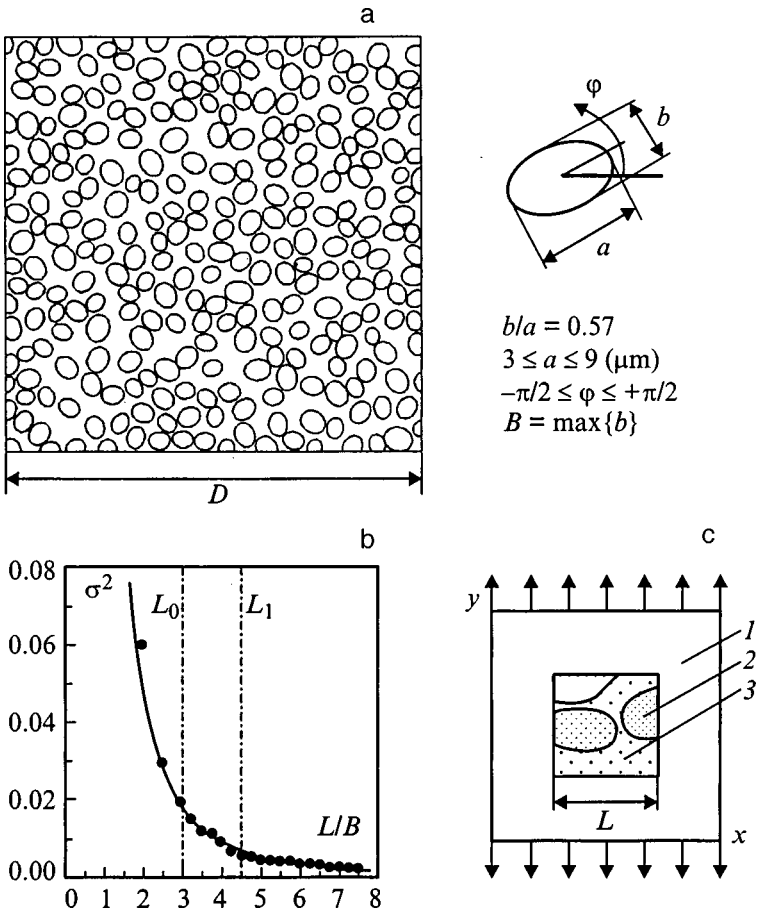

FIG. 1. Parameters of the structure of a model material and calculation scheme: a — structure of the model material; b — dependence of the variance σ^2 of the volume ratio between the components of the model material on the size of the fragments; c — calculation scheme for determining the effective parameters of a microvolume of the model material (*1* — effective medium, *2* — inclusions, *3* — matrix).

of microvolumes of various sizes (E and G are the effective Young's modulus and shear modulus of a microvolume, and E_m and G_m are the corresponding moduli of the matrix). A three-parameter Weibull distribution was used to approximate the distribution of the effective elastic moduli of the microvolumes. The size of the samplings formed ($N=300$) makes it possible to reliably estimate the parameters of the distributions for an assigned significance level.

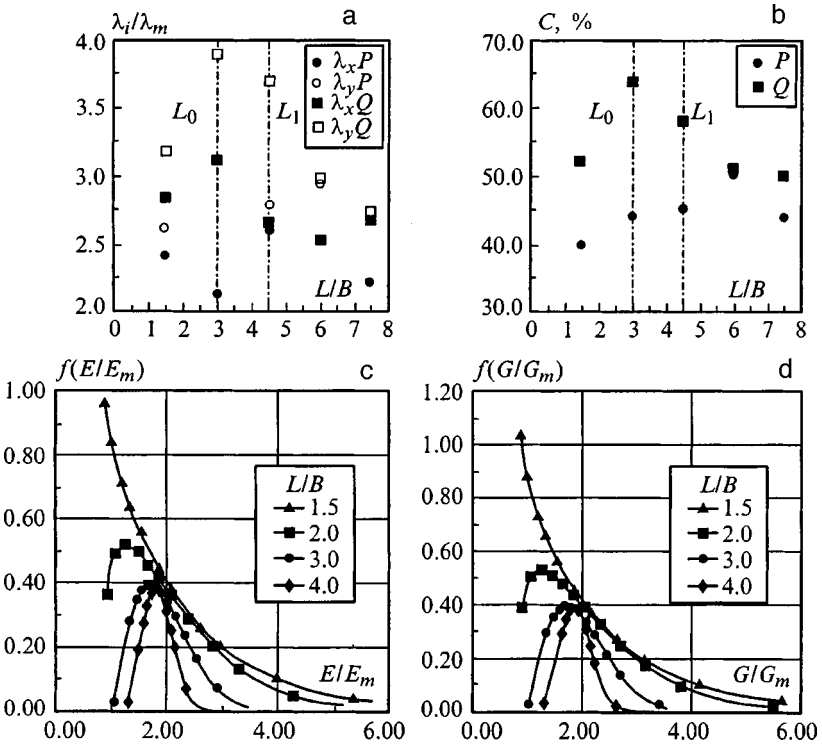

FIG. 2. Calculation results: a — dependence of the relative elastic characteristics λ_i $(i=x,y)$ for two points (P, Q) of the model material on the microvolume size for stretching in orthogonal directions; b — volume ratio between the components of the material (C) for two points (P, Q) within a microvolume as a function of its size; c — distribution densities of the relative Young's modulus for samplings of microvolumes of various size; d — distribution densities of the relative shear modulus for samplings of microvolumes of various size.

The plots of the distribution densities of the relative elastic moduli in Figs. 2c and 2d, like the data in Figs. 2a and 2b, attest to the existence of a strong dependenceof the result of the numerical estimation of the mechanical properties of a microvolume on its size. The plots presented allow us to state that the results obtained for different values of the relative size of the microvolumes become similar at $L/B \geqslant 3.0$. This bound of the similarity region of the plots of the distribution density of the relative elastic moduli ($L/B \geqslant 3.0$) falls in the same size interval (L_0, L_1) as does the region of the abrupt change in the character of $\sigma^2(L/B)$ (Fig. 1b).

The results obtained allow us to draw the following conclusions.

1. The use of a model material with a stochastic structure as a standard permits estimation of the mechanical response of multicomponent materials with consideration of the characteristic features of the real structure, as well as the local irregularities in the loading and straining parameters caused by them.[4]

2. There is a minimum microvolume size L_0 in the model structure, which permits allowance for the influence of its elements on the local mechanical response of the composite. There is a maximum microvolume size L_1, at which locality of the estimates of the properties is lost. Microvolumes whose size falls in the interval (L_0, L_1) can be regarded as locally representative. The results of the averaging of the mechanical responses of microvolumes of the sizes indicated determine the local effective parameters of state of the composite material.

3. A preliminary estimate of the bounds of the interval of microvolume sizes in a composite which ensure that it is locally representative can be obtained from the results of an analysis of the dependence of the variance of the volume ratio between the components on a characteristic geometric parameter of the structure (L/B).

[1] B. E. Pobedrya, Mekh. Kompozit. Mater., No. 6, 729 (1996).
[2] V. A. Lomakin, *Statistical Problems in the Mechanics of Deformable Solids* [in Russian], Nauka, Moscow (1970), 139 pp.
[3] R. M. Christensen, *Mechanics of Composite Materials*, Wiley, New York (1979) [Russ. transl., Mir, Moscow (1982), 334 pp.].
[4] Yu. G. Korotkikh and I. A. Volkov, in *Applied Strength and Plasticity Problems: An Interinstitute Collection* [in Russian], Nizhegorodskiĭ Universitet im. N. I. Lobachevskogo (1997), Vol. 56, pp. 43–49.

Translated by P. Shelnitz